OFF-TRACK VIBRATIONS OF THE READ-WRITE HEADS IN HARD DISK DRIVES

BY

HANY MICHAEL GROSS

B. S. (THE AMERICAN UNIVERSITY IN CAIRO) 1995

M. S. (THE AMERICAN UNIVERSITY IN CAIRO) 1997

A DISSERTATION SUBMITTED IN PARTIAL SATISFACTION OF THE

REQUIREMENTS FOR THE DEGREE OF

DOCTOR OF PHILOSOPHY

IN

ENGINEERING – MECHANICAL ENGINEERING

IN THE

GRADUATE DIVISION

OF THE

UNIVERSITY OF CALIFORNIA, BERKELEY

COMMITTEE IN CHARGE:

PROFESSOR DAVID B. BOGY, CHAIR

PROFESSOR ROBERTO HOROWITZ

PROFESSOR ÕMER SAVA[a]

PROFESSOR GREGORY L. FENVES

SPRING 2003

The dissertation of Hany Michael Gross is approved:

Chair	Date
	Date
	Date
	Date

University of California, Berkeley

Spring 2003

OFF-TRACK VIBRATIONS OF THE READ-WRITE HEADS IN HARD DISK DRIVES

BY

HANY MICHAEL GROSS

ABSTRACT

OFF-TRACK VIBRATIONS OF THE READ-WRITE HEADS IN HARD DISK DRIVES

By

Hany Michael Gross

Doctor of Philosophy in Engineering – Mechanical Engineering

University of California, Berkeley

Professor David B. Bogy, Chair

The demand for higher magnetic recording densities translates directly into demands for higher track densities and higher linear bit densities. This, in turn, requires squeezing the track misregistration and flying height modulation into tighter budgets. On the other hand, the demand for higher data access rates and reduced latency dictates using higher disk rotation speeds. Such high disk speeds lead to higher flow velocities, and consequently to higher levels of aerodynamic forces in the drive. With this decrease in the allowable vibration budgets and increase in excitation levels, effects that were formerly considered negligible in hard disk drives are becoming quite significant. This motivates studying the dynamics of the disk drive at a higher level of complexity, employing advanced algorithms for servo control, and understanding the airflow in the drive and its effects on structural vibrations.

Increasing the track density can be achieved by reducing component disturbances that move the read-write heads off-track, improving the structural characteristics of drive components so that their response to disturbances is attenuated, and enhancing the ability

of the servo controller to keep the heads on narrower tracks. The research presented in this dissertation was aimed at investigating and mitigating off-track vibrations of read-write heads in hard disk drives. It addressed three objectives. The first objective was to study and understand drive dynamics at the system level. The second objective was to determine the optimal orientation of strain sensors on an instrumented suspension to detect suspension vibrations that may contribute significantly to the off-track motion of the read-write head. These strain measurements would provide real-time suspension vibration information that can be employed in control schemes to suppress off-track vibrations. The third objective was to experimentally study and characterize airflow effects in hard drives, and to reach a better understanding of the relationship between airflow and head vibration.

The dynamics of the head stack assembly were studied using finite element modeling and analysis. The approach adopted was to examine the dynamic characteristics of the individual components of the head stack assembly, namely the head gimbal assemblies and the actuator block, and then investigate and understand the dynamic characteristics of the system as a whole in terms of the component dynamics and their coupling. The head stack assembly modes were categorized into two groups: modes that can potentially contribute significantly to off-track vibrations of the read-write heads, and modes that can contribute significantly to flying height-modulation.

Several researchers proposed the use of strain sensors for active vibration control in disk drives. The main idea was to strategically attach strain sensors to measure localized

strains at key locations on drive structures, so that the sensors will effectively detect structural vibrations that may result in off-track motion of the heads. The measured strain information can then be used by the servo controller to suppress off-track motion of the heads by using active feedback damping or active feedforward compensation. A prerequisite to implementing such an approach was determining the optimal placement of the strain sensors. In this study, the optimal location and orientation of strain sensors on an instrumented suspension were determined based on the degree of observability of suspension modes that contribute to off-track vibration of the heads.

The final part of this work addressed the characterization of airflow effects in hard disk drives through experimental research of the effects of the actuator arm geometry on the off-track vibrations of the heads and airflow in a modeled drive. The effects of the actuator arm thickness on the off-track vibrations of the read-write heads and the airflow in the modeled drive were investigated. Power spectra of the off-track vibrations of the heads were measured using laser Doppler vibrometry at the inner diameter, the middle diameter, and the outer diameter radial positions, for four arms with different thicknesses. These power spectra were used to compute the root mean square (rms) off-track vibrations and their components over several frequency bands. Airflow speed was measured in the region downstream of the arm tip using constant-temperature hot-wire anemometry at the inner diameter radial position. The flow measurements were used to compute the mean and rms flow speed, the turbulence intensity, and the mean and rms dynamic head distributions in the measurement region. The rms flow and dynamic head fluctuations were decomposed into components over the same frequency bands selected

for the decomposition of the rms vibrations. A positive correlation was observed between the rms components of the dynamic head fluctuations and the corresponding rms components of the off-track vibrations of the heads.

The effects of the actuator arm leading edge profile on the airflow downstream of the arm tip were also investigated. Five edge profiles were tested: rectangular, chamfered, U-cut, rounded, and stepped profiles. Airflow speed was measured in the region downstream of the arm tip using hot-wire anemometry at the inner diameter radial position. The flow measurements were used to compute the mean and rms flow speed, the turbulence intensity, and the mean and rms dynamic head distributions in the measurement region. The rms flow and dynamic head fluctuations were decomposed into components over several frequency bands. Modifying the arm profile from rectangular to any of the other shapes resulted in a reduction in the levels of flow fluctuations in the high-fluctuation region observed, and the dispersion of these regions over a larger area. The stepped arm generated the lowest levels of fluctuation, and therefore it is expected to be the most promising geometry of those studied for reducing read-write head vibration.

_____

Professor David B. Bogy
Dissertation Chair

DEDICATION

To my parents, wife, sister and brother.

TABLE OF CONTENTS

LIST OF FIGURES

Chapter 1

Chapter 2

LIST OF TABLES

SYMBOLS

a	scale factor for windowing function in spectrum analyzer
A	projection of the area of the body onto the flow direction
$\boldsymbol{A}$	system matrix
$\boldsymbol{B}$	input matrix
c_t	torsional damping coefficient
C_D	sectional drag coefficient
$\boldsymbol{C_q}$	strain projection matrix
d	effective magnetic spacing between head and surface of the medium
D	drag force
$\overline{D}$	mean drag force
D_{rms}	rms drag force fluctuation
E	Young's modulus
$f_{cyl,\mathrm{t}}$	vortex shedding frequency; free flow over circular cylinder with diameter t
f_v	vortex shedding frequency
g	gravitational constant
G	shear modulus
$\overline{G_{u'}(f)}$	averaged flow fluctuation power spectrum
$\overline{G_Y(f)}$	averaged vibration power spectrum
$\overline{h}$	mean dynamic head
h_{rms}	rms dynamic head fluctuations
H	slider height
I_{xx}	slider roll mass moment of inertia (I_{roll})
I_{yy}	slider pitch mass moment of inertia (I_{pitch})
I_{zz}	slider yaw mass moment of inertia (I_{yaw})
K_t	torsional stiffness coefficient
l	characteristic length of the body
L	slider length
m	slider mass
p_k, q_k	coefficients of residue of k^{th} mode
q	dynamic pressure
$\overline{q}$	mean dynamic pressure
q'	dynamic pressure fluctuation

q_{rms}	rms dynamic pressure fluctuation
R	disk radius
Re	the Reynolds Number
s	complex variable
S	disk-to-disk spacing
$SL(l)$	separation loss
St	the Strouhal number
t	obstruction/arm thickness
TI	turbulence intensity
u	flow speed
$\boldsymbol{u}$	input vector
$\bar{u}$	mean flow speed
u'	flow speed fluctuation
u_{rms}	rms flow fluctuation
U	characteristic speed of the flow
V_d	disk surface speed
W	slider width
$\boldsymbol{x}$	state vector
$\dot{\boldsymbol{x}}$	derivative of $\boldsymbol{x}$
Y_{rms}	rms off-track vibration of the read-write head
$a(s)$	frequency response function
$\boldsymbol{e}$	plane strain component vector
e_q	projected strain along angle q
e_x	x-direction strain component
e_y	y-direction strain component
g_{xy}	xy shear strain component
l	recorded wavelength
n	Poisson's ratio
n_k	kinematic viscosity of the fluid
q	strain projection angle
r	density
w	frequency of excitation
$\bar{w}_k$	natural frequency of k^{th} mode
z_k	modal damping factor of k^{th} mode

ABBREVIATIONS

ABS	Air Bearing Surface
BPI	Bits Per Inch
CD	Compact Disk
CTA	Constant-Temperature hot-wire Anemometry
DVD	Digital Versatile Disk (formerly Digital Video Disk)
FEA	Finite Element Analysis
FHM	Flying Height Modulation
FRF	Frequency Response Function
GMR	Giant Magneto-Resistive
HDD	Hard Disk Drive
HDI	Head-Disk Interface
HGA	Head Gimbal Assembly
HMS	Head Media Separation
HSA	Head Stack Assembly
ID	Inner Diameter
INSIC	INformation Storage Industry Consortium (formerly NSIC, National Storage Industry Consortium)
LDA	Laser Doppler Anemometry
LDV	Laser Doppler Vibrometry
MD	Middle Diameter
MEMS	Micro-Electro-Mechanical System
MOSFET	Metal-Oxide-Semiconductor Field Effect Transistor
MR	Magneto-Resistive
OD	Outer Diameter
PDA	Personal Digital Assistant
PES	Position Error Signal
RAID	Redundant Array of Independent Disks
RFP	Rational Fraction Polynomials
RMS	Root Mean Square
RPM	Revolutions Per Minute
TMR	Track MisRegistration
TPI	Tracks Per Inch
VCM	Voice-Coil Motor

ACKNOWLEDGEMENTS

I am honored to have had the privilege of working under the supervision of Professor David B. Bogy during my career at Berkeley. As a mentor, his incessant guidance and encouragement, his untiring support, and his remarkable thoroughness have been deeply enlightening over the course of my research at the Computer Mechanics Laboratory. As a friend, his sincere care, abundant thoughtfulness, and priceless advice have been a source of comfort and inspiration. I am very fortunate to have him as both a mentor and a friend.

I wish to express my utmost gratitude to Professor Ömer Savaº for the guidance that he gave me in my research over the past two years, and for the many illuminating discussions that we had. His patience and commitment to this work have played a pivotal role in its progress.

I must thank Toru Watanabe, of the Hard Disk Division at Fujitsu, for his contributions to this work during his stay as a visiting industrial fellow at the Computer Mechanics Laboratory. Our collaboration to address a multitude of research issues was synergetic and most fruitful.

I owe a great deal to Professor Oliver O'Reilly for his invaluable advice on both the academic and non-academic fronts. His genuine support and encouragement stemmed from truly believing in me. It is a pleasure and an honor to have had him as a friend and teacher at Berkeley. I would also like to thank Professor Andrew Szeri for his friendship, his help, and his interest in my work. My sincere appreciation goes to Professor Roberto

Horowitz and Professor Gregory Fenves for the helpful feedback and suggestions they provided to make this dissertation a better piece of work.

Finally, I cannot express enough gratitude to my parents, Jim and Josephine; my wife, Joanna; my sister, Suzanne; and my brother, Shady. Their constant love, devotion, sacrifices, understanding, support, and encouragement are a solid foundation for my well-being and achievement.

This research was supported by the Computer Mechanics Laboratory and the University of California, Berkeley. It was also supported in part by the Information Storage Industry Consortium and the Hard Disk Drive Division at Fujitsu Ltd.

Hany Michael Gross

Berkeley, May 2003

CHAPTER 1

INTRODUCTION

1.1. The History of Magnetic Recording

Since its inception towards the end of the nineteenth century, the use of magnetic recording expanded to the point where it has become an essential ingredient of our everyday life. The versatility of magnetic recording and its implementation in different storage media formats (such as hard disks, tapes, flexible disks, stripes, and cards) make it adaptable to a wide range of data, audio, and video applications, both at the business and consumer levels. Applications of magnetic recording include audio magnetic tapes, video magnetic tapes, computer hard disk drives, computer tape cartridges, floppy disks, and magnetic stripes on credit cards, to list a few.

The principles of magnetic recording were first conceived by *Oberlin Smith*. He described these principles in 1878, and published them in *Electrical World* in September of 1888, but he never demonstrated a device that utilized magnetic recording [1]. The Danish inventor *Valdemar Poulsen* rediscovered the magnetic recording principle in 1894 while working as a mechanic in the *Copenhagen Telegraph Company*. He demonstrated and patented the first successful magnetic recording device, the *telegraphone*, in 1898 [1]. It consisted of a steel wire wrapped around a drum and a recording/playback electromagnetic head that moved over the wire (around the cylinder) using a screw thread. An electrical current generated using a telephone microphone was passed through the electromagnetic head, which *magnetized* the steel wire as it moved along. *Poulsen's*

telegraphone illustrates the basic components of any magnetic recording device: a *recording medium*, which can be magnetized using a magnetic field, and can retain its magnetization after the field is removed; a *read-write head* that can be used to generate the magnetic field to '*write'* to the recording medium, and that can '*read'* the magnetic pattern from the magnetized medium and generate an output that is representative of the stored information; and a *transport mechanism* to move the read-write head over the recording medium.

After *Poulsen's telegraphone* failed commercially and his patent expired in 1918, Germany led efforts to research and improve magnetic recording. *Kurt Stille* developed the *Dailygraph* magnetic wire recorder as a dictating machine in 1925, which was later developed further into the *Textophone* by *Semi Joseph Begun*. *Begun* then developed a steel tape recorder for radio broadcast use, called the *Stahltone-Bandmaschine*. In 1928, *Fritz Pfleumer* was granted a German patent for the application of magnetic powders to strips of paper or film, which he called '*sounding paper'*. *Pfleumer's* work paved the way for thin plastic tape to replace wire and steel tape in the 1930s [1]. In 1930 the *Allgemeine ElektrizitatsGesellschaft* (*AEG, German General Electric*) in Berlin adopted the *Pfleumer* principle and proceeded to develop a *magnetophon* machine. Five years later, in collaboration with *BASF*, they produced the *magnetophon K1*: the world's first production tape recorder. They presented the *magnetophon* and the magnetic tape to the public during the 1935 Radio Fair in Berlin [1].

In the 1946-1947 period, the need for rapid data access and high-speed operation motivated the development of large-capacity random-access storage systems of digital information. These systems were to be used for storing alphabetical and numerical data, augmenting, and possibly replacing, the punched tape or photographic film, which were too slow because they stored data sequentially. The use of a revolving surface such as a disk or a drum was suggested, and the first implementation came in the form of a small drum with strips of magnetic tape cemented to its surface. Many read-write heads (with one head dedicated to each track) were held in a non-contact mode at a fixed distance from the drum to prevent wear of the tape or head. Later the number of heads in recording drums was significantly reduced through the use of mechanisms that moved the heads from one track to another as they flew over the boundary layer of air attached to the rotating drums [1].

During the early stages of their development, recording drums presented an attractive storage solution because they provided rapid access to the large amount of information required for scientific computation at a time where no other means for doing that were available. At a later stage, newer disk memories with much higher bit densities offered a more compact and more economic means of random-access large-capacity external storage. Data storage on hard magnetic disks was introduced, and it flourished to dominate the market of random-access mass-storage.

1.2. Data Storage on Hard Magnetic Disks

1.2.1. The Evolution of Hard Disk Drives

IBM (*International Business Machine*) introduced the first commercial hard disk drive, the *IBM 350* disk file, in 1956. It was a fast-access data recorder using coated rigid disks and heads with random access to any data track. The *IBM 350* was incorporated into *IBM's RAMAC* (*Random Access Method of Accounting and Control*) system. It contained a stack of fifty 24-inch diameter aluminum disks coated on both sides with a magnetic iron oxide, with an *areal storage density*[1] of 2000 bits/in^2 (100 *BPI* and 20 *TPI*). The read-write head was supported over the disk surface by a hydrostatic pressurized air bearing. The capacity of the entire disk file was 5 million 7-bit characters, which is equivalent to around 4.4 megabytes, and a data rate of 70 kbits/s [1]. The *RAMAC* established the generic structure for all '*hard'* disk drives: read-write heads flying in proximity over the surface of a rotating disk that can also be moved randomly to any radial position to access different data tracks.

The *IBM 350* disk drive was a revolutionary product because it allowed more storage in less space compared with magnetic storage drums. However, the drive was *big*, not quite ready for today's laptops: it occupied the space of two refrigerators and weighed a ton. By comparison, one of the disk drives demonstrated by *IBM* in 1999 had an areal density of 5.7 Gbits/in^2, a data rate of 118 Mbits/s and stored 6.5 gigabytes of information on two

[1] The *areal recording density* (usually expressed in bits per square inch, bits/in^2) is defined as the amount of data that can be stored on a unit area of the recording medium. In hard disk drives, areal density is equal to the product of the *linear bit density* (the number of bits per inch, BPI, along a circumferential track) and the *track density* (the number of tracks per inch, TPI). This is demonstrated in Figure 1.1.

2.5-inch diameter disks. That is a three-million-fold increase in storage density in 42 years, with quite a reduction in size.

At the turn of the century *IBM* achieved a milestone in data storage technology that demonstrates the extent to which drive dimensions can be reduced by making the 1-inch, 1 gigabyte *IBM microdrive* [2]: the world's smallest, lightest drive (Figure 1.2). The areal storage density had been increasing at an average rate of 23% per year (10-fold in 10 years), from 1956 to 1991. In 1991, the rate of growth jumped to around 60% per year (10-fold in 5 years), and it continued at that level to the end of the millennium. Since then, the areal density has been growing at the rate of over 100% per year. *Seagate Technology* recently demonstrated an areal density of 101 Gbit/in^2, with a track density of 149 kTPI, a linear bit density of 680 kBPI, and a data rate of 256 Mbit/s [3]. These astounding advances were driven by the same considerations that caused disk drives to replace recording drums: more storage in less space. The repercussions of these advances extend far beyond the convenience of compact storage devices. Their economic implications manifest in the reduction of the number of components (disks and heads) in the drive, and the associated savings in production costs: a substantial sum on the scales of mass production.

1.2.2. Basics of Hard Disk Drive Design and Storage

Figure 1.3 illustrates a typical hard disk drive with the top cover removed [4]. Every hard disk drive (HDD) contains one disk, or a stack of disks, mounted on a spindle rotating inside an enclosure, and usually twice as many magnetic read-write heads as disks

mounted on sliders. These sliders fly over the disks as a result of the hydrodynamic air bearing that is generated at the head-disk interface (HDI) by the air-bearing surface (ABS) of the slider. The spacing between the read-write head on the slider ABS and the disk surface is known as the *flying height*. The sliders are loaded against the disks by means of spring suspensions, which are compliant in the direction perpendicular to the disk surface. The head/slider/suspension assembly is usually referred to as the *head gimbal assembly* (*HGA*). The HGAs are attached to arms mounted on an actuator block, called the *E-block*, which also holds the actuator voice-coil. The actuator is a linear or rotary, electromagnetic actuator driven by a *voice-coil motor* (*VCM*), providing random access by moving the heads to any desired track on the disk. The HGA/E-block/voice-coil assembly is usually referred to as the *head stack assembly* (*HSA*) [5].

Data is written to and read from the magnetic media on the disks through two different elements: the write head, and the read head. These two heads are integrated into a single read-write head as shown in Figure 1.4 [6]. The write head consists of a coil wrapped around a yoke with a writing gap. When a current is passed through the coil, it generates a magnetic field that magnetizes the yoke producing North and South poles at the writing gap. The magnetic field at the gap establishes the polarity of the media passing under the write gap. The smaller the gap length and the closer the head is to the disk, the higher the possible bit density. The narrower the gap width, the higher the possible track density. Reversals of the electric current result in magnetic field reversals at the gap, which in turn result in reversals of the polarity on the magnetized media on the disk. These reversals are used to define bits. Since the disk is spinning, magnetic flux reversals (and

consequently bits) are arranged along concentric circles on the disk, called *tracks*. The read head uses magnetically sensitive resistors utilizing the *magneto-resistive* (*MR*) effect. Most modern drives use *giant magneto-resistive* (*GMR*) heads, which are much more sensitive than standard magneto-resistive heads.

The distance between the read-write head and the media is commonly referred to as the *magnetic spacing*, or the *head-media separation* (*HMS*). The magnetic spacing contains the disk and slider carbon overcoats, the disk lubricant, the flying height, and the *pole-tip recession*[2]. The linear bit density can be increased by reducing the HMS in order to reduce the bit spot size during writing, and improve the strength of the read-back signal during reading. The strength of the read-back signal is governed by the *Wallace spacing loss equation* [7]

$$\begin{aligned} \mathrm{SL}(\lambda) &= \exp\left(\frac{-2\pi d}{\lambda}\right) \\ &= -54.6\frac{d}{\lambda}\ [\mathrm{dB}], \end{aligned} \tag{1.1}$$

where *SL(l)* is the separation loss, λ is the recorded wavelength [μm], and d is the effective magnetic spacing between the head and the surface of the medium [μm].

The physical location of a unit of data on the disk is identified by a unique address consisting of three components: *head*, *cylinder*, and *sector*. This addressing system is quite similar to the cylindrical coordinate system. The head component of the address identifies the disk surface on which the data unit in question is located, and it is defined

[2] The *pole-tip recession* refers to the height difference between the pole tips of the read-write head and the ABS of the slider. The pole-tip recession is zero only if the pole tips are flush with the slider surface.

by vertically numbering the disk surfaces, usually starting with the bottom-most surface. The cylinder component of the address identifies the radial position of the data unit, and it is defined by numbering the tracks (or the concentric cylinders passing through the tracks on a disk stack) starting with 0 at the outermost track. Tracks are divided into segments called *sectors*. The sector component of the address identifies the angular position of the data unit, and it is defined with respect to a reference angular position of the disks.

In modern disk drives, position information (called *servo bursts*) is encoded at regular intervals between data sectors on the disk surfaces during manufacturing. This is known as an *embedded servo* system. Servo bursts provide the servo controller with a reference for position feedback control information. The controller compares this position with the storage location of the target bit, as specified by its address. The difference between the actual and desired locations is called the *position error signal* (*PES*), and it is used to produce a correction signal to the actuator through feedback control. When moving from one track to another, the servo controller operates in *track seek* mode. It then *settles* on the target track, and operates in *track following* mode. The *seek time*, the *settling time*, and the *latency* (the time for the disk to rotate the target sector under the head) comprise the *access time*, which is the time required to move the head to the desired track and have it ready to read or write data. It is highly desirable to reduce access times as low as possible in order to prevent overall delays in storing, retrieving, or processing data.

1.2.3. The Future of Hard Disk Drives

Higher storage densities, faster data access speeds, and lower costs form a triad of conflicting requirements in data storage. Technologies other than hard magnetic storage disks are available for online data storage. Non-volatile semiconductor memory devices store data based on the principle of storing electric charges in the gate insulator of a MOSFET (Metal-Oxide-Semiconductor Field Effect Transistor). Semiconductor memory has the advantage of fast data access, but its relatively high cost-per-stored-bit regulates its use and limits it to low capacity applications such as flash memory for portable devices like digital cameras and camcorders, digital cellular phones, flash cards for laptop computers, personal digital assistants (PDAs), and MP3 players. Optical storage devices, such as CD (Compact Disk) and DVD (Digital Versatile Disk) devices, do not compete with HDDs in neither storage capacity nor data access speed. Consequently, their application lies mainly in areas requiring high-capacity data portability and data distribution.

HDDs offer the attractive combination of large storage capacity and high data access speed, all at low cost, which will allow them to maintain their position as the primary online data storage device for computers in the foreseeable future. In addition, the expanding market segment of offline storage presents an opportunity for increased application of high-performance HDDs in RAIDs (Redundant Arrays of Independent Disks). Finally, the outlook for the use of HDDs in new applications – such as in digital cameras, PDAs, and digital video recording (DVR) devices – is promising.

1.3. Motivation

The disk drive industry is continually faced with demands for higher areal recording densities, faster data access speeds, higher reliability, and lower cost. The *Information Storage Industry Consortium* (*INSIC*) areal density goal of 100 Gbit/in^2, with a corresponding track density of 175 kTPI, is no longer a pre-competitive research objective. It was recently relabeled by the *INSIC* as '*competitive'* research, and it is currently making its way into industry roadmaps. The new *INSIC* goal is *1 Tbit/in^2*. The demand for a higher areal density translates directly into demands for increasing the track density and the linear bit density, which, in turn, require squeezing the *track misregistration*[3] (*TMR*) and *flying height modulation*[4] (*FHM*) into tighter budgets. It is estimated that a track density of 540 kTPI will be necessary to achieve the new *INSIC* goal [8]. This corresponds to a track pitch of 47 nm, and consequently a reduced allowable TMR budget[5] of less than 5 nm. The projected flying height for the 1 Tbit/in^2 areal density is 3.5 nm [8]. Reliable reading and writing of data require that the HMS fluctuate by no more than ±10% [9]. Taking the head and disk overcoats into account, the limit on the FHM would be 0.5 nm at a 3.5 nm flying height.

On the other hand, the demand for higher data access speeds dictates using faster positioning speeds to reduce seek time, and faster disk rotation speeds to reduce latency. High positioning speeds result in higher residual vibrations of the HSA and the read-write

[3] The *track misregistration* is a statistical distribution that relates to the off-track vibrations of the read/write heads.
[4] The *flying height modulation* is the fluctuation in the flying height, which is the spacing between the read/write head and the disk.
[5] As a rule of thumb, the allowable TMR is limited to 12% of the track pitch. The *track pitch* is the reciprocal of the track density.

heads as the VCM swings back and forth quickly during seeking and tracking. The increased disk speeds lead to greater flow velocities, and consequently to higher levels of aerodynamic forces in the drive. The result is an increase in windage disturbances that excites the structural modes of the HSA and the disks, inducing greater TMR and FHM.

With the meager allowable TMR and FHM limits decreed by higher areal densities, and the elevated windage excitation ensuing faster disk rotation speeds, smaller variations in slider positioning pose a potential threat of read errors, write errors, and head-disk slaps. Consequently, effects that were formerly considered negligible are now becoming quite significant. This motivates studying the dynamics of the disk drive at a higher level of complexity, employing advanced algorithms for servo control, and understanding the airflow in the drive and its effects on structural vibrations.

1.4. Research Objectives

Increasing the track density can be achieved by reducing component disturbances that move the read-write heads off-track, improving the structural characteristics of drive components so that their response to disturbances is attenuated, and enhancing the ability of the servo controller to keep the heads on narrower tracks. The research presented in this dissertation was aimed at investigating and mitigating off-track vibrations of read-write heads in HDDs. It addressed three objectives. The first objective was to study and understand HDD dynamics at the HSA level. The approach adopted was to examine the dynamic characteristics of the individual components of the HSA, namely the HGAs and the actuator block, and then investigate and understand the dynamic behavior of the HSA

as an integrated system in terms of the component dynamics and their coupling. The second objective was to determine the optimal orientation of strain sensors on an instrumented suspension to detect suspension vibrations that may contribute significantly to off-track motions of the read-write head. These strain measurements would provide real-time suspension vibration information that could be employed in control schemes, such as active feedback damping or active feedforward compensation, to suppress off-track vibrations. The procedure was based on the degree of observability of the modes that contribute to the off-track motions of the heads. The third objective was to experimentally study and characterize airflow effects in HDDs, and to reach a better understanding of the relationship between airflow and head vibrations. This objective was tackled by investigating the effects of the actuator arm geometry on the airflow and the off-track vibrations of the heads in a modeled HDD.

1.5. Dissertation Outline

This dissertation is divided into six chapters. Chapter 1 is an introduction that covers the history of magnetic recording and HDDs, the basics of HDD design and storage, the motivation for this work, and the objectives of the research presented. Chapter 2 is a study of HDD dynamics at the HSA level using finite element modeling and analysis. Chapter 3 is a study of the optimal strain sensor placement on an instrumented suspension for suppression of off-track vibrations of read-write heads in HDDs. Chapter 4 is an experimental investigation of the effects of E-block arm thickness on the off-track vibrations and the airflow in a modeled HDD. Chapter 5 is an experimental investigation

of the effects of E-block arm leading edge profile on the airflow in a modeled HDD. Chapter 6 presents the summary and conclusions of the dissertation.

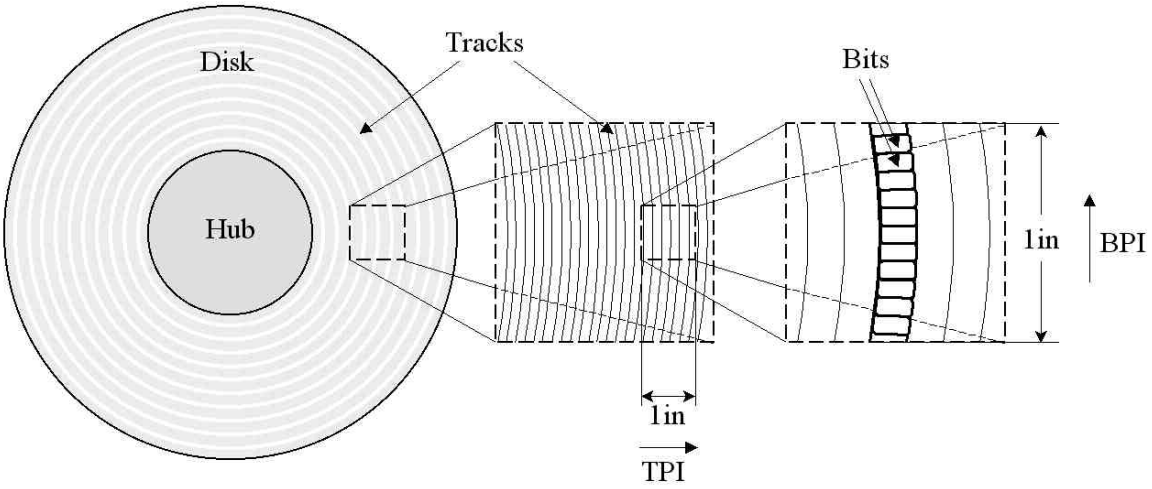

Figure 1.1: Areal storage density.

Figure 1.2: The *IBM microdrive* [2].

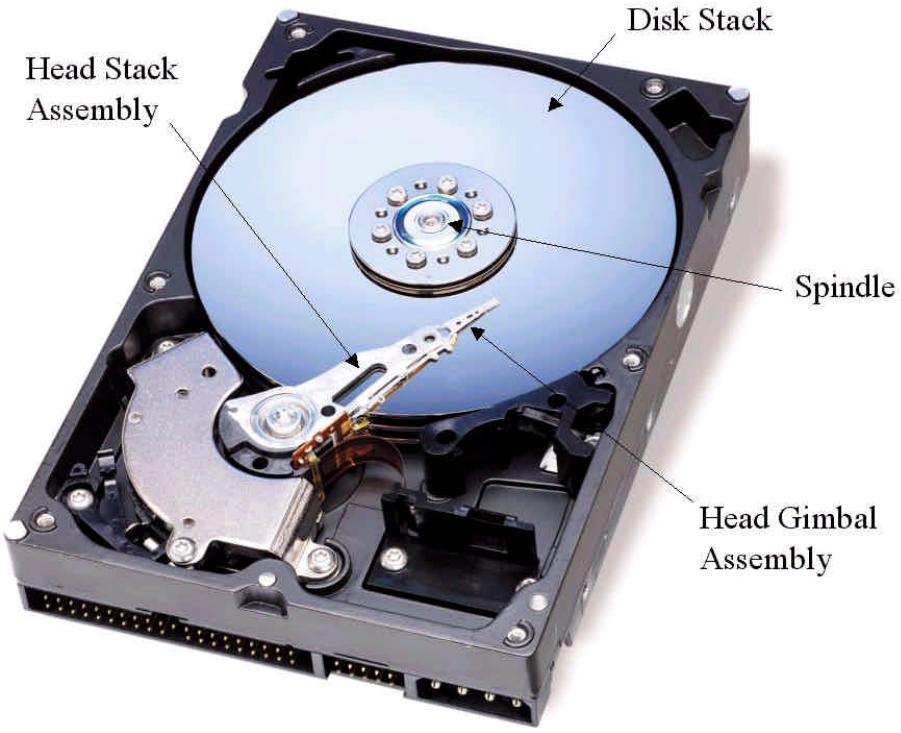

Figure 1.3: Components of a typical hard disk drive [4].

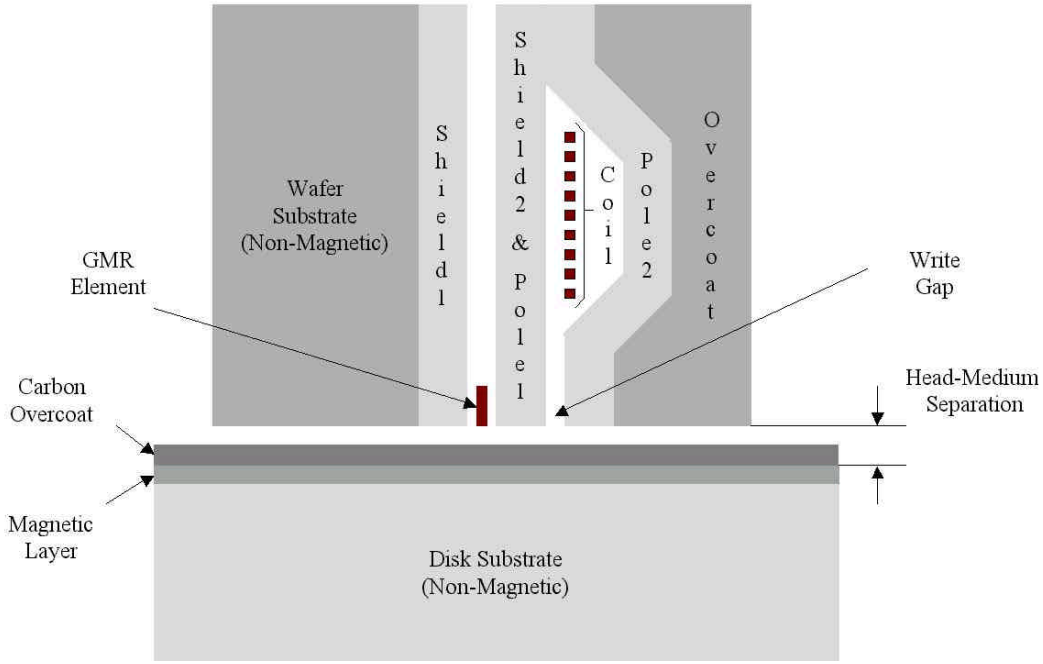

Figure 1.4: Integrated read-write head [6].

CHAPTER 2

A STUDY OF DISK DRIVE DYNAMICS AT THE HEAD STACK ASSEMBLY LEVEL

2.1. Introduction

Many studies have been dedicated to investigating the dynamics of individual drive components, but very few have investigated 'drive-level' dynamics. Studies that focused on individual components include the work of *Okawa et al.* [10], which presented modal analysis results for HDD E-blocks; the work of *Yoshida et al.* [11], which presented a new actuator design to reduce residual vibrations; the study by *Ku* [12], which investigated the dynamic characteristics of spindle motors and compared ball bearings with hydrodynamic bearings; the study by *McAllister* [13], which investigated the effect of platter resonances on TMR, and found that axial disk vibrations produced a significant portion of the TMR at 7200 rpm; and the work of *Zeng and Bogy* [14], which investigated the dynamic properties of an HGA using modal testing and finite element analysis (FEA).

Some of the studies carried out at the drive system level include [15], in which *Radwan and Whaley* studied servo-structure interaction using FEA, and examined the effect of structural resonances on the open loop servo response of the drive; [16], in which *Wilson and Bogy* carried out modal tests on suspensions loaded on spinning disks, and investigated the dynamic coupling of the suspension and disk modes; [17] and [18], where *Zeng and Bogy* investigated the dynamic characteristics of HDDs using modal testing and FEA.

In this study, FEA was used to investigate and understand the dynamics of the hard disk drive at the HSA level. The approach adopted was to examine the dynamic characteristics of the individual components of the HSA, namely the HGA and the actuator E-block/voice-coil unit, and then investigate the dynamic behavior of the HSA as an integrated system in terms of the component dynamics and their coupling. The objective of the study was not to accurately identify the modal parameters of the modeled HSA, but rather to examine the dynamic behavior of the system and reach a better understanding and appreciation of the nature and complexity of its response. This is an essential prerequisite to accurate structural identification, modification, analysis, and design in the drive. Research plunging into such tasks without a keen understanding of the system response would likely be overwhelmed by the abundance of modes associated with such a complex structure.

2.2. Finite Element Modeling and Analysis

The main components of the HSA are the HGAs and the actuator E-block/voice-coil unit (which will henceforth be referred to as the E-block unit for short). The HGA consists of the base-plate, the suspension load-beam, the flexure, and the slider. It was considered as a subsystem of the HSA without further division. The E-block unit consists of the E-block with the actuator arms and the voice-coil, integrated together through an over-mold encapsulation. All finite element modeling and analyses were carried out using *ANSYS* FE software. The modeled HSA was a two-platter HSA using *Western Digital's*[6] '*Rebel'*

[6] Western Digital Corporation

E-block unit, and four *Hutchinson*[7] '*Conventional HTI2030*' suspensions. The details of the modeling and boundary conditions applied to each subsystem are described below.

A modal analysis[8] was carried out to obtain the modal parameters of each subsystem, and the associated mode shapes were examined. A harmonic analysis[9] was also performed to obtain frequency response functions (FRFs) of each subsystem to a given excitation. The harmonic analysis focused mainly on FRFs associated with off-track vibrations. Descriptions of the excitations and parameters used in the modal and harmonic analyses are included below. The models of the E-block unit and the HGAs were then integrated to obtain a model of the HSA. Modal and harmonic analyses of this model were carried out and the results were compared with those of the individual components.

2.2.1. The Head Gimbal Assembly

The HGA consisted of the base-plate, the suspension load-beam, the flexure, and the slider. The load-beam was modeled using 714 *SHELL43* 4-node structural shell elements with 872 nodes. The flexure was modeled using 130 *SHELL43* elements with 190 nodes, and it was attached to the load-beam at the laser spot weld locations using *BEAM4* 3-D elastic beam elements. The material properties used for both the load-beam and the flexure were those of stainless steel and are listed in Table 2.1. The material used for all beam elements was assigned high stiffness and zero density so as to provide the desired

[7] Hutchinson Technology Incorporated
[8] A modal analysis in *ANSYS* identifies the natural frequencies and associated mode shapes of the modeled structure.
[9] A harmonic analysis in *ANSYS* determines the response of the structure to sinusoidally varying loads (in the form of displacements or forces) applied at selected nodes.

attachment without dynamically loading the system. The material property values used are listed in Table 2.1. The flexure dimple[10] was also modeled using *BEAM4* elements. In order to model the point of contact between the dimple and the flexure, a node on the flexure coincident with the apex node of the dimple was created, and the two nodes were constrained to have the same translational coordinates, but they were allowed to rotate relative to one another. The slider, which is basically a parallelepiped block as depicted in Figure 4.2(b), was modeled using a *MASS21* structural mass element, which is a single-node element that can be assigned a mass and rotational mass moments of inertia. It was given the following inertial properties, which are typical of a pico-slider[11]:

Mass, $m = 1.71\times10^{-6}$ kg

Roll mass moment of inertia (I_{roll}), $I_{xx} = 0.141\times10^{-6}$ kg· mm^2

Pitch mass moment of inertia (I_{pitch}), $I_{yy} = 0.221\times10^{-6}$ kg· mm^2

Yaw mass moment of inertia (I_{yaw}), $I_{zz} = 0.343\times10^{-6}$ kg· mm^2

The slider mass element was positioned at the location of the center of gravity of the slider, and was attached to the flexure using BEAM4 elements.

The base-plate was modeled using 1072 *SOLID72* 3-D 4-node tetrahedral structural solid elements with 406 nodes, and it was attached to the load-beam at the laser spot weld locations using *BEAM4* 3-D elements. The HGA was initially modeled as a flat structure

[10] The *flexure dimple* is a dimple-shaped impression on the flexure that allows the slider to rotate with very little resistance in the pitch and roll directions, so that it can maintain its flying attitude relative to the disk in spite of the undulations and asperities of the disk.

[11] The '*pico'* prescript denotes the *form factor*, or size, of the slider. The custom in the HDD industry is to take the '*mini'* slider (with a length *L* of 4.06 mm, a width *W* of 3.20 mm, and a height *H* of 0.86 mm) as a reference for slider dimensions. With the gradual reduction in drive size, the dimensions of the '*micro'*, '*nano'*, '*pico'*, and '*femto'* sliders were taken as around 70%, 50%, 30%, and 20% of the mini-slider dimensions. Most current drives use pico-sliders, with efforts being made to switch to femto-sliders in the future. The dimensions of a pico-slider are *L* = 1.25mm, *W* = 1.00 mm, and *H* = 0.30 mm.

(with a formed load-beam and a formed flexure). It was then bent into its *free state*[12] using a coordinate transformation of the appropriate nodes. Finally, to obtain the model for the HGA in the *loaded state*[13] a nonlinear static analysis[14] was performed in which the slider was loaded to the desired offset, and the coordinates of the nodes were updated to the deformed configuration. Figure 2.1 shows the solid and FE models of the HGA. Figure 2.2(a) shows a close up of the slider and the dimple and Figure 2.2(b) shows the free and loaded states of the suspension.

In the analyses of the HGA, the base-plate area of the load-beam was completely constrained to have no degrees of freedom, so that its nodes could neither translate nor rotate in any direction. Since the base-plate would also have been fully constrained in these analyses, it was removed from the HGA model. This reduced the model size without affecting the results. Each HGA model contained a total of 1089 nodes. Air bearing dynamics were not considered in the modal and harmonic analyses. The slider node was constrained to give the slider a fixed *flying attitude*: fixed flying height (z translation), fixed pitch (y rotation), and fixed roll (x rotation). This is justified by the fact that the air bearing resonant frequencies (typically over 100 kHz) are much higher than the frequency range considered, and that changes in the flying attitude of the slider are negligible for the purpose of our analyses: changes in the flying height are on the order of nanometers, and changes in the pitch and roll are on the order of micro-radians.

---

[12] The *free state* describes the suspension with the pre-bend, before it is loaded onto the disk.
[13] The *loaded state* describes the suspension while the slider is loaded on the disk. The loaded state is characterized by a 'hump' at the bend region, and a 'sag' between the bend region and the slider.
[14] A static analysis in *ANSYS* calculates the nodal displacements and element stresses due to applied loads (in the form of applied displacements of forces) at selected nodes.

Figure 2.3 shows a FRF of the HGA that was obtained using harmonic analysis: the off-track response of the slider node to a unit sinusoidal lateral excitation at the base-plate area over the frequency range 0-45 kHz. This FRF exhibited several resonant peaks, marking the frequencies of the modes that contribute significantly to off-track vibration. It should be noted that a damping ratio of 0.0013 was imposed during the harmonic analysis in *ANSYS*. This value was an estimate of the average modal damping ratio based on unpublished experimental results. The natural frequencies and mode shapes of the HGA over the range 0-14 kHz were computed using modal analysis, with the base-plate area completely fixed. The natural frequencies are listed in Table 2.2, and some of the modes are shown in Figures 2.4 through 2.10. The modes associated with the resonant peaks of Figure 2.3 are the modes that can potentially contribute significantly to TMR. In the range 0-14 kHz these modes were the three suspension torsion modes (T1, T2, T3) and the suspension sway mode (S). The suspension bending modes (B1, B2, B3) and the flexure bending mode were the HGA modes that may contribute primarily to FHM.

2.2.2. The Actuator E-Block Unit

Figure 2.11 illustrates the solid model of the E-block unit. The *ANSYS* auto-mesh option was used to generate the FE mesh of this part, using 18075 *SOLID72* tetrahedral solid elements with 5156 nodes. Aluminum 6061-T6 material properties were used for the E-block, while aluminum material properties were used for the coil. These properties and the material properties used for the over-mold encapsulation (which is usually made of fiber-reinforced polyethylene sulfide) are listed in Table 2.1.

The E-block pivot was modeled using *BEAM4* elements, attaching the nodes on the inner surface of the E-block over-mold to a node at the center of the pivot core. This center node was constrained to have no translational DOFs and only one rotational DOF about the pivot axis, and it was connected using a *COMBIN14* torsional spring-damper element to a coincident node, which was constrained to have no degrees of freedom. This was done to simulate the so-called '*rigid body rotation mode*' of the actuator[15]. According to the material presented in [19], the natural frequency of the rigid body rotation mode is typically around 60 Hz and its modal damping ratio is around 0.06. These values were used to concoct the required stiffness $K_t = 0.5$ N· m and damping $c_t = 1.0$ mN· m· s for the spring-damper element.

The relevant natural frequencies and associated mode shapes of the E-block unit are listed in Table 2.3, and some of the mode shapes are illustrated in Figures 2.12 through 2.15. The over-mold section around the coil exhibited a large number of modes due to its lower stiffness. However, the effect of these modes on the dynamics of the slider was negligible and was ignored in this study. The arm bending and torsion modes were essentially the single arm modes coupling with one another in different in-phase and out-of-phase combinations. The motions of the outer arms, whether in-phase or out-of-phase, were typically of the same amplitude, whereas the middle arm exhibited a different amplitude. This observation is readily explained by the nearly symmetric conditions of the outer arms about the *x*-*y* plane. The rigid body mode, the *butterfly*[16] *mode*, and the E-

[15] This mode is called the rigid body rotation mode on account of its low frequency and its mode shape.
[16] The *butterfly mode* (Figure 2.12(b)) was given its name in industry on account of its shape. It is a bending mode about the *z* axis (passing through the E-block pivot) that resembles the first bending mode of a beam with free-free boundary conditions, with the arms and the coil moving in the same direction.

block arm sway and torsion modes can potentially contribute significantly to TMR. The E-block arm bending modes may contribute to FHM.

2.2.3. The Head Stack Assembly

The modeled HSA was a two-disk actuator with four suspension assemblies. The model was built by assembling the component models described in the preceding sections. The four HGAs were connected to the E-block arms my merging common nodes on the areas of the base-plate and the arms representing the swage area. The complete HSA model is depicted in Figure 2.16. The HSA model had a multitude of modes as a result of the dynamic coupling between its components. The relevant HSA frequencies are listed in Table 2.1, and some mode shapes are shown in Figures 2.17 through 2.26.

The results demonstrate that the coupling between the four HGAs generated several modes that can be grouped into sets corresponding to the familiar single-suspension modes. These sets typically consisted of four modes: two modes in which the two inner suspensions were moving (in-phase in one mode and out-of-phase in the other) while the two outer suspensions exhibited very little motion; and two modes where the two outer suspensions possessed most of the energy (in-phase in one mode and out-of-phase in the other) while the two inner suspensions had very little energy. The suspension modes also coupled with some of the E-block arm modes. The results indicate that there was a negative shift in the natural frequencies of the E-block unit relative to the component model. This was expected due to the added mass of the HGAs. The results also indicate that there was a negative shift in the natural frequencies of the HGA modes relative to the

component model. It is likely that this was due to the change in boundary conditions of the HGA, since its base-plate end was no longer completely fixed in space, but was allowed to move with the arm tip. It should be noted that, with the exception of the rigid body and butterfly modes, all the E-block arm modes in the frequency range considered invariably drove and coupled with some HGA modes. On the other hand, many of the modes in the various sets exhibited mode shapes with significant deformations in the HGAs only, and practically negligible deformations in the rest of the system. This suggests that HGA modes did not appreciably drive E-block modes, probably due to their inferior mass relative to the E-block. The labeling of the HSA mode shapes was based on observing the dominant mode in mode shape animations, under the guidance of the component results presented in §2.2.1 and §2.2.2.

The modes within the first, second, and third bending sets, and within the first and second torsion sets, had natural frequencies that were closely spaced in frequency, with differences of only a few kHz (less than 0.5% of the natural frequencies). The two arm sway modes of the component E-block unit coupled with the suspension sway mode yielding the two modes at 8.44 kHz and 8.52 kHz. These modes, however, were essentially driven by the arm sway modes. The suspension sway and third torsion modes occurred at natural frequencies that were close to the E-block arm first torsion modes. This resulted in several modes where the suspension dynamics coupled with the arm dynamics, in addition to the suspension sway and third torsion four-mode sets. For many of these modes, the mode shape was too complicated to allow more than a subjective assessment of whether the modes were driven primarily by suspension dynamics or by

arm dynamics. The spacing between these modes was in the range of 2-5% of their natural frequencies.

Figure 2.27 depicts the FRFs of the four sliders in the HSA representing the off-track response of the sliders to a unit rotational excitation at the E-block pivot (about the pivot axis). The modes excited were the modes that can potentially contribute to off-track motion, and can directly be associated with individual component modes that contribute to off-track motion. The FRFs are clearly more complex and denser with resonant peaks than that of the slider in the component HGA model (Figure 2.3). There were actually over forty modes for the HSA, compared with the five modes of the HGA, in the 0-14 kHz frequency range.

2.3. Conclusion

The dynamics of a two-disk HSA were investigated using FEA at the component and system levels. The main components of the HSA are the HGAs and the actuator E-block unit. The HGA sway and torsion modes and the E-block rigid body, butterfly, and arm sway and torsion modes were identified as modes that can potentially contribute significantly to off-track vibrations of the read-write head. The suspension bending modes and the E-block arm bending modes were identified as modes that may contribute to flying height variations.

In the HSA model, the coupling between the four HGAs generated several modes that can be grouped into sets corresponding to the familiar single-suspension modes. These

sets typically consisted of four modes: two modes in which the two inner suspensions were moving while the two outer suspensions exhibited very little motion, and two modes where the outer suspensions possessed most of the energy while the inner suspensions showed little energy. Some HGA modes were driven by E-block modes that were close in frequency. As a result of this coupling and of the coupling among the four HGAs, familiar suspension modes appeared over a wide frequency range.

The FRFs of the sliders in the HSA model were far more complex and dense in modes than that of the component HGA, and a response calculated using the HSA FRF is expected to be appreciably greater than that calculated using the FRF of a single HGA or even that of a single-arm, single-suspension assembly.

Material	***E* [GPa]**	***r* [kg/m^3]**	***n***
Stainless Steel	190	8072	0.32
Beam Material	393	0	0.23
Aluminum 6061-T6	69	2710	0.33
Aluminum	70	2710	0.33
Over-mold Material	0.1	1650	0

Table 2.1: Material properties used in FE modeling of the HGA.

Natural Frequency[17] **[Hz]**	**Mode Shape**
1570	Suspension first bending, B1
2890	Suspension first torsion, T1
4740	Suspension second bending, B2
7170	Suspension second torsion, T2
8010	Flexure bending
9130	Suspension third bending, B3
9540	Flexure torsion coupled with suspension second torsion
11440	Suspension sway, S
13320	Suspension third torsion, T3

Table 2.2: Natural frequencies and associated mode shapes of the HGA.

Natural Frequency[17] **[Hz]**	**Mode Shape**
60	Rigid body rotation mode
1710	Butterfly mode
2410	Arm first bending 1, ArmB1,1
2870	Arm first bending 2, ArmB1,2
3110	Arm first bending 3, ArmB1,3
8850	Arm second bending 1, ArmB2,1
9130	Arm second bending 2, ArmB2,2
9450	Arm second bending 3, ArmB2,3
9870	Arm sway 1, ArmS,1
11280	Arm sway 2, ArmS,2
11720	Arm first torsion 1, ArmT1,1
12660	Arm first torsion 2, ArmT1,2
13920	Arm first torsion 3, ArmT1,3

Table 2.3: Natural frequencies and associated mode shapes of the E-block unit.

[17] Natural frequencies are listed to the nearest 10 Hz.

Natural Frequency [Hz]	Mode Shape
60	Rigid body rotation mode
1470	Suspension first bending 1, B1,1
1480	Suspension first bending 2, B1,2
1480	Suspension first bending 3, B1,3
1490	Suspension first bending 4, B1,4
1670	Butterfly
2360	Arm first bending 1, ArmB1,1
2720	Suspension first torsion 1, T1,1
2720	Suspension first torsion 2, T1,2
2720	Suspension first torsion 3, T1,3
2720	Suspension first torsion 4, T1,4
2800	Arm first bending 2, ArmB1,2
3040	Arm first bending 3, ArmB1,3
4410	Suspension second bending 1, B2,1
4440	Suspension second bending 2, B2,2
4450	Suspension second bending 3, B2,3
4460	Suspension second bending 4, B2,4
6770	Suspension second torsion 1, T2,1
6780	Suspension second torsion 2, T2,2
6780	Suspension second torsion 3, T2,3
6780	Suspension second torsion 4, T2,4
8440	Arm sway 1 / suspension sway, ArmS,1/S
8520	Arm sway 2 / suspension sway, ArmS,2/S
8920	Suspension third bending 1, B3,1
8920	Suspension third bending 2, B3,2
8930	Suspension third bending 3, B3,3
8930	Suspension third bending 4, B3,4
10600	Arm first torsion 1 / suspension sway, ArmT1,1/S
10910	Suspension sway 1, S,1
11220	Suspension sway 2, S,2
11600	Suspension sway 3, S,3
11740	Suspension sway 4, S,4
12050	Arm first torsion / suspension sway, ArmT1/S
12140	Arm first torsion / suspension third torsion, ArmT1/T3
12750	Suspension third torsion 1, T3,1
12950	Suspension third torsion 2, T3,2
13080	Suspension third torsion 3, T3,3
13120	Suspension third torsion 4, T3,4
13520	Arm first torsion / suspension third torsion, ArmT1/T3

Table 2.4: Natural frequencies and associated mode shapes of the HSA.

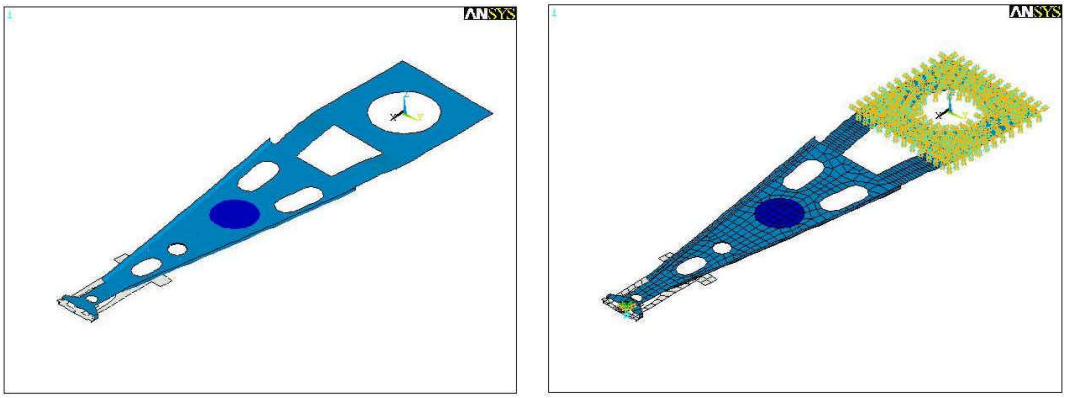

(a) Solid model (b) Finite element model

Figure 2.1: *ANSYS* model of the HGA.

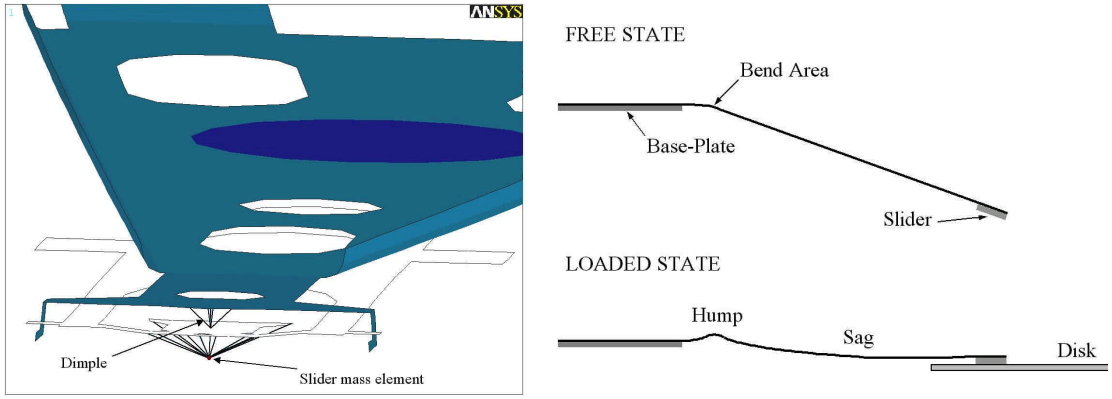

(a) Dimple and slider mass element (b) Suspension free and loaded states

Figure 2.2: Dimple and slider mass element; suspension free and loaded states.

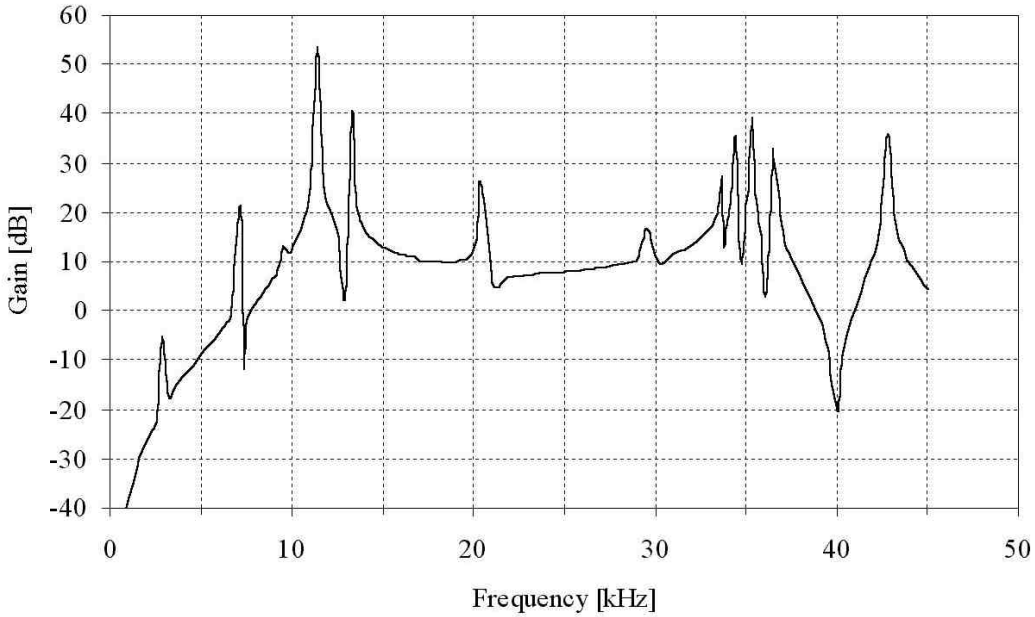

Figure 2.3: FRF of the slider to a unit lateral excitation at the base-plate.

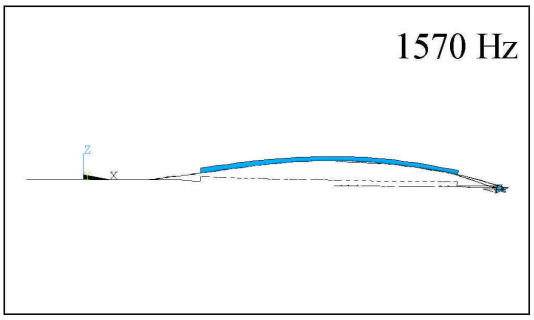

Figure 2.4: Suspension first bending.

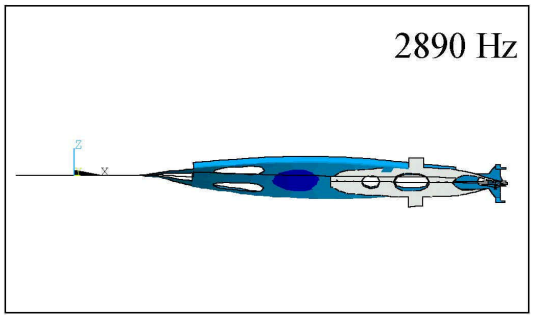

Figure 2.5: Suspension first torsion.

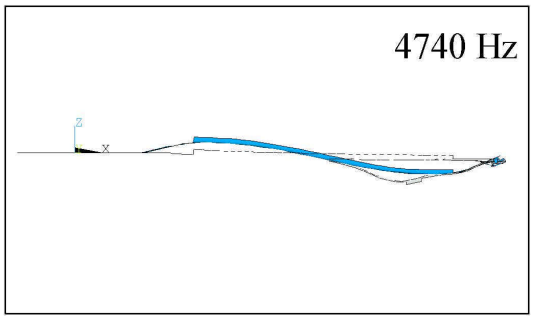

Figure 2.6: Suspension second bending.

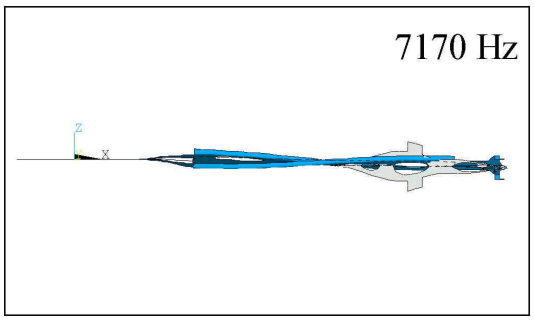

Figure 2.7: Suspension second torsion.

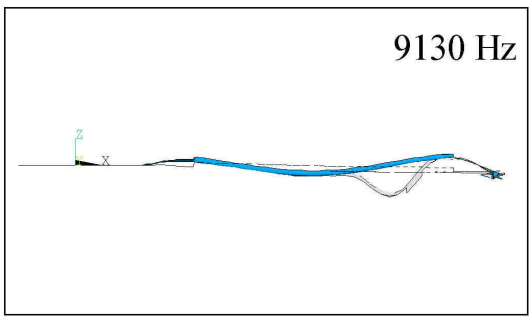

Figure 2.8: Suspension third bending.

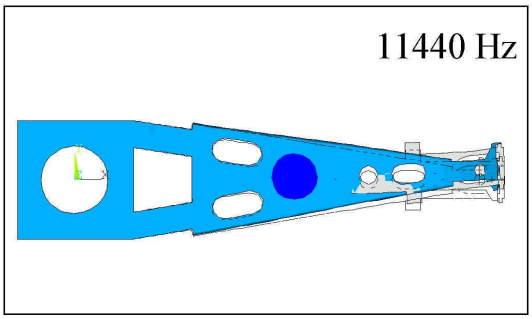

Figure 2.9: Suspension sway.

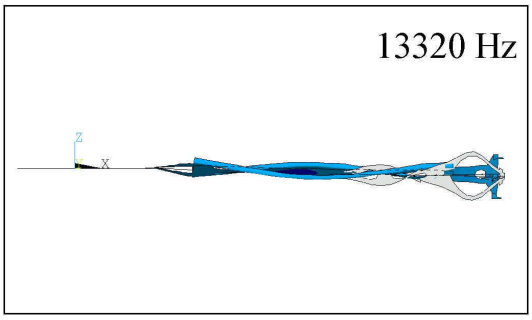

Figure 2.10: Suspension third torsion.

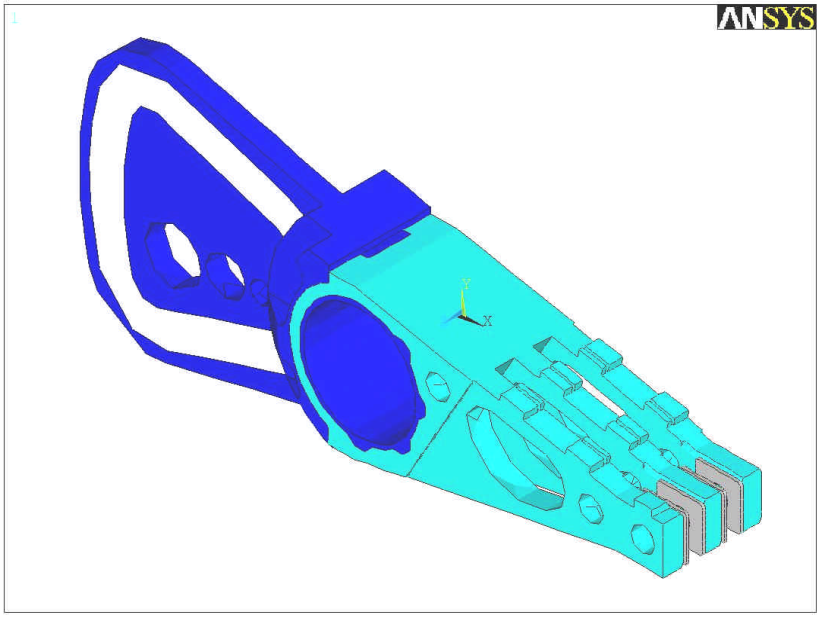

Figure 2.11: Solid model of E-block unit.

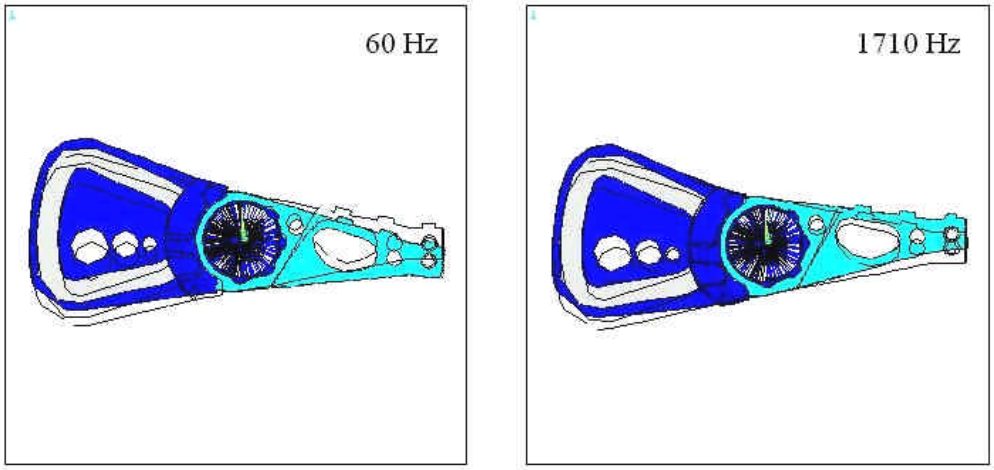

(a) Rigid body rotation mode (b) Butterfly mode

Figure 2.12: Rigid body rotation and butterfly modes.

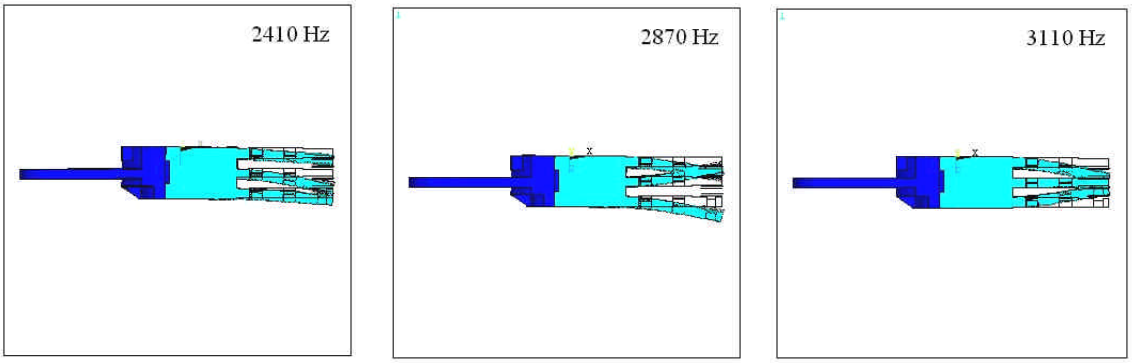

(a) Arm B1,1 (b) Arm B1,2 (c) Arm B1,3

Figure 2.13: Three first bending modes of the E-block arms.

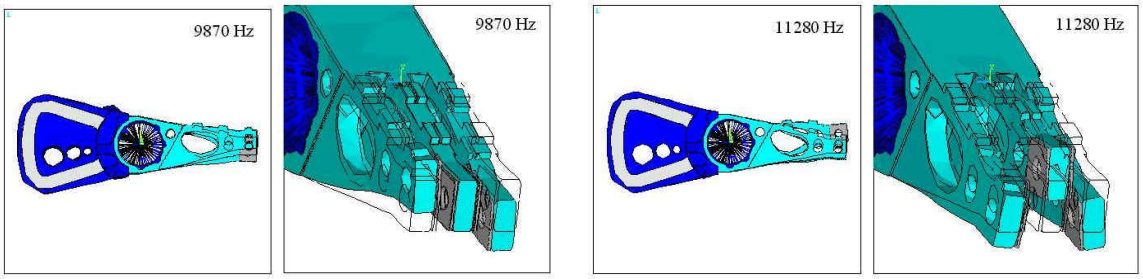

(a) Arm S,1: top and isometric views. (b) Arm S,2: top and isometric views.

Figure 2.14: Two sway modes of the E-block arms.

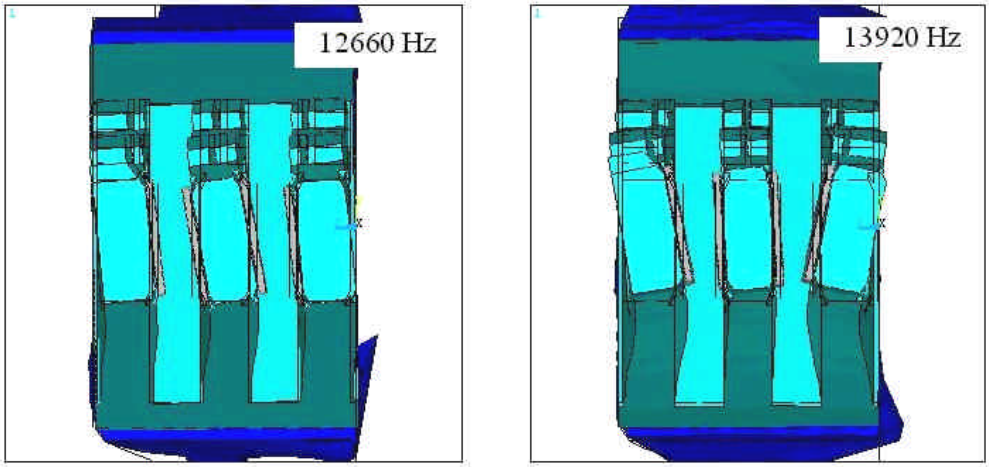

(a) Arm T1,2 (b) Arm T1,3

Figure 2.15: Two first torsion modes of the E-block arms.

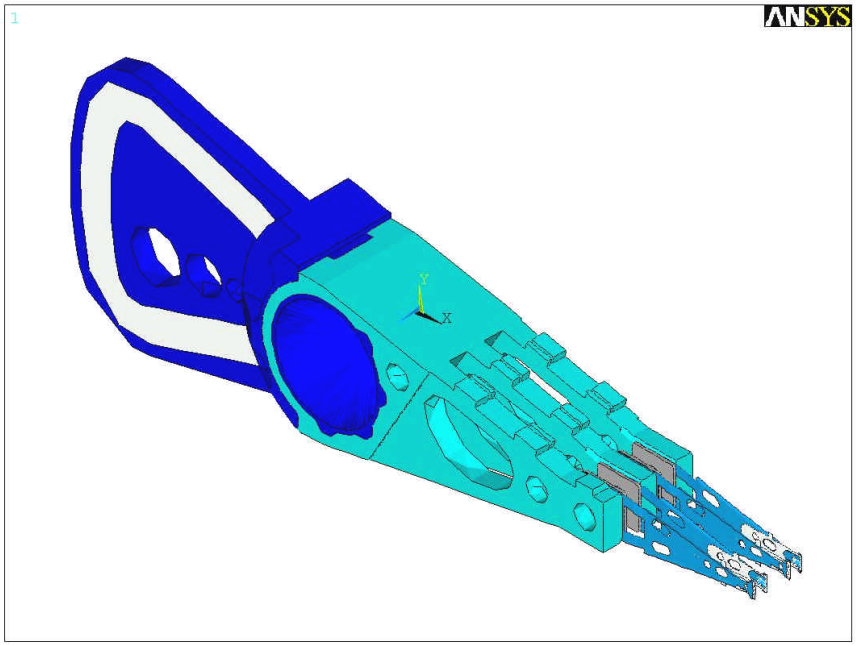

Figure 2.16: Solid model of HSA.

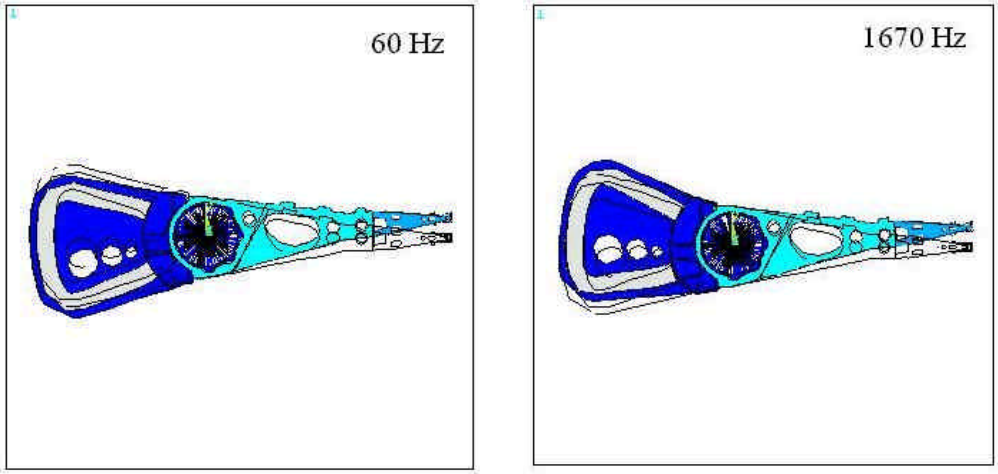

(a) Rigid body rotation mode (b) Butterfly mode

Figure 2.17: HSA rigid body rotation and butterfly modes.

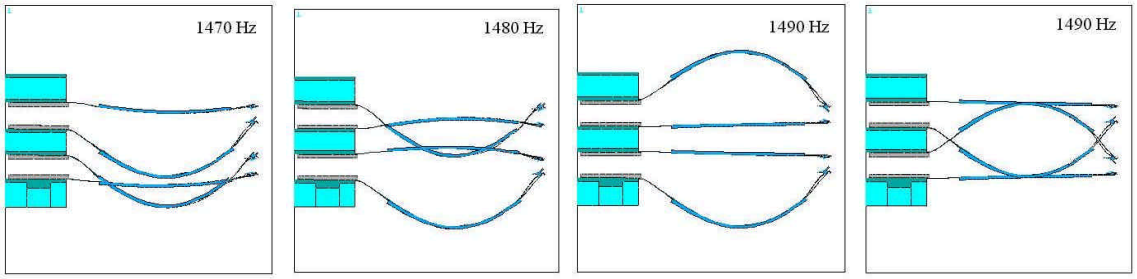

(a) B1,1 (b) B1,2 (c) B1,3 (d) B1,4

Figure 2.18: Four HSA suspension first bending modes.

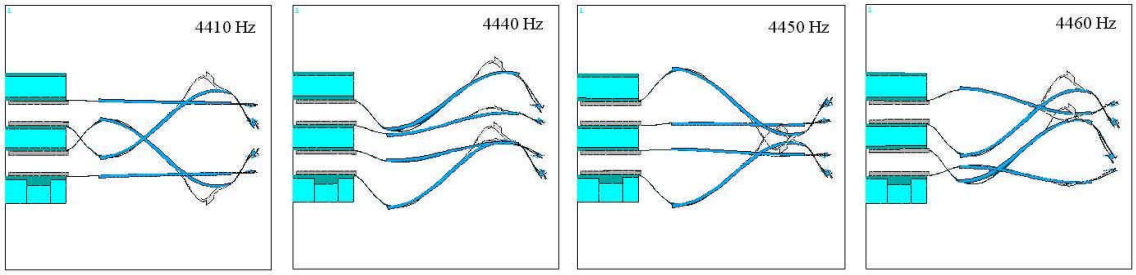

(a) B2,1 (b) B2,2 (c) B2,3 (d) B2,4

Figure 2.19: Four HSA suspension second bending modes.

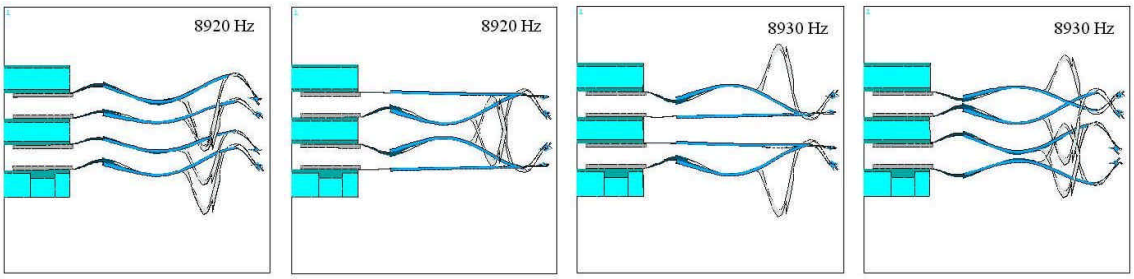

(a) B3,1 (b) B3,2 (c) B3,3 (d) B3,4

Figure 2.20: Four HSA suspension third bending modes.

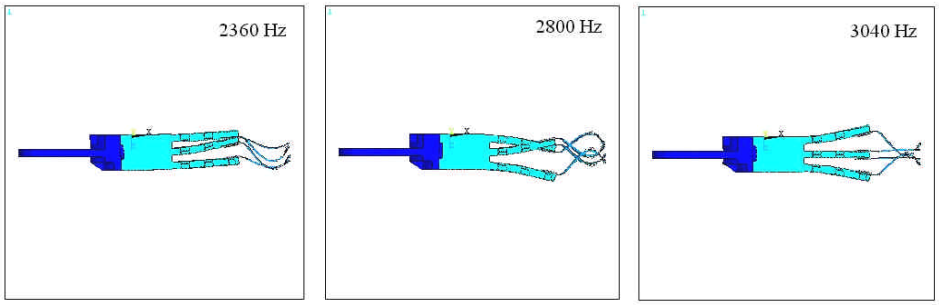

(a) Arm B1,1 (b) Arm B1,2 (c) Arm B1,3

Figure 2.21: Three HSA first bending modes of the E-block arms.

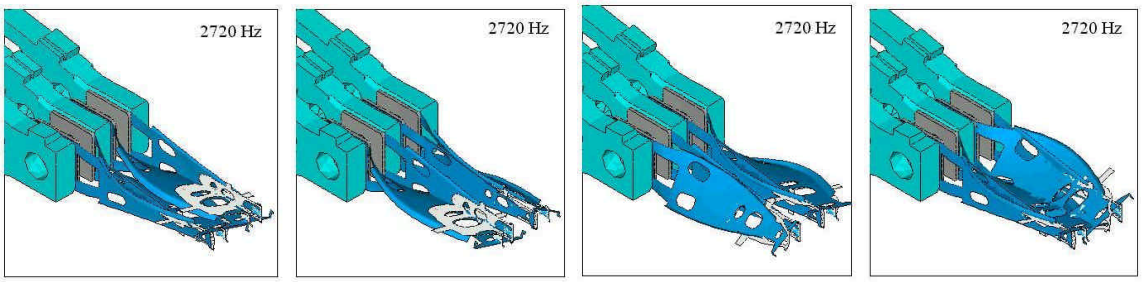

(a) T1,1 (b) T1,2 (c) T1,3 (d) T1,4

Figure 2.22: Four HSA suspension first torsion modes.

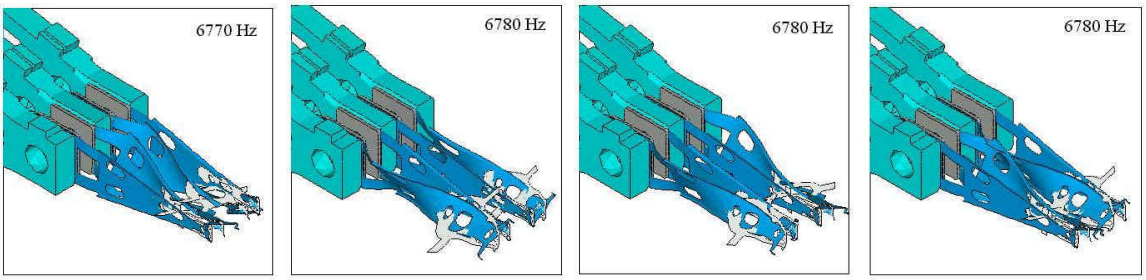

(a) T2,1 (b) T2,2 (c) T2,3 (d) T2,4

Figure 2.23: Four HSA suspension second torsion modes.

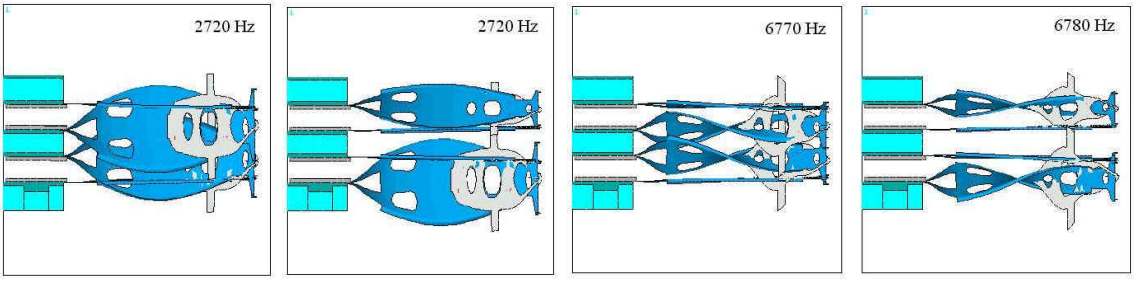

(a) T1,1 (b) T1,2 (c) T2,1 (d) T2,2

Figure 2.24: HSA suspension first and second torsion modes: side view.

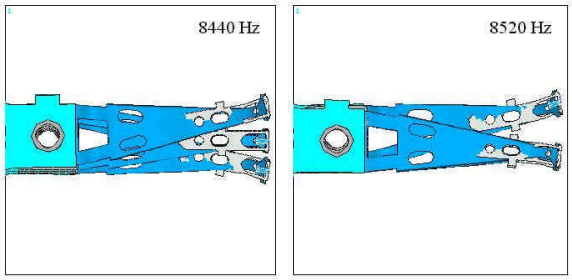

(a) ArmS,1/S (b) ArmS,2/S

Figure 2.25: Two HSA arm-sway/suspension-sway modes.

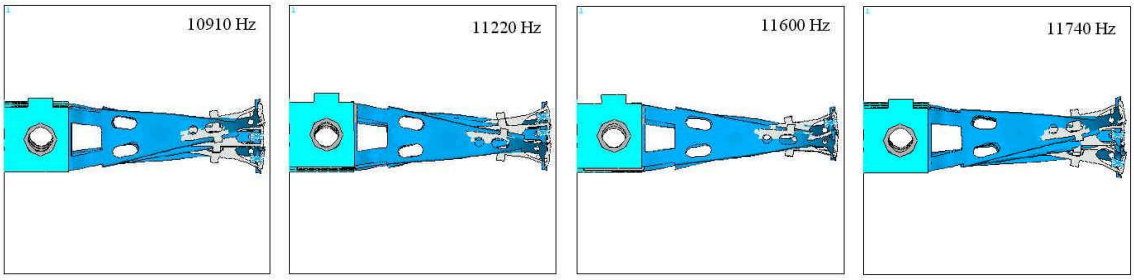

(a) S,1 (b) S,2 (c) S,3 (d) S,4

Figure 2.26: Four HSA suspension sway modes.

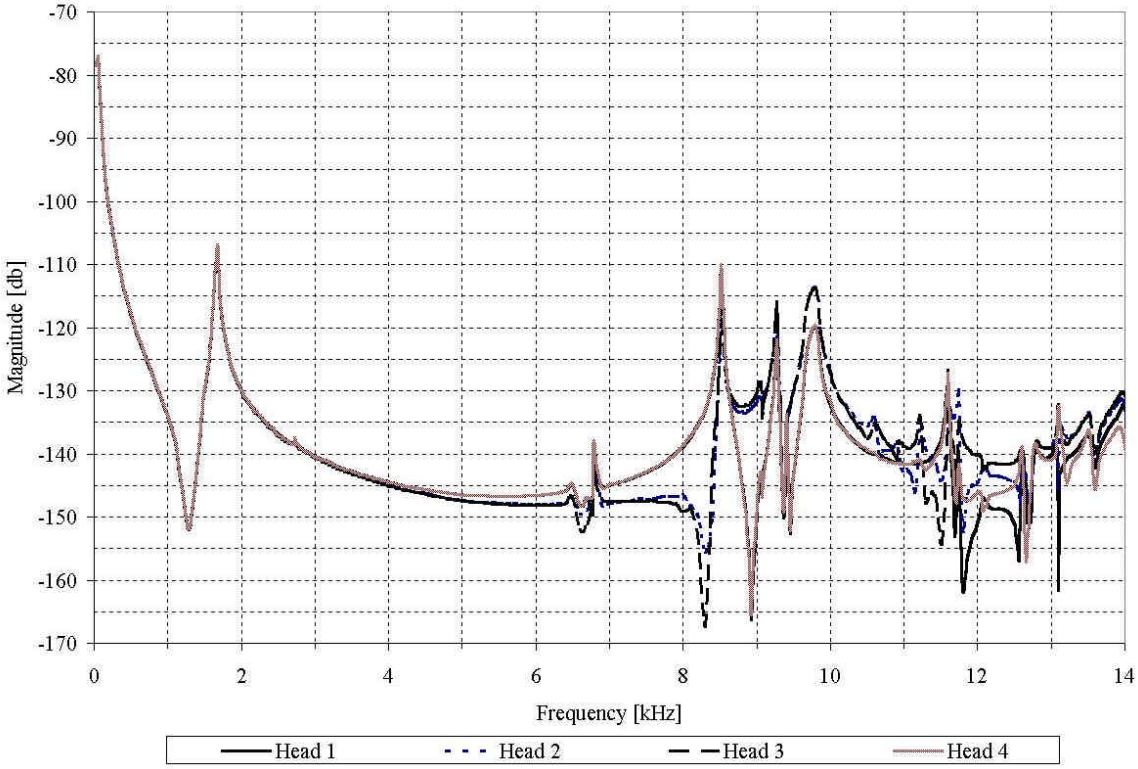

Figure 2.27: Off-track FRFs of heads in the HSA to a rotational excitation at the pivot.

CHAPTER 3

OPTIMAL STRAIN SENSOR PLACEMENT ON AN INSTRUMENTED SUSPENSION FOR SUPPRESSION OF OFF-TRACK VIBRATIONS IN HARD DISK DRIVES

3.1. Introduction

It is expected that for areal densities greater than 100 Gbit/in^2 the track density will increase at a higher rate than the linear bit density due to limitations in ultra-fast channel electronics. This will result in tighter TMR budgets, and will in turn impose a heavier burden on servo control. One of the primary problems of servo control in HDDs is the presence of flexible structures between actuation at the VCM and response at the head. In other words, it is non-collocated control. The suspensions and the E-block arms, body and pivot-bearing exhibit mechanical resonances that limit the closed-loop servo bandwidth.

It has been predicted for some time that servo control based solely on VCM actuation (commonly referred to as *single-stage actuation*) is reaching its performance limit, and that the use of *dual-stage actuation* should be considered by the HDD industry. Dual-stage actuation offers the use of a secondary actuator, with the VCM as the primary actuator, which is closer to the read-write heads than the VCM to achieve finer motion control of the heads. This would provide a higher servo bandwidth and an increased tracking accuracy. One option is to use two *piezo-electric actuators*, placed near the base of the suspension, to generate a push-pull action that would deform the suspension in sway. The deflection at the suspension tip would move the slider parallel to the disk

surface in the radial direction. Another option is to use a *MEMS-type micro-actuator* that would be inserted between the head and the suspension, allowing collocated control.

The use of strain sensors for active servo control in HDDs was proposed by several researchers [20], [21], [22] in order to increase the servo bandwidth. The basic idea was to strategically attach strain sensors to measure localized strains at key locations on drive structures, so that the sensors would effectively detect structural vibrations that may result in slider off-track motion. The measured strain information could then be used in active feedback control to damp out the resonances of those structures. *Huang et al.* [20] attached a strain sensor to the actuator and used an external feedback control loop to actively damp the E-block resonances, especially the butterfly mode. *Huang et al.* [21] attached strain sensors to the suspension, and fed the strain measurement back in an inner loop to actively damp the suspension resonances. With the active feedback damping achieved in [20] and [21], it was possible to design the servo controller to utilize a high open-loop gain to achieve a high closed-loop bandwidth.

In [23], it was proposed to use the strain sensor measurement not only for active feedback control, but also for active feedforward compensation of suspension vibrations. The idea was that the strain measurements would provide real-time suspension vibration information that can be fed forward to compensate for TMR resulting from suspension vibrations. The work was to be carried out on a piezo-electrically actuated dual-stage suspension as well as on a dual-stage suspension using a micro-actuator.

One of the main tasks in designing an instrumented suspension, for use in either of the control schemes described above, is determining the optimal location and orientation of the strain sensors in order to capture the dynamics of the desired modes: the modes that can contribute significantly to the off-track motion of the slider. The subject of optimal sensor and actuator placement on flexible structures was treated by several researchers, including *Lim* [24] and *Hac and Liu* [25]. *Hac and Liu* [25] proposed the use of some quantitative measure of the degree of observability of the modes under consideration in optimizing the sensor location. *Huang et al.* [21], applied the concepts presented in [25] and used the *observability gramian* to determine the optimal location and orientation for a strain gauge on a suspension. However, the results obtained in [21] were not in agreement with expectations based on the modal strain field distributions in the suspension.

Krinke [22] presented an implementation of an instrumented suspension prototype. Four strain gauges were used in the prototype, and were arranged in a *Wheatstone bridge* circuit as shown in Figure 3.1, in a configuration that would increase the sensitivity of the measurement. The configuration capitalized on the fact that certain high strain areas on the suspension are in opposite states of loading for the suspension off-track modes, and it was designed to optimize the sensitivity of measuring first torsion strains. The four sensor locations were determined by examining the strain distributions for the first torsion, second torsion, and sway modes, and selecting the regions possessing the highest levels of strain. The sensor orientations were selected as the principal strain angles of the strains generated by first torsion. The strain gauges used consisted of many deposited constantan

elements that formed a serpentine pattern at the prescribed angle, as shown in Figure 3.2, so as to increase the sensitivity of the strain measurement. The pattern was approximately 700 μm × 400 μm, with an element length of nearly 450 μm.

The objective of this study was to determine the optimal placement of strain sensors on a commercial suspension. The suspension used was *Hutchinson's* '*Magnum-5E*' piezo-actuated suspension. The study was conducted using FEA. The placement selection procedure was based on the theory presented by *Hac and Liu* [25], and it utilized the minimum eigenvalue of the observability gramian as a quantitative measure of the degree of observability of the suspension modes that could potentially contribute significantly to off-track motions. The formulation allowed for assigning weighting factors to the different modes to account for their contributions to off-track vibrations.

3.2. The State Space Realization and the Observability Gramian

A FRF, $a(s)$, can be expressed as the rational fraction of two polynomials, in the form

$$a(s) = \frac{\sum_{k=1}^{2n-2} b_k s^k}{\sum_{m=1}^{2n} a_m s^m}, \tag{3.1}$$

where $s = iw$ is the complex variable, w is the frequency of excitation, and n is the number of active modes in the frequency range of the FRF. $a(s)$ can also be expressed as the modal summation

$$a(s) = \sum_{k=1}^{n} \frac{p_k \overline{w}_k s + q_k \overline{w}_k^2}{s^2 + 2z_k \overline{w}_k s + \overline{w}_k^2}, \tag{3.2}$$

where $\overline{w}_k$, z_k, and p_k and q_k are the natural frequency, modal damping ratio, and residue coefficients, respectively, of the k[th] natural mode.

The process of matching or curve-fitting a selected model of a structure to its frequency response data to determine the modal parameters of the structure is widely referred to as *modal analysis*. Many methods are available for modal analysis. The method employed in this study was a variation of the *rational fraction polynomials* (*RFP*) method [26], which is a multi-degree-of-freedom frequency-domain method.

A state space realization of the transfer function is

$$\dot{\boldsymbol{x}} = \boldsymbol{A}\boldsymbol{x} + \boldsymbol{B}\boldsymbol{u}\,, \tag{3.3}$$

with the output equation

$$\boldsymbol{y} = \boldsymbol{C}\boldsymbol{x}\,, \tag{3.4}$$

where the matrices $\boldsymbol{A}$ and $\boldsymbol{B}$ are given by

$$\boldsymbol{A} = \begin{bmatrix} 0 & \overline{w}_1 & 0 & 0 & \dots & 0 & 0 \\ -\overline{w}_1 & -2z_1\overline{w}_1 & 0 & 0 & \dots & 0 & 0 \\ 0 & 0 & 0 & \overline{w}_2 & \dots & 0 & 0 \\ 0 & 0 & -\overline{w}_2 & -2z_2\overline{w}_2 & \dots & 0 & 0 \\ \vdots & \vdots & \vdots & \vdots & & \vdots & \vdots \\ 0 & 0 & 0 & 0 & \dots & 0 & \overline{w}_n \\ 0 & 0 & 0 & 0 & \dots & -\overline{w}_n & -2z_n\overline{w}_n \end{bmatrix}, \tag{3.5}$$

$$\boldsymbol{B} = \begin{bmatrix} 0 & \overline{w}_1 & 0 & \overline{w}_2 & \cdots & 0 & \overline{w}_n \end{bmatrix}^T, \tag{3.6}$$

and, for a single output system, $\boldsymbol{C}$ is given by

$$\boldsymbol{C} = \begin{bmatrix} p_1 & q_1 & p_2 & q_2 & \cdots & p_n & q_n \end{bmatrix}. \tag{3.7}$$

For a multi-output system with m outputs, $\boldsymbol{y}$ is an $m\times1$ column vector, and the output matrix $\boldsymbol{C}$ is an $m\times n$ matrix of the form

$$\boldsymbol{C}=\begin{bmatrix} p_1^1 & q_1^1 & p_2^1 & q_2^1 & \cdots & p_n^1 & q_n^1 \\ p_1^2 & q_1^2 & p_2^2 & q_2^2 & \cdots & p_n^2 & q_n^2 \\ \vdots & \vdots & \vdots & \vdots & & \vdots & \vdots \\ p_1^m & q_1^m & p_2^m & q_2^m & \cdots & p_n^m & q_n^m \end{bmatrix}. \tag{3.8}$$

The vibration of the instrumented suspension was to be measured in terms of the strains generated by the suspension motion. The output of the strain gauge used would depend upon both the location of the strain gauge and its orientation. Therefore, in the problem at hand, the system output of interest in identifying the optimal strain sensor placement is the strain e_q projected in a given direction, identified by the angle q from the x-axis. e_q can be computed once the plane strain components e_x, e_y, and g_{xy} are known, according to *Mohr's equation*

$$e_q = \frac{e_x + e_y}{2} + \frac{e_x - e_y}{2}\cos 2q + \frac{g_{xy}}{2}\sin 2q\ , \tag{3.9}$$

where e_x is the x-direction normal strain component, e_y is the y-direction normal strain component, and g_{xy} is the shear strain component. Eq. (3.9) can be expressed in matrix form as

$$e_q = \boldsymbol{C}_{\grave{e}}\mathring{\boldsymbol{a}}\,, \tag{3.10}$$

where

$$\boldsymbol{C}_{\grave{e}} = \begin{bmatrix} \frac{1+\cos 2q}{2} & \frac{1-\cos 2q}{2} & \frac{\sin 2q}{2} \end{bmatrix}, \tag{3.11}$$

and

$$\boldsymbol{\varepsilon} = \begin{bmatrix} \varepsilon_x \\ \varepsilon_y \\ \gamma_{xy} \end{bmatrix}. \tag{3.12}$$

The frequency range considered (0-20 kHz) contained four active suspension modes: first torsion, sway, second torsion, and third torsion. The FRFs of the strain components can therefore be expressed by Eq. (3.1) with $n = 4$. Thus, the state space formulation of the system has the form of Eq. (3.4) with $\boldsymbol{A}$ and $\boldsymbol{B}$ given by Eqs. (3.5) and (3.6), respectively, taking $n = 4$. An intermediate output matrix $\boldsymbol{C_{int}}$ (with the three strain components as outputs) can be written, according to Eq. (3.8), and setting $m = 3$, as

$$\boldsymbol{C_{int}} = \begin{bmatrix} p_1^x & q_1^x & p_2^x & q_2^x & p_3^x & q_3^x & p_4^x & q_4^x \\ p_1^y & q_1^y & p_2^y & q_2^y & p_3^y & q_3^y & p_4^y & q_4^y \\ p_1^{xy} & q_1^{xy} & p_2^{xy} & q_2^{xy} & p_3^{xy} & q_3^{xy} & p_4^{xy} & q_4^{xy} \end{bmatrix}. \tag{3.13}$$

The system output matrix is then given by

$$\boldsymbol{C} = \boldsymbol{C_{\varepsilon}}\,\boldsymbol{C_{int}}. \tag{3.14}$$

Structural conditions, such as *controllability* and *observability* play a vital role in the motion control of flexible structures. These conditions should not be violated by the arrangement of actuators and sensors on a structure. Otherwise, control performance objectives may not be achieved. Of particular interest in this study was the observability condition, which was directly governed by the sensor placement. For example, the placement of a sensor near a nodal point of a mode would yield erroneous information about the contribution of that mode to the system response.

The *observability gramian*, $\boldsymbol{W_o}$, of a system given by Eqs. (3.3) and (3.4) is defined by

$$\boldsymbol{W_o} = \int_0^\infty e^{\boldsymbol{A^T}t}\boldsymbol{C^T}\boldsymbol{C}e^{\boldsymbol{A}t}\,dt\ . \tag{3.15}$$

If the observability gramian of a system is nonsingular, then the system is observable; if the observability gramian is singular, then the system is not observable. This binary character of the notion of observability renders it unsuitable for direct application to the problem of determining the optimal sensor placement. *Hac and Liu* [25] proposed a methodology for determining the optimal sensor placement in active motion control of flexible structures. The proposed approach used the observability gramian of the system and relied on certain quantitative measures of its degree of observability. By noting that a system is considered to be completely observable if its observability gramian is nonsingular, regardless of how close to being singular the gramian might come, *Hac and Liu* suggested using the eigenvalues of the observability gramian as a measure of the degree of observability of the system [25].

A system with a nearly singular observability gramian (and equivalently some near-zero eigenvalues) is still strictly observable, but with a low degree of observability. In [25], *Hac and Liu* demonstrated that the eigenvalues of the observability gramian are directly related to the output energy of the system. The smallest eigenvalue of the gramian corresponds to the output energy of the least observable state of the system. The optimal sensor placement would be the one yielding the greatest minimum eigenvalue of the observability gramian, or equivalently, the least observable state with the greatest output

energy. The proposed optimality criterion for the sensor placement provides a balance between the importance of the lower order and the higher order modes.

For damped flexible structures, a closed form solution for the observability gramian exists, and, for a continuous-time system described by Eqs. (3.3) and (3.4), the gramian can be computed by solving the *Lyapunov equation*

$$\boldsymbol{A}^{\boldsymbol{T}}\boldsymbol{W}_{\boldsymbol{o}} + \boldsymbol{W}_{\boldsymbol{o}}\boldsymbol{A} + \boldsymbol{C}^{\boldsymbol{T}}\boldsymbol{C} = \boldsymbol{0}\,. \tag{3.16}$$

The existence of such a closed form solution rendered the method computationally inexpensive, requiring only the determination of the eigenvalues of the gramian at each step of optimization. Furthermore, the eigenvalues could be obtained in closed form for small structural damping and distinct, well-spaced natural frequencies.

The system output matrix $\boldsymbol{C}$ can be further modified to account for the different contributions of the modes under consideration to slider off-track motion. $\boldsymbol{C}$ would then be given by

$$\boldsymbol{C} = \boldsymbol{C}_{\dot{\boldsymbol{e}}}\boldsymbol{C}_{\boldsymbol{int}}\boldsymbol{C}_{\boldsymbol{w}}\,, \tag{3.17}$$

where $\boldsymbol{C}_{\boldsymbol{w}}$ is a weighting matrix that assigns a weighting factor to each of the modes.

The value of the amplitude of a modal coordinate at its matching resonance is called the *Q factor*, or *quality factor*, of that mode[18]. The frequency points at which the magnitude of the modal coordinate falls to 0.707 of the quality factor of that mode are called the

[18] in analogy with some electrical engineering applications

half-power points of the mode, and the frequency band between these two points is called the *bandwidth* of the mode. In this study, the entries of $\boldsymbol{C_w}$ were based on the contribution of each mode to the slider off-track motion over the bandwidth of the mode.

3.3. Finite Element Modeling and Analysis of the *Magnum-5E* Suspension

The HGA model built for the *Magnum-5E* suspension consisted of the suspension load-beam, the flexure, and the slider (Figure 3.3). The load-beam, the flexure, and the piezo-electric elements were modeled using 5686 4-node shell elements, with 6387 nodes. The material properties used for the load-beam and the flexure were those of stainless steel. They are listed, along with those used for the piezo-elements, in Table 3.1. The flexure attachment to the load-beam at the laser spot weld locations was modeled using *BEAM4* elements. The material used for the beam elements was assigned zero density and high stiffness, so as to provide the desired attachment without dynamically loading the system. The load-beam dimple was modeled using *BEAM4* elements. In order to model the point of contact between the dimple and the flexure, a node on the flexure coincident with the apex node of the dimple *BEAM4* elements was created, and the two nodes were constrained to have the same translational coordinates, but were allowed to rotate relative to one another.

The slider was modeled as a *MASS21* mass element, and was assigned the same inertial properties as those listed in §2.2.1 for a pico-slider. The slider mass element was positioned at the location of the center of gravity of the slider and was attached to the

flexure using beam elements. Air bearing dynamics were not considered in these analyses and the slider was considered to have a fixed flying attitude.

A modal analysis was performed to compute the modal parameters of the suspension over the 0-20 kHz frequency range. The relevant natural frequencies and associated mode shapes of the suspension in this range are presented in Table 3.2. A harmonic analysis was then performed to obtain the FRFs of the slider motion and the three plane strain components in all elements on the load-beam to a unit lateral excitation at the base-plate area. The 0-20 kHz frequency range contained four active suspension modes: first torsion, sway, second torsion and third torsion. These modes are depicted in Figure 3.4. Figure 3.5 shows the FRF of the slider off-track motion to a unit lateral excitation at the base-plate area. The response plotted is the slider motion relative to the base-plate motion. Figures 3.7, 3.8, and 3.9 show sample strain FRFs for the strain components e_x, e_y, and g_{xy}, respectively, at five arbitrary elements (marked in Figure 3.6). The vertical scale on these plots is the decibel of the absolute value of each FRF (which is generally a complex quantity), with the reference taken as 1 unit. It should be noted that a damping ratio of 0.0013 was imposed during the harmonic analysis in *ANSYS*. This value was an estimate of the average modal damping ratio based on unpublished experimental results.

An examination of the strain intensity distributions corresponding to the four active natural modes indicated that the bend area and the central region between the bend area and the base-plate exhibited the highest levels of strain for all four modes. Close-up views of the strain intensity distributions around these areas for the four modes are given

in Figure 3.10. Blue and red indicate the lowest and highest levels, respectively, of strain intensity in the contour color scale. It should be noted that the four distributions have different scales, and a comparison of strain levels across the different modes would be meaningless.

The modified RFP method used for modal analysis was coded in MATLAB, and the modal parameters (natural frequencies, modal damping factors, and modal residues) associated with each strain FRF were computed for each element on the suspension load-beam. The computed parameters were then used in building the system matrices as given by Eqs. (3.5), (3.6), and (3.13).

3.4. Optimization Results

After constructing the system matrices at each element on the load-beam, the strains were projected at angles in increments of 1° at each of these elements. The observability gramian and its eigenvalues were then computed for each element/strain-projection-angle combination according to Eqs. (3.15) and (3.16). The element/projection-angle combination yielding the greatest minimum eigenvalue of the gramian was identified as the optimal sensor placement. The entire procedure was carried out twice using MATLAB. In the first run, the output matrix given by Eq. (3.14) was used, with the weighting matrix $\boldsymbol{C_w}$ set to the identity matrix $\boldsymbol{I}$, so that all modes were assigned equal relevance. In the second run, the output matrix given by Eq. (3.17) was used with the weighting matrix $\boldsymbol{C_w}$ set to $\boldsymbol{C_h}$, where $\boldsymbol{C_h}$ is a matrix whose entries were calculated based

on the contribution of each mode to the slider off-track motion over the bandwidth of the mode, normalized by the total off-track motion in the 0-20 kHz range (Table 3.3).

The optimal sensor placement for the first case where $\boldsymbol{C_w} = \boldsymbol{I}$ was at element 559, at an angle of 92°, as shown in Figure 3.11. However, the results presented in Figure 3.11 were expected to be of little practical use due to the small size of the selected element. On average, the element dimensions in the bend area were approximately 100 μm in the *x*-direction by 75 μm in the *y*-direction, whereas target dimensions for implementing an instrumented suspension at *CML* are 100 μm × 225 μm, or, equivalently, a three-element strip: one element long in the *x*-direction and three elements long in the *y*-direction. In order to provide more applicable results, it was necessary to identify larger regions at which the minimum gramian eigenvalues assumed the highest values for certain directions. There were four such regions, as depicted in Figure 3.12. Red represents the highest gramian minimum eigenvalue level in the color scale.

The orientation of the strain sensor in each element strip was based on the average minimum eigenvalue of the three elements in the strip. The strain projection angle yielding the highest average minimum eigenvalue was identified as the optimal sensor orientation at the corresponding element strip. Figure 3.12 indicates the optimal projection angle for each of the selected regions, and Table 3.4 lists the associated average minimum eigenvalues. Region R1 represents the best location for a single strain sensor. However, the degrees of observability at regions R2, R3, and R4 are only slightly

lower than that at R1, and strain sensor placement at any of these regions (with the specified orientation) is expected to yield comparable results to those obtained using R1.

The results presented in Figure 3.12 are especially useful for implementations of the instrumented suspension similar to that presented in [22], in which four strain gauges are arranged in a *Wheatstone* bridge circuit to increase the sensitivity of the measurement. Such a configuration utilizes the fact that two pairs of regions are in opposite states of loading for all modes: pair R1-R4 is in tension (compression) during the time pair R2-R3 is in compression (tension) for the three torsion modes; and pair R1-R3 is in tension (compression) during the time pair R2-R4 is in compression (tension) in the sway mode. For the *Magnum-5E* suspension, sway was the major contributor to slider off-track motion, which suggests using a *Wheatstone* configuration that would maximize the measurement sensitivity to the sway mode.

The second case was conducted with $\boldsymbol{C_w} = \boldsymbol{C_h}$. The optimal sensor placement for this case was at element 559, at an angle of 92° (Figure 3.11). Note that this result is identical to that obtained using $\boldsymbol{C_w} = \boldsymbol{I}$. The four three-element strips at which the minimum gramian eigenvalues assumed their highest values for certain directions are identified in Figure 3.13. The optimal orientation of the strain sensors for these element strips was based on the average minimum eigenvalue of the three elements in the strip. Figure 3.13 indicates the optimal projection angle for each of the selected regions, and Table 3.4 lists the associated average minimum eigenvalues. The optimal sensor placement was quite similar to the one obtained using $\boldsymbol{C_w} = \boldsymbol{I}$.

3.5. Conclusion

The objective of this study was to determine the optimal placement of strain sensors on a commercial suspension, the *Magnum-5E* suspension. The optimal placement selection procedure was based on maximizing the degree of observability of the suspension first torsion, sway, second torsion, and third torsion modes, which are the modes that could potentially contribute significantly to slider off-track motion. The minimum eigenvalue of the observability gramian was used as a quantitative measure of the degree of observability of these modes.

The optimal sensor location and orientation on the suspension load-beam were identified for two cases: in the first, equal weighting factors were assigned to all modes; in the second, weighting factors based on the modal contributions to the slider off-track motion were assigned to the modes. Both cases yielded the same result. The optimal location was on the load-beam bend area. In addition, the four locations on the suspension load-beam with the highest degree of observability of the selected modes were identified for implementations of the instrumented suspension in which four strain gauges are arranged in a *Wheatstone* bridge circuit, in a configuration that would increase the sensitivity of the measurement. The results obtained for the two cases described above were nearly identical.

Material	***E* [GPa]**	***G* [GPa]**	***r* [kg/m^3]**	***n***
Stainless Steel	180	68.182	8072	0.32
Piezo-element material	62	23.485	7800	0.32
BEAM4 material	280	80.000	0	0

Table 3.1: Material properties[19] used in the FE model of the *Magnum-5E*.

Frequency [Hz]	Mode Shape
2730	First bending
5420	Second bending
6740	First torsion
8640	Sway
9640	Third bending
12120	Second torsion
14950	Fourth bending
15740	Third torsion

Table 3.2: Natural frequencies and mode shapes of the *Magnum-5E*.

Mode	**T1**	**S**	**T2**	**T3**
Weighting Factor	0.0167	0.9129	0.0593	0.0111

Table 3.3: Weighting factors used in $\mathbf{C_h}$.

Region	**Optimal Projection Angle**		**Average Minimum Eigenvalue**	
	$C_w = I$	$C_w = C_h$	$C_w = I$	$C_w = C_h$
R1	91°	91°	22.4×10^{-9}	27.4×10^{-13}
R2	89°	89°	22.2×10^{-9}	27.1×10^{-13}
R3	86°	88°	19.9×10^{-9}	24.9×10^{-13}
R4	94°	92°	19.6×10^{-9}	24.5×10^{-13}

Table 3.4: Optimization results.

[19] These material properties were supplied by Hutchinson Technology Inc.

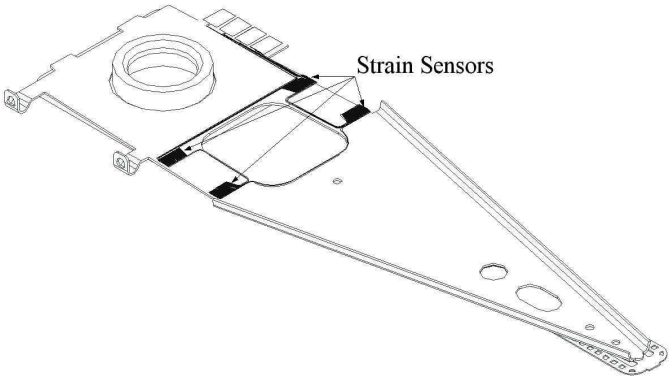

Figure 3.1: *Wheatstone* bridge strain gauge configuration[20].

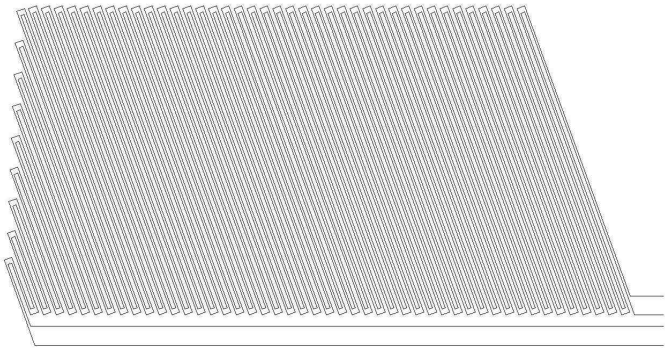

Figure 3.2: Strain gauge consisting of serpentine pattern of constantan elements[20].

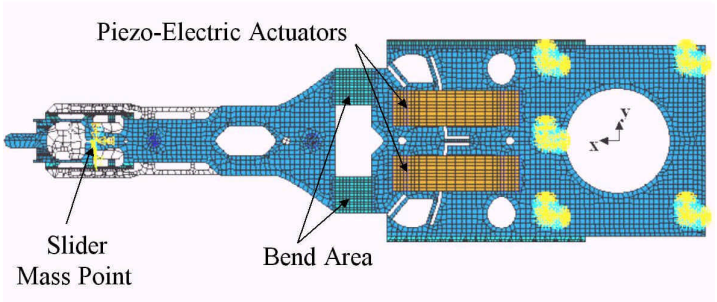

Figure 3.3: FE model of the *Magnum-5E* suspension.

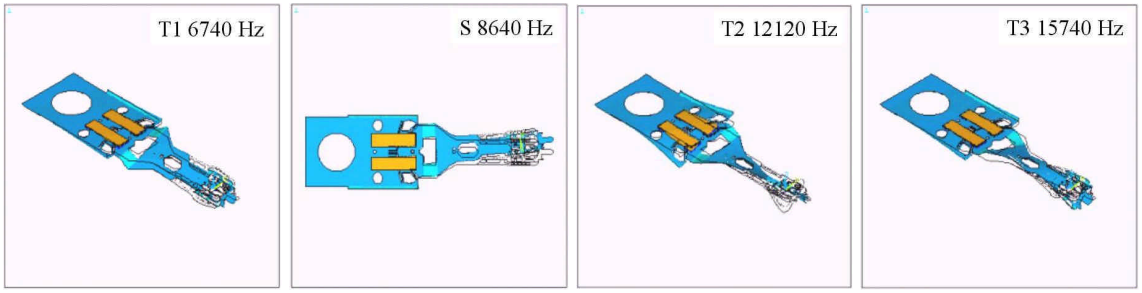

Figure 3.4: Suspension modes that contribute to off-track vibration.

[20] Figures courtesy of *Todd Krinke*, *Hutchinson Technology Inc*.

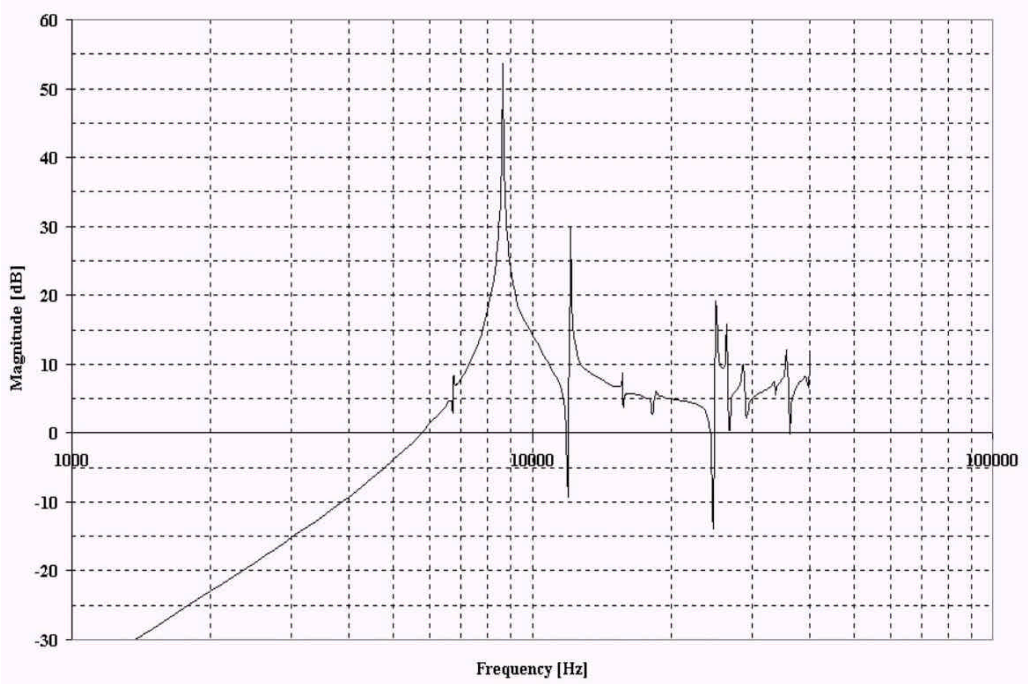

Figure 3.5: FRF of slider off-track to a unit lateral excitation at the base-plate area.

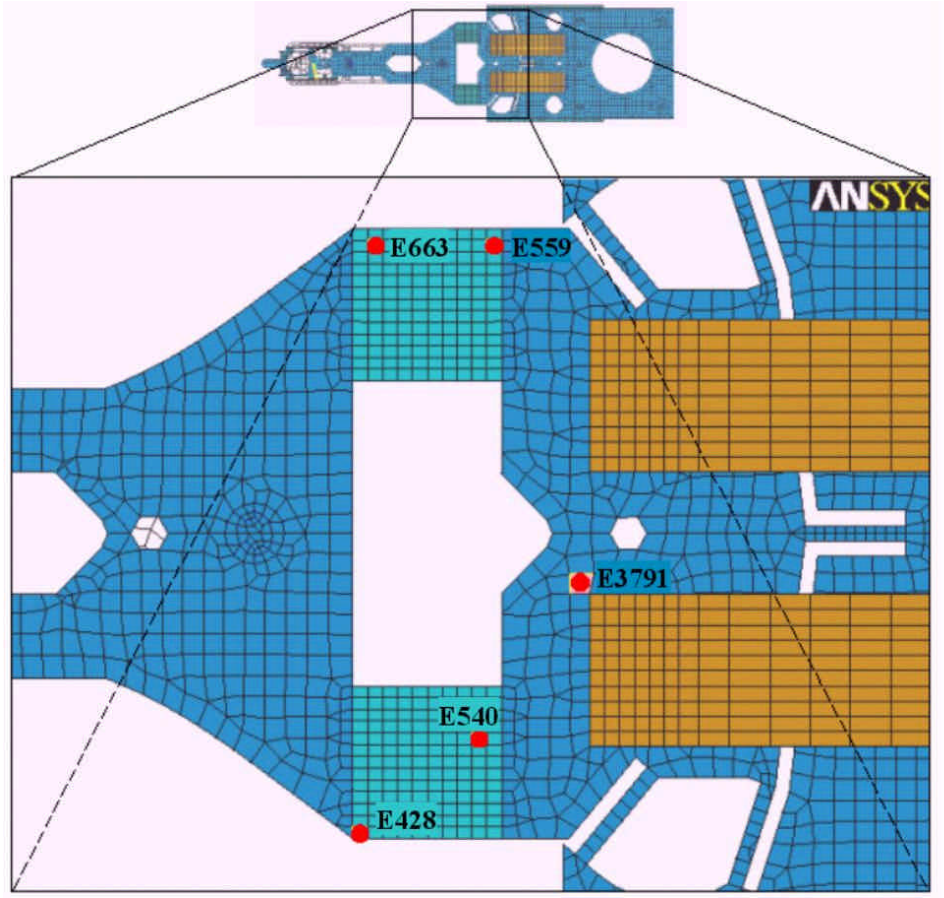

Figure 3.6: Close-up of central region on suspension; five arbitrary sample elements.

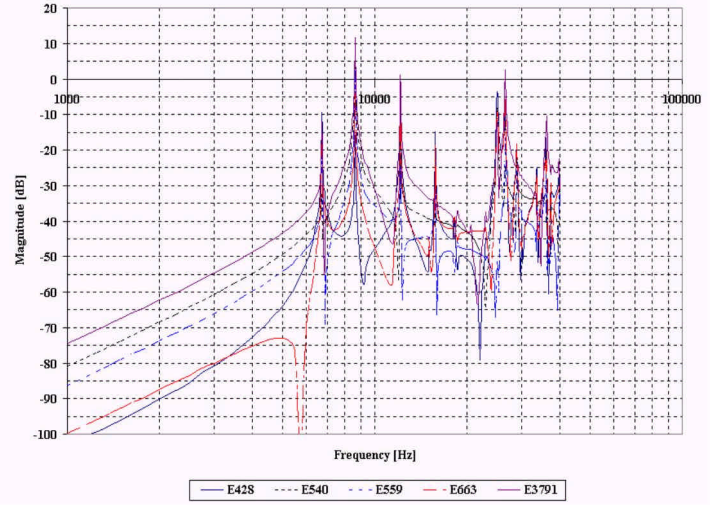

Figure 3.7: Five sample FRFs of the normal strain component e_x.

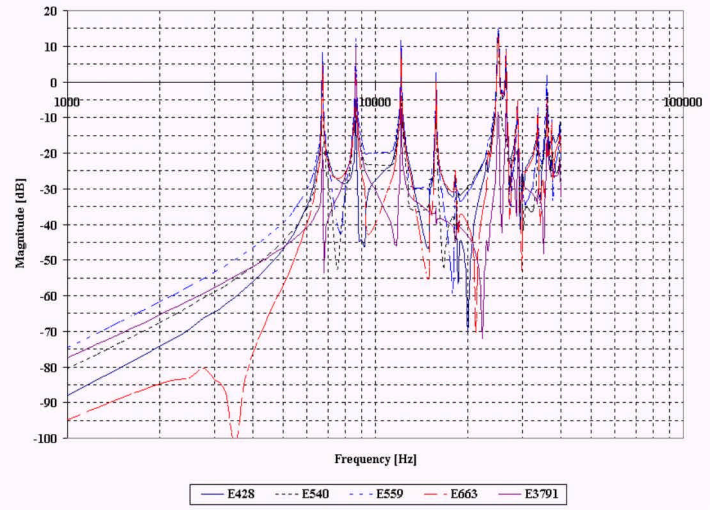

Figure 3.8: Five sample FRFs of the normal strain component e_y.

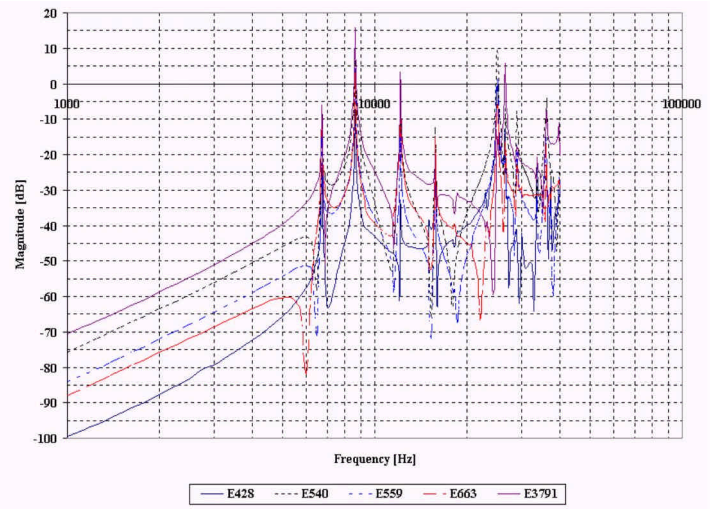

Figure 3.9: Five sample FRFs of the shear strain component g_{xy}.

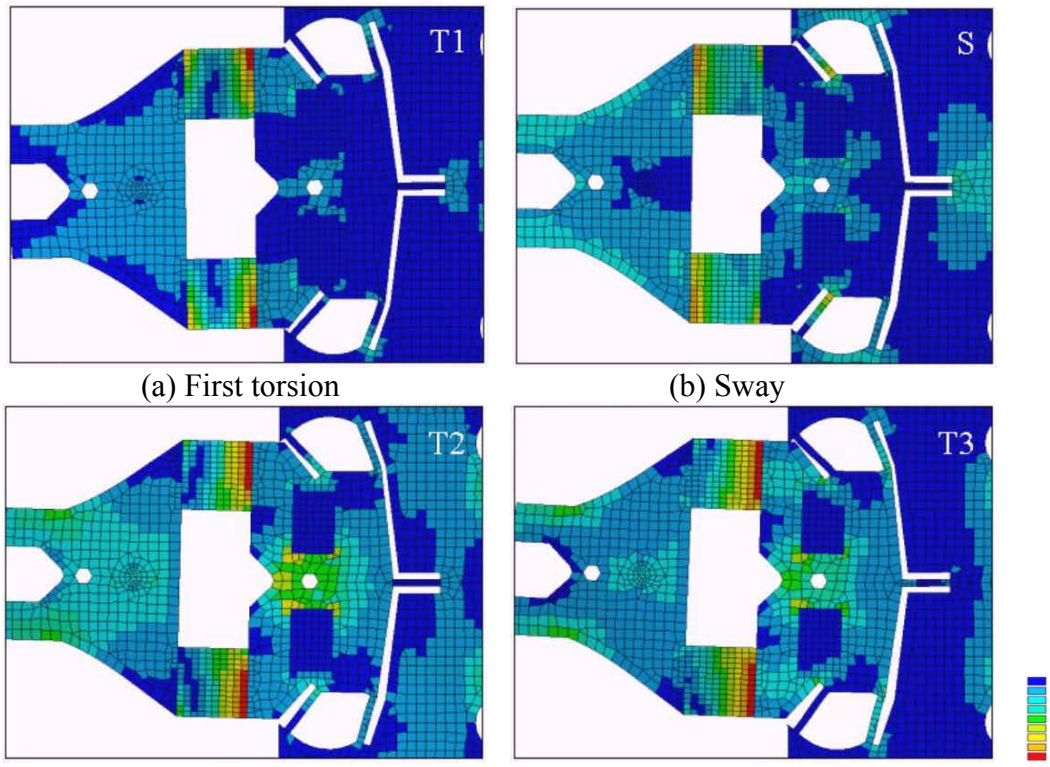

(a) First torsion (b) Sway

(c) Second torsion (d) Third torsion

Figure 3.10: Strain intensity distributions for T1, S, T2, and T3.

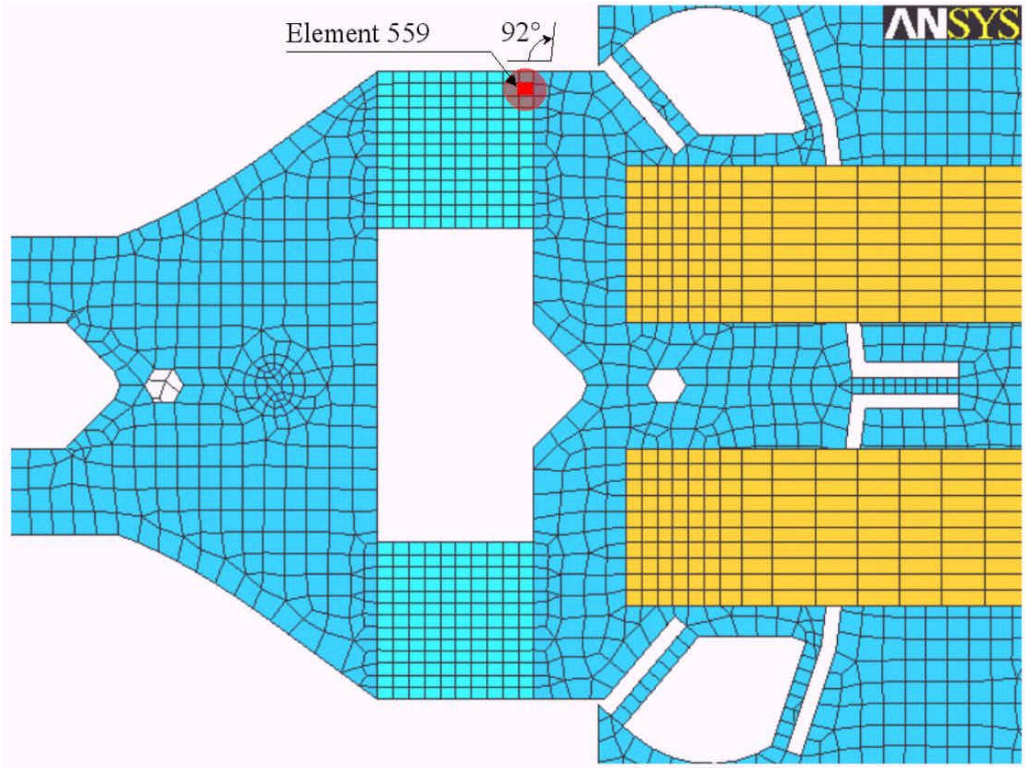

Figure 3.11: Optimal sensor placement for $\boldsymbol{C_w} = \boldsymbol{I}$, and for $\boldsymbol{C_w} = \boldsymbol{C_h}$.

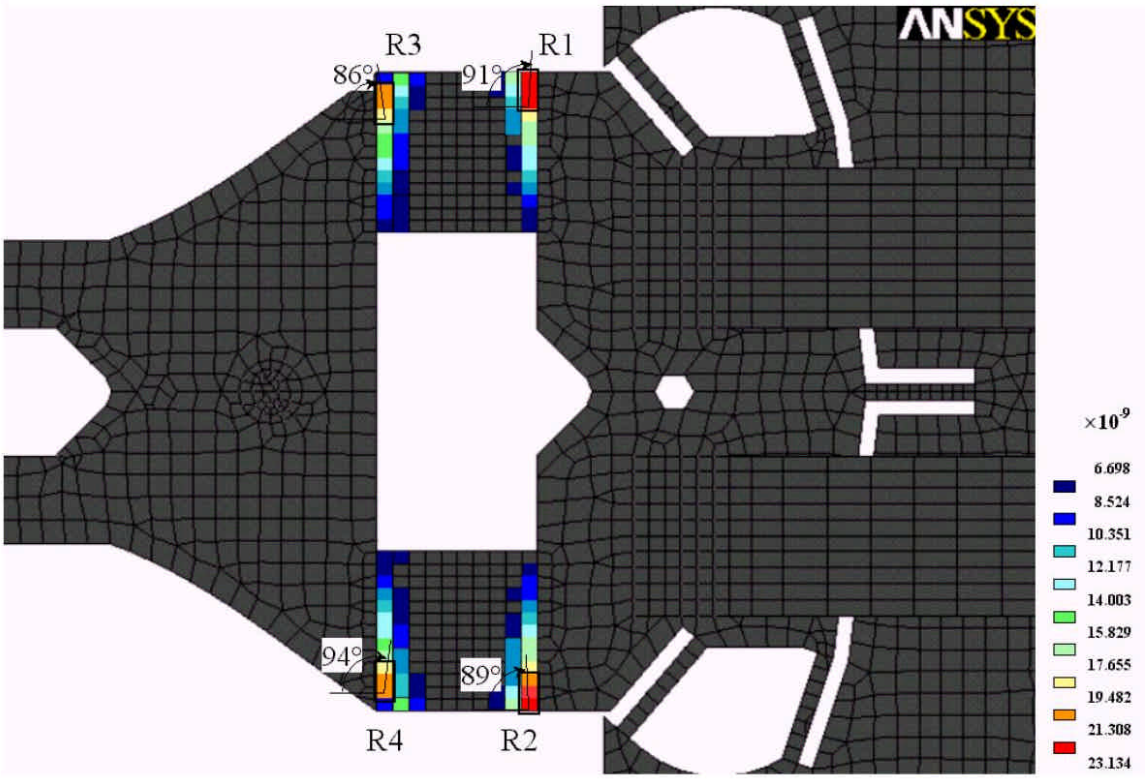

Figure 3.12: Regions with the highest minimum eigenvalues for $\boldsymbol{C_w} = \boldsymbol{I}$.

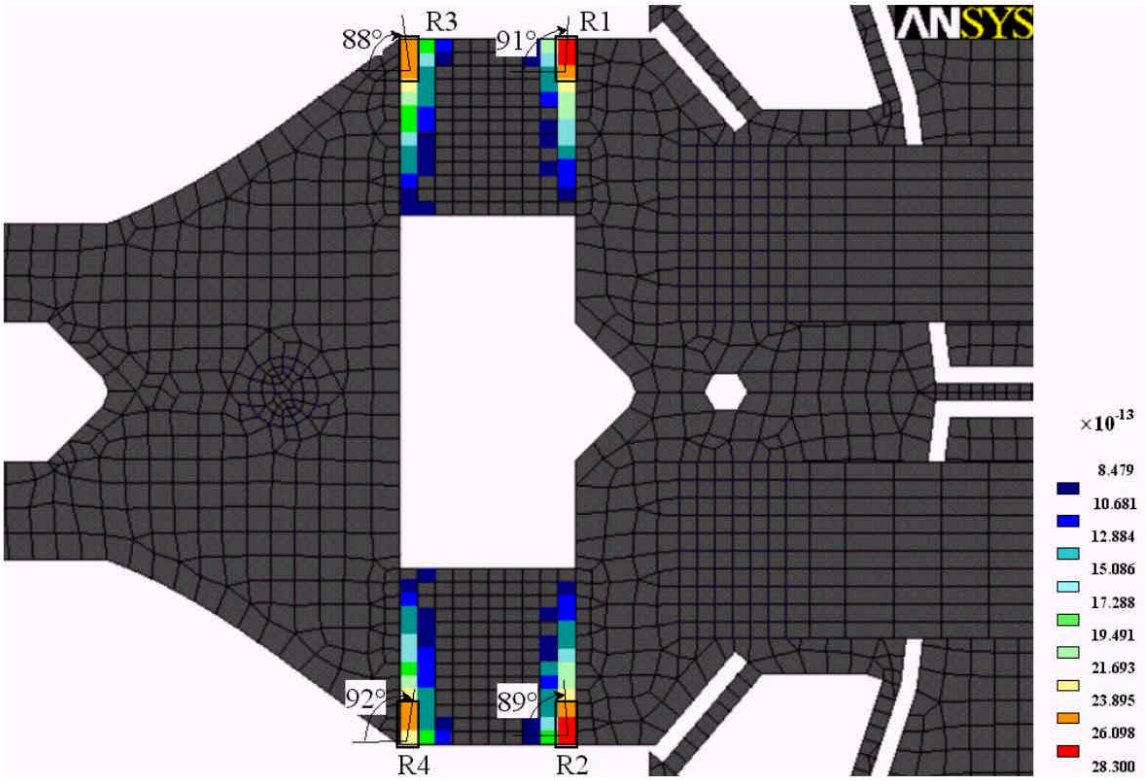

Figure 3.13: Regions with the highest minimum eigenvalues for $\boldsymbol{C_w} = \boldsymbol{C_h}$.

CHAPTER 4

THE EFFECTS OF E-BLOCK ARM THICKNESS ON HEAD OFF-TRACK VIBRATION AND AIRFLOW IN A MODELED HARD DISK DRIVE

4.1. Introduction

In addition to controlling the temperature distribution and the concentration and transfer of particulates within the drive, the flow field in the drive and any large scale fluid structures it may contain constitute a significant disturbance to the read-write head motion, as they excite the structural modes of the HSA and the disks, inducing TMR and FHM. Consequently, it is of paramount importance to understand the nature and characteristics of the airflow in disk drives, as well as its impact on structural vibrations, if the performance of future generation drives is to be improved.

Early research on the effects of airflow in HDDs on suspension vibration was carried out by *Yamaguchi et al.* [27]. The findings in [27] indicated that the amplitude of suspension vibration was proportional to the square of the speed of the approaching flow. In subsequent research by *Yamaguchi et al.* [28] and *Takuyama et al.* [29], the flow around a suspension was measured using hot-wire anemometry to identify the sources of suspension vibration, and numerical simulations of the flow were performed. It was shown in [28] and [29] that suspension vibration was caused by the turbulence behind the suspension cross-section, and that employing an aerofoil shape for the suspension cross-section could reduce its vibration.

Investigations of the flow in disk drives have been carried out in configurations of varying degrees of geometric complexity. The fully-enshrouded assembly of co-rotating disks, with no obstructions inserted between the disks, was one of the simplest configurations considered, and was studied by several researchers including *Lennemann* [30], *Abrahamson et al.* [31], *Schuler et al.* [32], *Tzeng and Humphrey* [33], *Humphrey et al.* [34], and *Iglesias and Humphrey* [35]. *Lennemann* [30] used aluminum flake flow visualization in a water flow model and observed a laminar central core of fluid with a highly turbulent outer region. The core had a lobed or polygonal shape, extended from the hub to the periphery of the disks, and it rotated at about 80% of the disk rotation speed.

Abrahamson et al. [31] used a dye injection flow visualization technique in a water flow model and refined *Lennemann's* conclusions. They characterized the flow structure as consisting of three distinct regions. The first was an inner region dominated by rotation effects. This region moved in rigid body rotation, exhibiting little or no motion relative to the disks, and was observed to extend from the hub to approximately 75% of the disk diameter. The second region was a shroud boundary layer region, which was dominated by viscous effects due to the no-slip condition at the shroud wall. This region was observed to extend inward from the shroud to approximately 90% of the disk diameter. The third region was an outer region, which occupied the space between the inner region and the shroud boundary layer region. It experienced a mixture of rotational and viscous effects, which resulted in the formation of large, periodic, axially-aligned vortical structures that rotated counter to the disk rotation. These vortices were polygonal in shape

and nearly uniform in size, spanning the radial extent of the outer region. The inner and outer regions were both predominantly 2-dimensional, whereas the shroud boundary layer region exhibited significant mean 3-dimensional motion.

Schuler et al. [32] and *Tzeng and Humphrey* [33] experimentally investigated the airflow in the unobstructed space between a pair of disks using *laser Doppler anemometry* (*LDA*). Their flow measurements along radial lines showed the flow to be divided into two main regions: an inner region in rigid body rotation whose mean flow speed was approximately equal to the local disk surface speed; and an outer region whose mean flow speed relative to the disk surface speed decreased linearly between the inner region and the disk edge. Their flow measurements along lines parallel to the spin axis revealed that the mean flow speed was fairly uniform along this direction.

Humphrey et al. [34] carried out numerical simulations to investigate the unsteady motion of the flow in the unobstructed space between a pair of fully-shrouded co-rotating disks. They performed 2-dimensional (axisymmetric) and 3-dimensional calculations in a configuration corresponding to the experimental setup employed by *Schuler et al.* [32]. Their 2-dimensional simulations predicted that for Reynolds numbers[21] $Re < 22200$, the flow exhibited a pair of counter-rotating toroidal vortices in the cross-stream plane. For $Re > 22200$, the flow was unsteady periodic, and the symmetry of the motion of the flow about the mid-plane was broken by alternating periodic crossings of the toroidal vortices. 3-dimensional numerical simulations at $Re = 22200$ and 44400 further revealed that the

[21] The definition of the Reynolds number is given in Eq. (4.20). The Reynolds number in [34] was based on the disk radius and the tip speed of the disks.

toroidal vortices acquired a time-varying sinuous shape in the circumferential direction, and that the rigid-body rotation region contained very weak secondary motions.

Iglesias et al. [35] numerically investigated the flow field between co-rotating disks that were fully shrouded by a cylindrical wall, and concluded that there were significant vertical velocity fluctuations at the disk outer region, which resulted in disk flutter.

The flow field between co-rotating disks is dramatically altered by the insertion of an arm between the disks to simulate the E-block arms of the HSA. The effects of radially-oriented obstructions between co-rotating disks was studied by several researchers including *Lennemann* [30], *Tzeng and Humphrey* [33], *Usry et al.* [36], *Harrison et al.* [37], *Gor et al.* [38], *Abrahamson et al.* [39], and *Suzuki and Humphrey* [40]. *Tzeng and Humphrey* [33] and *Usry et al.* [36] used LDA to investigate the effects of relatively thin obstructions, with an obstruction thickness, t, to disk-to-disk spacing, S, ratios of t/S = 0.25 and t/S = 0.21, and blockage factors[22] b in the range of 7% ≤ b ≤ 16%. They presented radial and axial mean and rms circumferential velocity profiles of the flow between the disks in the presence of the obstruction. *Harrison et al.* [37] measured the flow field around an arm using hot-wire anemometry, and showed that the mean flow velocity increased as the disks were shrouded and/or as the disk spacing was decreased. *Gor et al.* [38] used LDA to investigate thicker arms, with b = 23% and b = 46%.

[22] The blockage factor for a radially-inserted obstruction was defined as $b = [tL_1]/[H(b+R-R_1)]$, where L_1 is the length of the obstruction, b is the spacing between the disk tip and the shroud, R is the disk radius, and R_1 is the hub radius.

Abrahamson et al. [39] used a dye-injection flow visualization technique to investigate the effects of a relatively large obstruction, with t/S = 0.57, and b = 60%. *Suzuki and Humphrey* [40] used numerical simulations to investigate the effects of relatively large obstructions, with t/S = 0.67, and b = 31% or b = 62%. The simulations were carried out for a single obstruction, as well as for two obstructions simultaneously present in the space between the disks.

Recent disk drives employ a rotary HSA configuration where the sliders are in-line with the suspensions and arms, and the HSA follows a circular arc to position the head on the disk surface. Flow visualizations for the in-line rotary configuration drive were carried out by *Girard et al.* [41], who observed vortex shedding around the E-block arm tip that originated from the flow along the leading and the trailing edges of the arm.

In this study, the effects of E-block arm thickness on the head off-track vibration and the airflow downstream of the arm tip were experimentally investigated in a modeled drive, prepared for this work. Four E-block arms with thicknesses 1.0, 1.2, 1.4, and 1.6 mm were tested. The specific objectives of this study were to form a better understanding of the local flow structure in the region downstream of the HSA, to observe the effects of E-block arm thickness on the flow characteristics in this region and on the head off-track vibration, and to gain insight into how the flow affects head vibration. In addition, the measurements obtained in this investigation constitute an experimental reference for the testing, development, and validation of numerical simulation procedures that aim at predicting the flow in HDDs.

For the head vibration measurements, two HGAs were attached to each E-block arm, and they were inserted between two co-rotating disks, spinning at 10000 rpm, and fixed at a disk spacing of 2.0 mm. Power spectra of the head vibration in the off-track direction were measured using *laser Doppler vibrometry* (*LDV*) at three radial positions: the *inner diameter* (*ID*), the *middle diameter* (*MD*), and the *outer diameter* (*OD*). FEA was used to compute the natural frequencies and mode shapes of the HGAs, the E-block arms, and the HSAs, in order to identify the resonances observed in the experimental measurements. The measured power spectra were used to compute the rms off-track vibrations and their components over selected frequency bands.

Airflow measurements of the obstructed flow between the disks were taken in the region downstream of the E-block arm using *constant-temperature hot-wire anemometry* (*CTA*) at the ID position. The unobstructed flow between the disks in the HSA region was also measured. The mean speed and flow fluctuation power spectra of the airflow downstream of the arm tip, with no HGAs attached, were measured, and were used to compute several quantities including the rms dynamic head fluctuations and their components in the measurement region. These flow measurements were conducted primarily with the goal of shedding some light on the head vibration results. A positive correlation was observed between the dynamic pressure fluctuation levels and the vibration levels.

4.2. Experimental Setup and Measurements

4.2.1. Modeled Hard Disk Drive

The modeled drive shown in Figure 4.1 was prepared for this study. The setup consisted of a fixed plate A, to which the E-block was fastened using a screw; and a movable plate B, on which the spindle, the shroud, and the rest of the enclosure were mounted. The E-block (Figure 4.2(a)) did not have a pivot and a coil, and it did not rotate to seek different radial positions on the disks. Instead, the heads were moved to the desired radial positions by rotating plate B, and consequently the spindle and disks, about an axis that corresponds to the actual pivot of the E-block. The precision of positioning the head at the ID, MD, and OD was achieved through the use of pins that fit in accurately located holes on plate A. This arrangement was employed in order to allow for changing the radial position of the head without changing the relative position between the head and the air-table on which the experimental setup was mounted. This was very convenient for measuring head vibrations using an LDV since it eliminated the need to readjust the LDV head and cable to reestablish beam alignment and focus.

The spindle used in the setup was an actual drive ball-bearing spindle, and it was operated at 10000 rpm (w = 1,047.2 rad/s). A cross-plate (Figure 4.1(b)) was used to support the spindle at the top in order to reduce spindle vibrations. The disk radius R was 42 mm, the disk thickness 1.0 mm, and the disk-to-disk spacing 2.0 mm. The disks were partially shrouded with a shroud cutout angle of 110°. Four different E-block arm thicknesses were tested: 1.0, 1.2, 1.4 and 1.6 mm. These arms will henceforth be referred to as t10, t12, t14 and t16, respectively. The arm tip thickness at the swage area was 0.95

mm for all arms. Figure 4.3 is a schematic of the setup that highlights its most relevant dimensions. *Fujitsu's*[23] '*pico-CAPS*' suspensions for pico-sliders (Figure 4.2(b)) were used in this experiment. The load-beam cross-section of the *pico-CAPS* suspension was rectangular and flangeless.

4.2.2. Laser Doppler Vibrometer Measurements

A *POLYTEC OFV-1102* LDV was used for taking the slider off-track vibration measurements, and its output was averaged in the frequency domain and fed to an *HP3562A* signal analyzer to obtain the averaged vibration power spectra. Two HGAs were attached using adhesive to each arm, and were inserted between the disks. The slider vibrations in the off-track direction were measured at the ID, MD, and OD for each of the arms above, giving a total of twelve measurement sets. For each arm thickness, all measurements were repeated on two identical HSA samples to ensure the consistency and repeatability of the results.

4.2.3. Hot-Wire Anemometer Measurements

A customized CTA hot-wire probe (*TSI model 1276CF-10A*) was used for measuring the flow field. The hot-wire probe (Figure 4.4) carried a single sensor, capable of measuring flow speed without providing any information about flow direction. The body length of the probe was extended so that it could be inserted between the two disks.

[23] *Fujitsu Limited*

The hot-wire probe diameter was 0.9 mm, the sensor diameter 4 μm, and the sensor length 0.2 mm, which was 10% of the disk-to-disk separation. The sensing wire was attached to the probe by two prongs that extended out 4 mm from the end of the probe. The sensor was oriented with its axis parallel to the spin axis, and was centered between the two disks. It was therefore most sensitive to the in-plane flow velocity component at the mid-plane between the disks. The probe body was nearly aligned with the expected mean flow direction to minimize vortex wrapping on the prongs and the associated spurious contributions to the measurements. The output of the CTA was fed to an *HP3563A* signal analyzer. Software was written to perform the data acquisition and preliminary processing. At each measurement point, the CTA output was averaged in the time domain to obtain the mean flow speed, $\overline{u}$. During this part of the measurement the data rate was set low enough (frequency span of 1 kHz, data record length of 800 ms, equivalent to 133 disk revolutions) to ensure that an accurate long-term mean flow speed was obtained. The dc component of the anemometer output was then removed, the data rate was increased (frequency span of 20 kHz, data record length of 40 ms, equivalent to 7 disk revolutions), and the output was averaged in the frequency domain to obtain an averaged power spectrum of the flow fluctuation.

The CTA was calibrated using a precision net flow apparatus prior to the measurements and its calibration curve was determined using least squares regression. A calibration reference measurement of the mean flow speed was taken immediately after calibration in the unobstructed flow between the disks. For each subsequent measurement set a reference measurement was taken at the same location as that of the calibration reference,

so that a correction factor could be computed for the measurement set to account for ambient temperature variations.

The flow measurements taken in this study were carried out at the ID position. For each arm the flow speed was measured in the region downstream of the arm tip, with no HGAs attached. The measurement region, shown to scale with the E-block arm in Figure 4.5, was covered by scanning eight lines perpendicular to the arm trailing edge. These lines were located at distances x = 2, 3, 4, 5, 6, 8, 10, and 12 mm away from the arm tip. The number and density of the measurement points along each line were determined during the measurement for each arm by starting with a coarse point-to-point step of 1.0 mm, and then refining the step size with additional points to capture any steep gradients and local extrema of the mean flow speed and the rms flow fluctuation profiles along the line. Steps as small as 0.05 mm between points were sometimes necessary to capture all the desired details of the profiles. The unobstructed flow between the disks was also measured at the HSA location over an area that contains the measurement region indicated in Figure 4.5. At each measurement point, the flow was allowed to settle for a minimum of 1000 disk revolutions before acquiring the data.

4.3. Data Analysis

The rms off-track vibrations of the heads, Y_{rms}, can be computed from the power spectra $\overline{G_Y(f)}$ of the vibrations, where f denotes frequency, according to[24]

$$Y_{rms} = \sqrt{a \sum_i \overline{G_Y(f)}}, \tag{4.1}$$

where a is a scale factor for the windowing function used in calculating the power spectra. The Hanning window was used for the vibration power spectrum measurements, with $a = 2/3$.

The flow speed, u, in a turbulent flow is commonly analyzed as the sum of the mean and fluctuating components of the speed, $\bar{u}$ and u', respectively

$$u = \bar{u} + u'. \tag{4.2}$$

The rms flow fluctuations, u_{rms}, can be computed from the flow fluctuation power spectra $\overline{G_{u'}(f)}$ according to

$$u_{rms} = \sqrt{a \sum_i \overline{G_{u'}(f_i)}}. \tag{4.3}$$

The Hanning window was used for the flow fluctuation power spectrum measurements, with $a = 2/3$.

[24] Eqs. (4.1) and (4.2) are based on Parseval's theorem, which states that for an aperiodic function $x(t)$ whose Fourier transform is $X(w)$,

$$\int_{-\infty}^{\infty} x^2(t)dt = 2p \int_{-\infty}^{\infty} |X(w)|^2 dw .$$

The rms flow fluctuation is usually expressed as a percentage of the *local* mean flow speed. This percentage is known as the *turbulence intensity*, *TI*, of the flow, and was computed at each measurement as

$$TI = \frac{u_{rms}}{\bar{u}}. \tag{4.4}$$

The drag force, D, on a body can be expressed as

$$D = \int_A C_D q dA, \tag{4.5}$$

where C_D, q, and A denote the sectional drag coefficient, the dynamic pressure, and the projection of the area of the body onto the flow direction, respectively. The dynamic pressure, q, is given by

$$q = \tfrac{1}{2} r u^2, \tag{4.6}$$

where r denotes air density (assumed to be constant).

Substituting Eq. (4.2) into Eq. (4.6), we write q as

$$\begin{aligned} q &= \tfrac{1}{2} r \left(\bar{u} + u'\right)^2 \\ &= \tfrac{1}{2} r \left(\left(\bar{u}\right)^2 + 2\bar{u}u' + \left(u'\right)^2 \right) \end{aligned} \tag{4.7}$$

Similar to velocity, dynamic pressure can be expressed in terms of its mean and fluctuating components, $\bar{q}$ and q', respectively, as

$$q = \bar{q} + q'. \tag{4.8}$$

It follows from Eqs. (4.6) through (4.8) that

$$\bar{q} = \tfrac{1}{2} r \left((\bar{u})^2 + \overline{(u')^2} \right), \tag{4.9}$$

and

$$q' = \tfrac{1}{2} r \left(2\bar{u}u' + (u')^2 - \overline{(u')^2} \right). \tag{4.10}$$

If $\bar{u}$ is much greater than $|u'|$, $\bar{q}$ will be dominated by the first term in the brackets of Eq. (4.9), and q' will be dominated by the first term in the brackets of Eq. (4.10), and they may be approximated as

$$\bar{q} \approx \tfrac{1}{2} r (\bar{u})^2 , \tag{4.11}$$

$$q' \approx r \bar{u} u' . \tag{4.12}$$

The rms dynamic pressure fluctuation q_{rms} can now be written as

$$q_{rms} \approx r \bar{u} u_{rms} . \tag{4.13}$$

Consequently, the mean drag force $\overline{D}$ and the rms drag force fluctuation D_{rms} can be written as

$$\overline{D} \approx \tfrac{1}{2} \int_A C_D r (\bar{u})^2 dA , \tag{4.14}$$

$$D_{rms} \approx \int_A C_D r \bar{u} u_{rms} dA . \tag{4.15}$$

It is clear from Eqs. (4.9) and (4.10) that a higher rms flow fluctuation translates directly into a higher average drag force $\overline{D}$, and a higher rms drag force fluctuation D_{rms}. Eq.

(4.15) also highlights the relevance of the quantity $\bar{u}\, u_{rms}$, since D_{rms} is directly related to $\bar{u}\, u_{rms}$. *Kim et al.* [42] showed, through experimental investigation, a correlation between HGA vibration and $\bar{u}\, u_{rms}$.

The quantities $\bar{h}$ and h_{rms}, defined by,

$$\bar{h} = \frac{1}{2}\left(\left(\bar{u}\right)^2 + \left(u_{rms}\right)^2 \right) \approx \frac{1}{2}\left(\bar{u}\right)^2 , \tag{4.16}$$

$$h_{rms} \approx \bar{u} u_{rms} . \tag{4.17}$$

will henceforth be loosely referred to as the mean dynamic head and the rms dynamic head fluctuation[25], respectively.

Letting w denote the disk angular speed, the disk surface speed V_d is given by

$$V_d = wr . \tag{4.18}$$

A second computer program was prepared to further process the output of the anemometer for each measurement. $\bar{u}$ and u_{rms} and its components over several frequency bands were obtained using the CTA calibration curve. TI, $\bar{h}$, and h_{rms} and its components were also computed. The discrete values of $\hat{u}$, u_{rms}, TI, $\bar{h}$, h_{rms}, and the components of u_{rms} and h_{rms} at the measurement points were then interpolated in the x and y directions to generate continuous distributions of these quantities over the entire measurement region.

[25] Strictly speaking, these quantities should be divided by the gravitational constant $g = 9.81$ m/s^2 to yield the mean and rms dynamic head.

4.4. Finite Element Modeling and Analysis

4.4.1. The Head Gimbal Assemblies

The *pico-CAPS* HGAs were modeled in ANSYS as shown in Figure 4.6(a). The base-plate, load-beam, and slider were modeled using SOLID45 3-D structural solid elements. MASS21 structural mass elements were used to account for the added inertias of the trace, the damping layers on the suspension, the flexible printed circuit terminal, and the gold balls used to ensure electrical connection between the slider and the trace. The position of the printed circuit terminal was not the same for the upper and lower HGAs. ANSYS modal analysis was used to compute the natural frequencies and associated mode shapes of the active modes of the upper and lower HGAs in the 0-20 kHz frequency range. The results are presented in Table 4.1.

4.4.2. The E-Block Arm

The E-block arm was modeled in ANSYS as shown in Figure 4.6(b). The arm was modeled using SOLID45 3-D structural solid elements. The natural frequencies and associated mode shapes of the E-block arm were computed using ANSYS modal analysis for each arm thickness. The results are listed in Table 4.2 for the first five modes. The variation of the natural frequencies of these modes as a function of E-block arm thickness is presented in Figure 4.8(a). Note that the natural frequency of the sway mode was less sensitive to the change in arm thickness than the natural frequencies of the other modes.

4.4.3. The Head Stack Assembly

The HSA in this study consisted of a single E-block arm and two HGAs. It was modeled by combining the component models described above, as illustrated in Figure 4.7. The natural frequencies and associated mode shapes of the HSA were obtained using ANSYS modal analysis for each arm thickness. The HSA modes in the 0-20 kHz range were numerous due to the dynamic coupling between the upper and lower HGAs, and the dynamic coupling between the HGAs and the E-block arm. A complete list of these modes is not provided here. Table 4.3 lists the FEA results for the natural frequencies and mode shapes of the HSA modes that were identified in the experimental measurements. The first mode listed in Table 4.3 was dominated by the E-block arm sway mode, which drove the suspension sway mode. It should be noted that the slope of variation of natural frequency of this mode as a function of E-block arm thickness was roughly the same as that of the variation of the natural frequency of the E-block arm sway mode as a function of arm thickness, as presented in §4.4.2 This is illustrated in Figure 4.8(b).

4.5. Experimental Results and Discussion

4.5.1. Slider Off-Track Vibration Results

The power spectra of the slider off-track vibrations for the four arms are shown in Figure 4.9. All of these spectra exhibited three dominant resonance peaks, the frequencies of which are listed in Table 4.4. The first resonance peak occurred at a frequency of around 8 kHz, and was identified as the E-block arm sway mode coupled with the suspension sway mode (the first mode in Table 4.3). The discrepancy between the frequencies

computed using FEA and those obtained experimentally can be attributed to the incompleteness and simplicity of the FE model. Nonetheless, the congruence of the slope of the variation (as the arm thickness was increased) of the frequency of the measured resonance and that of the variation of the natural frequency of the E-block arm sway/suspension sway mode presented in §4.4.3 is a clear indicator that the observed mode was, in fact, the identified one (Figure 4.8(b)).

The second and third major resonance peaks in the measured spectra occurred at frequencies of around 12 kHz and 14 kHz, respectively. The 12 kHz resonance peak was identified as the second torsion mode of the suspension; the 14 kHz resonance peak was identified as the sway mode of the suspension. Note that the frequencies of these two peaks were relatively insensitive to changes in the E-block arm thickness. The power spectra of the slider off-track vibrations for t10 (Figure 4.9(a)) contained two additional small peaks at 2.65 kHz and 5.7 kHz. The former peak was the first bending mode of the suspension, and the latter was the base-plate first bending mode coupled with the load-beam second bending mode. The amplitude of the 2.65 kHz peak was lower than the amplitudes of the three major modes in the spectra by more than 10 dB, and the amplitude of the 5.7 kHz peak was lower than the amplitudes of the three major modes by more than 20 dB. Consequently, the contributions of these two modes to the slider off-track motions were relatively small.

The rms amplitudes of the slider off-track vibrations were evaluated for each arm thickness over the 0-20 kHz frequency range at the ID, MD, and OD positions. These rms

amplitudes are listed in Tables 4.5, 4.6, and 4.7, and are plotted in Figures 4.10, 4.11, and 4.12. A common feature of all the off-track vibration power spectra was that the amplitudes of the slider off-track vibrations increased as the sliders were moved from the ID to the MD to the OD. This was clearly evident in comparing the scales of Figures 4.10, 4.11, and 4.12. These figures also show that the rms amplitudes of the slider vibrations increased as the arm thickness was increased.

The rms amplitudes over the 0-20 kHz range were broken down into two components: a component over the 0-2 kHz frequency range, and a component over the 2-20 kHz range. The amplitudes of these components are listed in Tables 4.5, 4.6, and 4.7, and are presented in Figures 4.10, 4.11, and 4.12. It is clear that the component amplitudes over both frequency ranges increased as the slider was moved from the ID to the OD. Furthermore, the component amplitudes over the 0-2 kHz range increased as the arm thickness was increased. On the other hand, the trend that the 2-20 kHz component amplitudes followed as the arm thickness was increased was somewhat unexpected. t12 resulted in the highest rms component values and t16 resulted in the lowest rms component values for all radial positions.

The trend that the 0-2 kHz components followed as the arm thickness was increased may be explained by postulating that increasing the arm thickness led to higher levels of turbulence in the flow, hence resulting in greater levels of fluctuation in the aerodynamic forces in the drive. Such fluctuations may have induced higher disk flutter and higher levels of HSA vibrations, which, in turn, generated greater levels of slider vibration.

The trend observed for the 2-20 kHz components was quite interesting, and may be explained as the combination of two effects. The first effect can be explained by noting that if the same external forces are applied to each E-block arm, then the amplitude of the arm sway mode must decrease as the arm thickness is increased, due to the increase in inertia and the increase in stiffness that accompany the increase in arm thickness. This explains the decline in amplitude observed going from t12 to t16. The increase in the rms amplitude components observed in going from t10 to t12 may be explained by the second effect, which is the increase in the flow fluctuation levels and the drag forces as the arm thickness was increased.

The 2-20 kHz rms component amplitudes were further broken down into three subcomponents over the 2-6 kHz, 6-10 kHz, and 10-20 kHz frequency bands in order to assess the contributions resulting primarily from suspension dynamics (the 2-6 kHz and 10-20 kHz bands), and those resulting primarily from E-block arm dynamics (the 6-10 kHz band). These rms component amplitudes are listed in Tables 4.5, 4.6, and 4.7, and are plotted in Figures 4.10, 4.11, and 4.12. An examination of these plots indicates that the component amplitudes increased as the sliders were moved from the ID to the OD, and that this trend was most pronounced for the suspension second torsion and sway modes, which are captured in the 10-20 kHz frequency band.

The first torsion mode of the HGA occurred at around 4 kHz, but there were no peaks at this frequency in the any of the power spectra, which indicates that this mode was not excited to a significant level. This may explain the lack of dependency of the rms

component amplitudes in the 2-6 kHz frequency band on arm thickness. The rms component amplitudes in the 6-10 kHz frequency band were dependent on arm thickness. The main mode excited in this frequency band was the sway mode of the E-block arm, which occurred at around 8 kHz. Going from t10 to t16, the amplitudes of this component were highest for t12 and were lowest for 16 at all radial positions. This is the same trend that was observed in the 2-20 kHz component amplitudes. The variation of the rms component amplitudes in the 10-20 kHz band as a function of arm thickness followed a similar trend to that observed for the rms component amplitudes in the 6-10 kHz band, although the effect was on a smaller scale. The trend followed by the rms amplitudes of the slider off-track vibrations over the 2-20 kHz frequency range was primarily shaped by the 6-10 kHz component.

4.5.2. Airflow Results

4.5.2.1. A Note on the Usefulness of the Airflow Results

Before proceeding with a presentation and discussion of the airflow results, a note should be made about the extent of usefulness of the results. Figure 4.13(a) is a schematic that illustrates key axial dimensions[26] in the space between the two disks. It was noted earlier that the length of the sensing wire was 0.2 mm, which was 10% of the disk-to-disk spacing, 21% of the arm tip thickness, and 13%, 14%, 17%, and 20% of the thicknesses of t16, t14, t12, and t10, respectively. Consequently, the mean and rms output values obtained at each measurement point, and the computed values of $\hat{u}$, u_{rms}, TI, $\bar{h}$, h_{rms}, and the components of u_{rms} and h_{rms}, represent spatial averages of these quantities over the

length of the sensing wire, which is a fraction of the arm thickness. This extends the usefulness of the results because the dynamic head distributions obtained (both mean and rms) provide information about average incremental drag forces $DD = C_D q(DA)$, as opposed to differential drag forces $dD = C_D q(dA)$, that would be generated on a body in the flow. This renders the computed distributions more representative of the drag forces experienced by the arms, and the HGAs, had they been in the flow.

The mean and rms flow speed profiles depicted in Figures 4.13(b) and 4.13(c) are representative of some of the axial profiles expected between the two disks. Profiles $\hat{u}_1(z)$, $\hat{u}_2(z)$, $u'_1(z)$ and $u'_2(z)$ are representative of the mean and rms circumferential velocity axial profiles measured in the obstructed flow between two co-rotating disks by *Usry et al.* [36] at $r/R = 0.71$ and $r/R = 0.78$, 20º downstream of the obstruction. Profiles $\hat{u}_2(z)$ and $u'_2(z)$ are representative of the mean and rms flow speed profiles presented in [36] at $r/R = 0.71$ and $r/R = 0.78$, 90º downstream of the obstruction. Profiles $\hat{u}_2(z)$ and $u'_3(z)$ are representative of those measured for the unobstructed flow between two co-rotating disks by *Schuler et al.* [32] at $r/R = 0.714$ and $r/R = 0.781$, and *Tzeng and Humphrey* [33] at a $r/R = 0.726$, and are likely to be quite similar to the flow in the inner region more than 90º downstream of the E-block arm tip. The latter remark is based on the reportings in [33], [36], [38], [39], [40] that the fluid motion rapidly recovers the mean characteristics of an unobstructed flow as the flow travels further downstream of the obstruction. Profiles $\hat{u}_3(z)$ and $u'_3(z)$ are expected to be representative of the flow passing between the arm tip and the rotating hub, where the flow speed exceeds that of

[26] Axial dimensions are shown to scale. The arm thickness shown is 1.2 mm.

the disk surface on account of the increased flow rate through that region, as the flow approaching the arm is partially blocked and redirected towards the hub. The profiles above exhibit the common feature that they are nearly uniform around the mid-plane over the length of the arm. This is a feature that will be used to justify speculations made below.

At this stage, we will surmise that the flow in the space between the two disks at the measurement region is symmetric with respect to the mid-plane, and possesses mean and rms flow speed profiles similar to those presented in Figures 4.13(b) and 4.13(c). Taking this assumption into consideration, along with the note above on the sensor length, it is reasonable to extend the comparison of the dynamic head distributions in the measurement region to formulate conclusions, merely comparative in nature, about drag forces that would arise due to the complete dynamic pressure fields downstream of the arms.

4.5.2.2. Obstructed Flow Characteristics

Figure 4.14 presents the mean flow speed and rms flow fluctuation profiles along the measurement lines at x = 2, 4, 6, 8, 10, and 12 mm for t10. The plots demonstrate that the mean flow speed profiles exhibited steep gradients, and that the rms fluctuation profiles exhibited peaks that coincided with the steep gradients in the mean speed. These features are characteristic of a classical shear layer observed in free turbulent flows [43], and allude to the existence of a shear layer in the flow. The profiles for t12, t14, and t16 (not shown here) were similar to those of t10. Further discussion of the flow characteristics

and comparison of the flow around the four arms are deferred until after the distributions of $\hat{u}$, u_{rms}, TI, $\bar{h}$, h_{rms}, and the components of u_{rms} and h_{rms} are presented.

In spite of their relevance in detailing out the flow characteristic profiles, the results as presented in Figure 4.14 are difficult to assimilate, and do not readily lend themselves to the task of comparing the flow fields downstream of the four arms. In order to make the results easier to interpret and to provide a more coherent account of the flow characteristic fields in the measurement region, we interpolated the data in the x and y directions (indicated in Figure 4.5) and generated distributions of the flow characteristics over the entire region.

Figure 4.15 depicts two color contour plots of the disk surface speed, generated using two color scales. The plot in Figure 4.15(a) employs the first scale, which is an automatic scale showing the full range of the disk circumferential velocity. The plot in Figure 4.15(b) employs a clipped color scale that is used in all subsequent mean flow speed distribution plots to allow for comparison with the results for the different cases considered. The upper limit in the latter scale was based on the maximum mean flow speed measured with the E-block arms inserted between the disks. These figures are very similar to the schematic of Figure 4.5, with the arm and measurement region rotated slightly to align the x-axis with the horizontal. An outline of the E-block arm tip is shown as solid lines, and an outline of the HGA is shown as dashed lines. The HGA component outlines are labeled in Figure 4.15(a). It should be emphasized that the flow measurements were conducted with no HGAs attached to the E-block arm, and that the

HGA outlines are included in these figures, and in subsequent ones, merely for reference. Due to space limitations, the arm tip outline will be omitted, and only the portion of the HGA outline within the measurement region will be illustrated in the figures that follow.

The mean flow speed distributions for t10, t12, t14, and t16 are presented in Figure 4.16. The distributions were generated using different scales, precluding quantitative comparison across the plots, and have been included for a qualitative comparison of the expected main flow direction, especially in the area that would be occupied by the HGAs. The plots for all arms demonstrate a high flow speed region along the upper edge of the HGA outline, with a steep gradient region immediately below it over which the mean speed drops to an appreciably lower level. Although no direct evidence of the flow direction has been obtained in this investigation, speculations about the flow direction are justified, based on flow visualization results presented by *Girard et al.* [41] for a similar geometric setup, and on the characteristics of the shear layer alluded to earlier. The approximate main flow direction can be inferred from the plots by following the locus of the maximum mean flow speed across the measurement lines, which is indicated by the dark red area. This exercise suggests the flow crossed the HGA outline at a greater angle as the arm thickness was decreased, which implies a greater projection of the area of the HGA (had it been in the flow) onto the flow direction. Such an observation can be explained by noting that as the arm thickness was increased, more of the flow upstream of the arm was blocked by the arm and redirected with greater speed towards the hub. In fact, the plot for t16 suggests that most of the main flow overshot the HGA. The relevance of this remark stems from the direct proportionality of the mean and rms drag

forces to the projected area of the body onto the flow direction, expressed in Eqs. (4.14) and (4.15). It should be noted that some areas of the contours appear jagged due to the interpolation of sparse data, since the measurement grid was coarser in the horizontal direction than the vertical direction.

The mean flow speed fields in the measurement region for t10, t12, t14, and t16 were regenerated using *the same scale* for all arms, and are presented in Figure 4.17. For all arms there was a high mean flow speed zone along the upper edge of the HGA outline, and a low mean flow speed zone below that, with a steep speed gradient in between. This distribution is attributed to the presence of the arm, as it partially blocked the upstream flow and redirected it towards the gap between the hub and the arm tip. A comparison of Figures 4.15 and 4.17 reveals that the flow speed was much lower than the disk surface speed over most of the measurement region, and that, for t14 and t16, the local speed of air exceeded that of the disk surface around the upper edge of the tip of the HGA outline, as the air accelerated through the gap between the arm tip and the rotating hub. The blockage factors[27] associated with the four E-block arms at the ID position are listed in Table 4.8. A comparison of the plots of Figure 4.17 indicates that increasing the arm thickness resulted in elevating the mean flow speed in the entire measurement region. The HGA outline exhibited higher flow speeds for t12 than it did for t10, primarily due to the increase in the overall mean flow speed. The HGA outline exhibited slightly higher flow speeds for t14 than it did for t12, especially near the top edge of the slider. For t16, although the measurement region experienced the higher flow speed level, most of the high-speed flow was above the HGA outline, and the outline seems to be subject to a

similar level of flow speed to that of t10, if not lower. The significance of this trend is explained by the following two points: the mean drag force on the HGA is proportional to the square of the approaching flow speed, as expressed in Eq. (4.14); and the rms drag force fluctuation acting on the HGA is directly proportional to the approaching flow speed, as shown in Eq. (4.15).

The mean dynamic head color contour plots are shown in Figure 4.18. These distributions follow the same trend as that observed for the mean flow speed distributions: a result which is expected due to the approximation given in Eq. (4.11).

Figure 4.19 presents the rms flow fluctuation distributions for t10, t12, t14, and t16. The plots immediately reflect the increase in the level of flow fluctuation as the arm thickness was increased. The high-fluctuation region in these plots begins near the upper edge of the HGA outline, and coincides with the steep gradient in the mean flow speed distributions. As noted earlier, this feature is characteristic of a classical shear layer observed in free turbulent flows, and supports our assertion earlier about the flow direction, since in a classical shear layer the high-fluctuation region closely follows the main flow on the higher-speed side of the layer. The high-fluctuation area of t16 did not extend to the tip of the HGA as it did for the other three arms. A small additional area with relatively high fluctuation appeared near the upper edge of the tip of the HGA outline (around $x = 12$, $y = 3$) in the t16 distribution. It should be noted that the high-fluctuation regions appear to be scattered in these plots due to the interpolation of sparse

[27] These blockage factors were based on the projected area of the arm leading edge onto a radial plane.

data, since the measurement grid was coarser in the horizontal direction than the vertical direction.

The turbulence intensity and the rms dynamic head fluctuation distributions for the four arms are shown in Figures 4.20 and 4.21, respectively. The plots of Figure 4.21 clearly reveal an increase in the rms dynamic head fluctuation levels, both in the measurement region and within the HGA outline, as the arm thickness was increased from t10 to t12 to t14. The overall dynamic head fluctuation in most of the measurement region for t16 appears to have been higher than that for t14, the exception being the area near the HGA tip. It is difficult to assess whether the HGA outline contained a higher overall level of dynamic head fluctuation in the t14 or the t16 cases. The high-fluctuation region in the t14 distribution extended to the tip of the HGA, whereas the region in the t16 distribution attained the highest level of fluctuation, and spread out more in the *y* direction.

In order to obtain more diagnostic information about the airflow excitation and its relation to the head off-track vibrations, we decomposed the rms flow fluctuations and the rms dynamic head fluctuations into components over the frequency bands considered in §4.5.1. Namely, the rms fluctuations were decomposed into components over the 0-2 kHz and the 2-20 kHz frequency bands. The contributions of the 0-2 kHz components were noticeably greater than those of the 2-20 kHz components. The 2-20 kHz components were further divided into subcomponents over the 2-6 kHz, 6-10 kHz, and 10-20 kHz frequency bands. The contributions of these components were highest for the

2-6 kHz components, followed by the 6-10 kHz components, followed by the 10-20 kHz components.

Figures 4.22 and 4.23 depict the distributions of the 0-2 kHz components of the rms flow fluctuation and the rms dynamic head fluctuation, respectively. The figures reveal that as the arm thickness was increased both of these components increased in the measurement region, and within the HGA outline as well, with the exception of the area around the HGA tip outline for t16. As was the case with the rms fluctuation, the high-fluctuation area of t16 of both components did not extend to the tip of the HGA as it did for t10, t12, and t14. The high-fluctuation areas in the t16 distributions spread to cover a wider portion (in the y direction) of the HGA around the base-plate than they do in the t14 distributions, and a small additional area with relatively high fluctuation appeared near the upper edge of the tip of the HGA outline (around $x = 12$, $y = 3$) in the t16 distribution. Thus, it is difficult to judge whether the HGA outline contains a higher overall level of fluctuation in the 0-2 kHz band for the t14 or the t16 cases.

The 2-20 kHz components of the rms flow fluctuation and the rms dynamic head fluctuation are presented in Figures 4.24 and 4.25, respectively. An examination of these plots indicates that the levels of these components, especially within the HGA outline, increased as the arm thickness was increased from 1.0 mm to 1.2 mm, then they decreased as the thickness was increased to 1.4 mm, and then decreased further as the thickness was increased to 1.6 mm.

Figures 4.26 and 4.27 portray the 2-6 kHz components of the rms flow fluctuation and the rms dynamic head fluctuation, respectively. These components appear to follow the same trend as that observed for the 2-20 kHz components. The 6-10 kHz components of the rms flow fluctuation and the rms dynamic head fluctuation are presented in Figures 4.28 and 4.29, respectively. The overall levels of the flow fluctuation components appear to be highest for t12 and t14, followed by t10, and finally t16. The levels of this component of the dynamic head fluctuation within the HGA outline seem to be highest for t12, followed by 14 and t10, and finally t16. The 10-20 kHz components of the rms flow fluctuation and the rms dynamic head fluctuation are presented in Figures 4.30 and 4.31, respectively. It is difficult to compare the overall levels of the flow fluctuation components of Figure 4.30. However, the levels of 10-20 kHz components of the rms dynamic head fluctuation clearly follow the same trend as that observed in the 2-20 kHz frequency band: t12 appears to have the highest levels of fluctuation, followed by t14 and t10, and finally t16.

Figure 4.32 depicts the power spectra of the CTA output at the measurement points along the line at $x = 2$ mm for the four arms. The plots are three-dimensional, with frequency on the horizontal axis, dB amplitude on the vertical axis, and y-position (along the $x = 2$ mm line) on the third axis. Each curve within a plot represents the power spectrum at a certain y-position along the measurement line, and the color contour has also been included to emphasize the magnitude of the spectra. The plots for t10, t12, and t14 have been given the same view, with the origin on the right hand side and frequency increasing from right to left, whereas the plot for t16 has the origin on the left hand side, because these views

best demonstrate the plot features described below. All power spectra exhibited a peak at 167 Hz, which coincides with the disk rotation speed, and is attributed to disk run-out. The power spectra illustrate the dominance of the low frequency components; the high frequency energy was more pronounced only in the range of y = -6 to 0.5 mm. The plots also reveal the presence of clearly identifiable peaks, which we identify with vortex shedding from the arm, in the power spectra. Two coherent vortex shedding peaks were observed in the power spectra of each arm along the x = 2 mm line. The frequencies of these peaks, f_v, are listed in Table 4.9. These are the frequencies in the separated region and the shear layer, and were generated by the flow separation from the arm.

For bodies with simple geometries, the frequencies of the vortex shedding peaks can be correlated using the *Strouhal number St* defined by

$$St = \frac{f_v l}{U}, \tag{4.19}$$

where f_v, l, and U are the vortex shedding frequency [cycles/sec], the characteristic length of the body, and the characteristic speed of the approaching flow, respectively.

The Reynolds number *Re* is defined by

$$Re = \frac{Ul}{\acute{\imath}_k}, \tag{4.20}$$

where n_k is the kinematic viscosity of the fluid. The values of the *Re* for the four arms and the arm tip were computed using U = 20 m/s, n_k = 1.512×10^{-5} m^2/s, and l = arm thickness, and are listed in Table 4.9.

It is known from experimental results that the St remains essentially constant at $St \cong 0.21$ for the free flow over a circular cylinder with Re in the range $400 < Re < 10000$ [43]. Since the Re listed in Table 4.9 is within this range for all arm thicknesses, $St = 0.21$ can be used to estimate the vortex shedding frequencies $f_{cyl,t}$ for the free flow over a circular cylinder with a characteristic diameter l set equal to 0.95, 1.0, 1.2, 1.4, and 1.6 mm and a characteristic flow speed of $U = 20$ m/s. The computed values of $f_{cyl,t}$ are listed in Table 4.9. Even though these estimates cannot be used to predict the vortex shedding frequencies for the E-block arms, a comparison of the f_v and $f_{cyl,t}$ columns in this table indicates that they provide a reasonable approximation of the frequencies observed.

Figures 4.33 and 4.34 present the power spectra of the CTA output at measurement points along the lines at $x = 4$ mm and $x = 6$ mm, respectively. These figures show that the peaks were still identifiable on the 4 mm line, but their amplitudes had diminished considerably. Along the 6 mm line, the their amplitudes had diminished to the point where they could barely be identified in the spectra.

4.5.2.3. Unobstructed Flow Characteristics

The unobstructed flow between the disks was measured at the HSA location, over regions[28] A, B, and C (Figure 4.35(a)). The arm and HGA outlines are shown as dashed lines, and the circumferential lines and gridlines over regions A and C are also shown in the figure for reference.

The distributions of $\hat{u}$, u_{rms}, TI, $\overline{h}$, h_{rms}, and the components of u_{rms} and h_{rms} in regions A, B, and C are shown in Figures 4.35(b) through 4.35(p). Figure 4.35(b) shows that the mean flow speed was approximately 75-80% of the disk surface speed, and it suggests that the flow did not move along the circumferential lines in this region. The high fluctuations in region C over all frequency bands can be attributed to the turbulence generated at the shroud cutout. A comparison of the plots of the obstructed flow characteristics (presented in §4.5.2.2) and the unobstructed flow characteristics in the measurement region (region A in Figure 4.35) illustrates that there was a reduction in the mean flow speed and a substantial increase in the rms flow and dynamic head fluctuations over all frequency bands due to the presence of the arm. Figure 4.36 shows the power spectra of the flow fluctuation along the line at x = 2 mm for the unobstructed flow. It should be noted that no vortex shedding peaks could be detected in these spectra.

4.5.3. The Relationship Between Flow Fluctuation and Off-Track Vibration

Figure 4.10 showed that the rms slider off-track vibration amplitudes at the ID increased as the arm thickness was increased, with only a slight difference between t12 and t14. This trend agrees with the trend followed by the rms flow fluctuation levels and the rms dynamic head fluctuation levels in the measurement region, depicted in Figures 4.19 and 4.21, especially within the HGA outline. There is a positive correlation between the trends followed by the slider off-track vibrations and the flow and dynamic head fluctuations.

---

[28] Region A was the measurement region in this study. The measurement region was extended in the study presented in Chapter 5 to include region C as well.

Figure 4.10 demonstrated that the 0-2 kHz component amplitudes of the rms vibration increased as the arm thickness was increased. This trend correlates with the trends followed by the 0-2 kHz components of the rms flow fluctuation and the rms dynamic head fluctuation within the HGA outline, illustrated in Figures 4.22 and 4.23.

Figures 4.10, 4.24, and 4.25 indicate a positive correlation between the trends followed by the 2-20 kHz rms components of the off-track vibrations, the flow fluctuation, and the dynamic pressure fluctuation. The trend and the correlation observed in this component carries over to the 6-10 kHz and the 10-20 kHz rms components of the off-track vibration, the flow and dynamic head fluctuations.

It was shown in Eq. (4.15) that the rms drag force fluctuations are directly related to the rms dynamic head fluctuations. These drag force fluctuations result in dynamic forces acting on the HSA and the disks, and consequently in structural vibrations and slider off-track vibrations. The positive correlations observed between slider vibration components and dynamic pressure fluctuation components are an expression of this causality.

4.6. Conclusion

The effects of E-block arm thickness on the slider off-track vibrations and the airflow downstream of the arm tip between two disks in a modeled hard disk drive were investigated experimentally. Four arms with thicknesses 1.0, 1.2, 1.4 and 1.6 mm were tested. Slider off-track vibrations were measured at the ID, the MD, and the OD positions. For all E-block arms, the vibrations increased as the sliders were moved from

ID to OD. The primary contributors to the off-track vibrations were identified as the E-block arm sway mode, the suspension second torsion mode, and the suspension sway mode. The rms vibration amplitudes were decomposed into components over two frequency bands, 0-2 kHz and 2-20 kHz, in order to assess the contributions of the structural resonances to the total vibration. The 2-20 kHz component was further divided into subcomponents over three frequency bands in order to isolate the contributions of the E-block arm dynamics and the suspension dynamics to the rms off-track vibration.

The measured off-track vibrations were dependent on the E-block arm thickness. The rms vibration amplitudes, for all radial positions, increased as the arm thickness was increased. This trend was also observed in the 0-2 kHz component amplitudes. This trend, however, was not observed in the 2-20 kHz component amplitudes. The 1.2 mm arm resulted in the highest values of the 2-20 kHz components, and the 1.6 mm arm resulted in the lowest values. This trend was also observed in the two subcomponents of the 2-20 kHz band that contained the arm sway mode and the suspension second torsion and sway modes.

The mean and rms flow speed were measured using a single-sensor hot-wire anemometer at the mid-plane between the two disks, and were used to compute the turbulence intensity, the mean and rms dynamic head, and the components of the rms flow and dynamic head fluctuations over the same frequency bands considered in their rms off-track vibration breakdown. The rms dynamic head fluctuation decomposition revealed a positive correlation between the rms dynamic head fluctuation components and the

corresponding rms off-track vibration components. Specifically, a positive correlation was observed between these components over the 0-20 kHz, 0-2 kHz, 2-20 kHz, 6-10 kHz, and 10-20 kHz frequency bands. The flow fluctuation power spectra unveiled the presence of clearly identifiable peaks, which we connect with vortex shedding from the arms, for all four arms.

Natural Frequency [Hz]		Mode Shape	
Upper	**Lower**		
2200	2200	Load-beam first bending	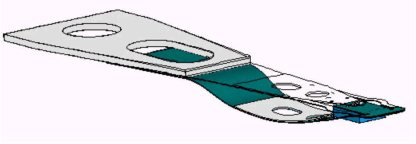
4080	4080	Load-beam first torsion	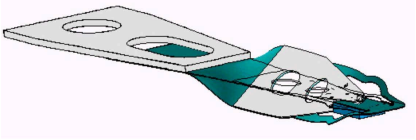
5470	5520	Base-plate first bending in-phase with load-beam second bending	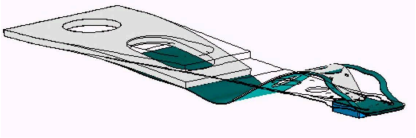
6940	7050	Base-plate first bending out-of-phase with load-beam second bending	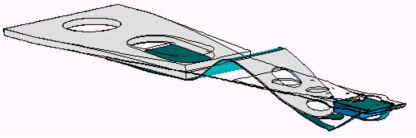
12960	12960	Load-beam second torsion	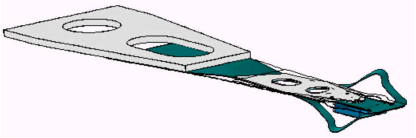
13100	13080	Load-beam third bending	
14420	14420	Load-beam sway	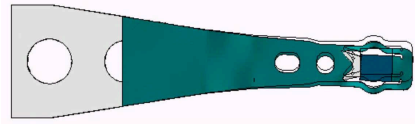
18550	18540	Load-beam fourth bending	
19070	17350	Load-beam third torsion in-phase with base-plate first torsion	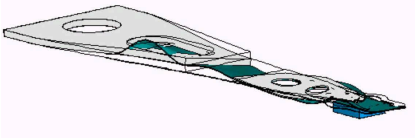
20130	19790	Load-beam third torsion out-of-phase with base-plate first torsion	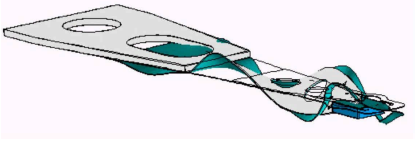

Table 4.1: FEA modal analysis results for HGA.

Natural Frequency [Hz]				Mode Shape	
$t = 1.0$	$t = 1.2$	$t = 1.4$	$t = 1.6$		
2000	2500	3000	3500	First bending	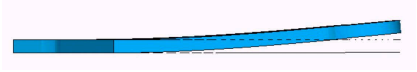
9160	11020	12810	14520	Second bending	
11230	13340	15400	17420	First torsion	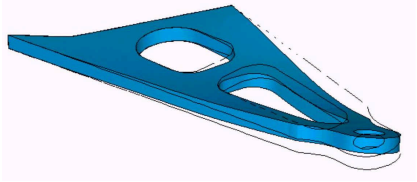
13860	14290	14610	14870	Sway	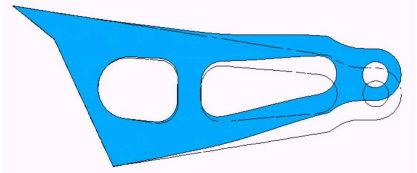
22970	27240	31270	35030	Third bending	

Table 4.2: FEA modal analysis results for E-block arms.

Mode Shape	Natural Frequencies [Hz]			
	***t* = 1.0**	***t* = 1.2**	***t* = 1.4**	***t* = 1.6**
E-block sway coupled with suspension sway	9200	9720	10150	10500
E-block first torsion coupled with suspension third bending	9120	10450	11510	13420
Suspension second torsion (upper and lower suspensions in-phase)	12960	12970	12940	12920
Suspension second torsion (upper and lower suspensions out-of-phase)	12960	13010	13040	13070
Suspension sway (upper and lower suspensions in-phase)	14030	14180	14300	14350
Suspension sway (upper and lower suspensions out-of-phase)	14460	14490	14600	14400

Table 4.3: FEA modal analysis results for HSA.
(modes identified in experimental measurements)

Mode Shape	Resonance Frequencies [Hz]			
	***t* = 1.0**	***t* = 1.2**	***t* = 1.4**	***t* = 1.6**
E-block sway coupled with suspension sway	7450	7950	8130	8330
E-block third torsion coupled with suspension second bending	9120	10450	11510	13420
Suspension second torsion	12700	12200	12230	12530
Suspension sway	13750	14100	14130	14050

Table 4.4: Estimates of resonant peak frequencies observed in vibration spectra.

***t* [mm]**	**0-20 kHz**	**0-2 kHz**	**2-20 kHz**	**2-6 kHz**	**6-10 kHz**	**10-20 kHz**
1.0	4.15	2.43	3.37	1.22	2.40	2.01
1.2	5.21	3.28	4.05	0.82	2.99	2.61
1.4	5.29	3.79	3.68	0.92	2.44	2.61
1.6	5.42	4.53	2.98	0.84	1.72	2.29

Table 4.5: RMS amplitudes and components [nm] of off-track vibration at the ID.

t [mm]	0-20 kHz	0-2 kHz	2-20 kHz	2-6 kHz	6-10 kHz	10-20 kHz
1.0	5.95	2.92	5.18	1.43	2.35	4.39
1.2	6.82	3.70	5.73	1.05	3.66	4.28
1.4	7.48	5.39	5.19	1.11	2.63	4.33
1.6	9.34	8.24	4.39	1.04	1.72	3.90

Table 4.6: RMS amplitudes and components [nm] of off-track vibration at the MD.

t [mm]	0-20 kHz	0-2 kHz	2-20 kHz	2-6 kHz	6-10 kHz	10-20 kHz
1.0	7.66	3.63	6.75	1.54	2.94	5.88
1.2	9.47	5.30	7.85	1.23	4.74	6.14
1.4	10.12	7.32	6.99	1.37	3.34	5.99
1.6	10.51	9.00	5.42	1.17	2.39	4.73

Table 4.7: RMS amplitudes and components [nm] of off-track vibration at the OD.

Arm	*t* [mm]	Blockage Factor at ID
t10	1.0	27%
t12	1.2	31%
t14	1.4	36%
t16	1.6	40%

Table 4.8: Blockage factors for the E-block arms at the ID position.

Arm	*Re*	f_v [kHz]	$f_{cyl,t}$ [kHz]
arm tip	1260	-	4.4
t10	1320	3.8, 4.5	4.2
t12	1590	2.6, 3.5	3.5
t14	1850	3.0, 3.8	3.0
t16	2120	2.8, 3.8	2.6

Table 4.9: Reynolds numbers and vortex shedding frequencies.

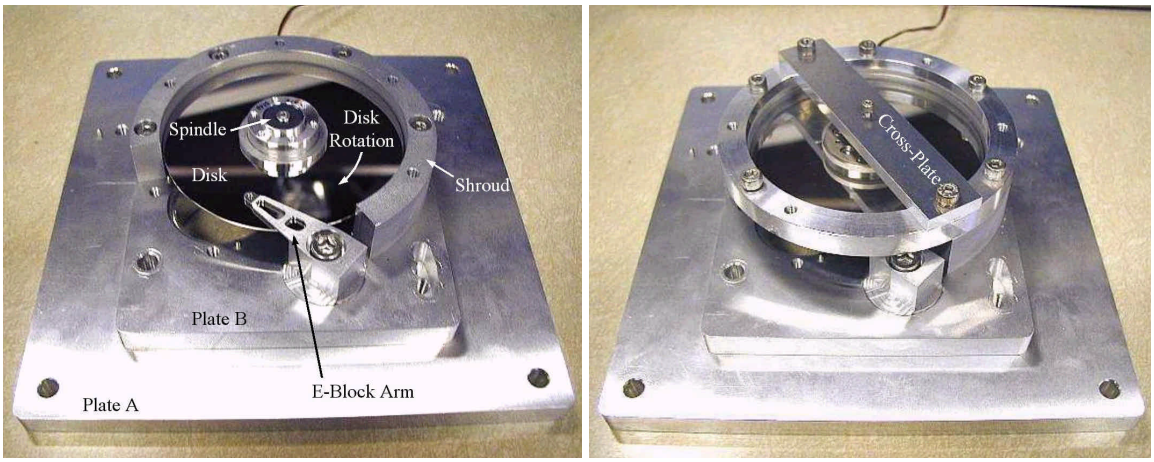

(a) without top disk and cover (b) with top disk and cover

Figure 4.1: Modeled hard disk drive.

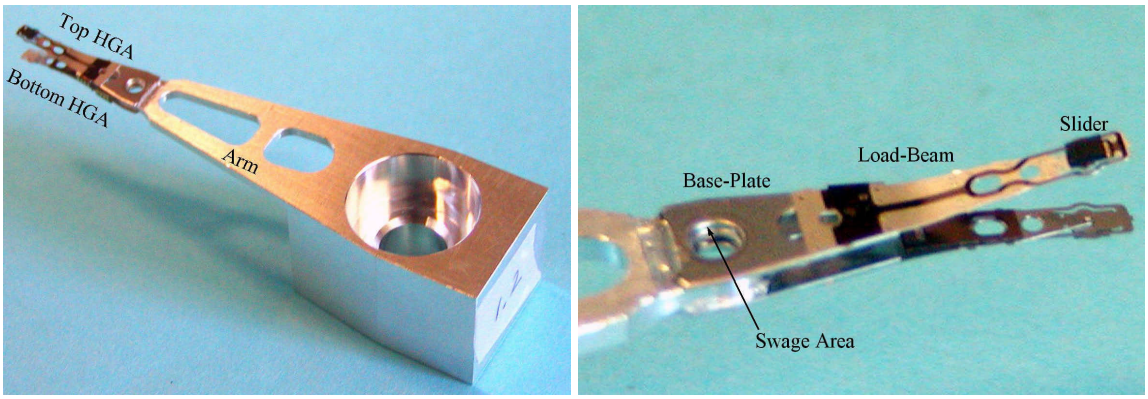

(a) Pico-CAPS HGA (b) HSA

Figure 4.2: Photographs of HSA and HGA.

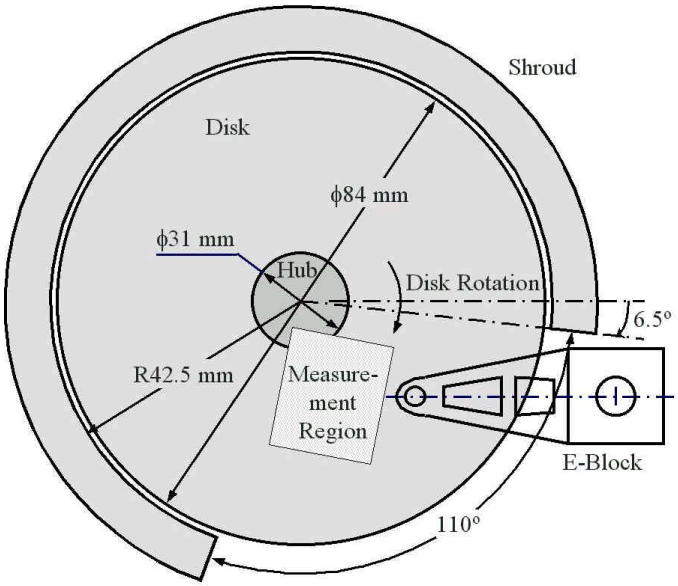

Figure 4.3: Schematic of the setup.

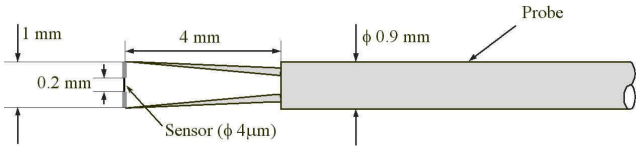

Figure 4.4: Schematic of the hot-wire probe.

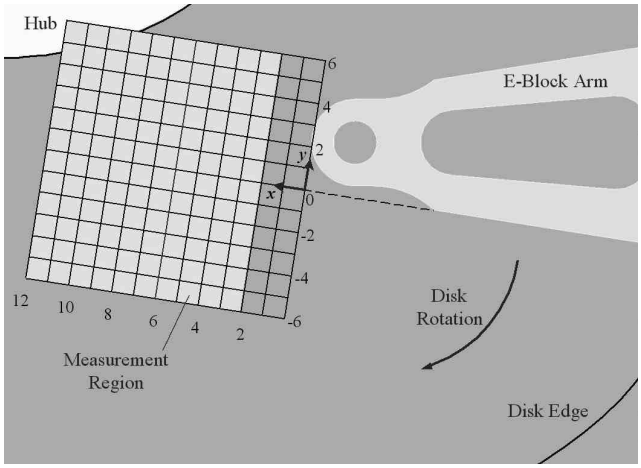

Figure 4.5: Airflow measurement region.

(a) FE model of the HGA (b) FE model of the arm

Figure 4.6: FE models of the HGA and the E-block arm.

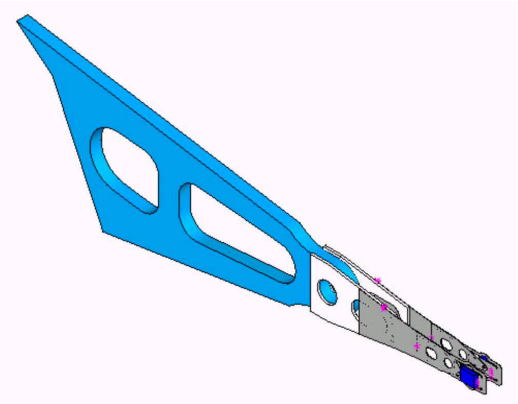

Figure 4.7: FE model of the HSA.

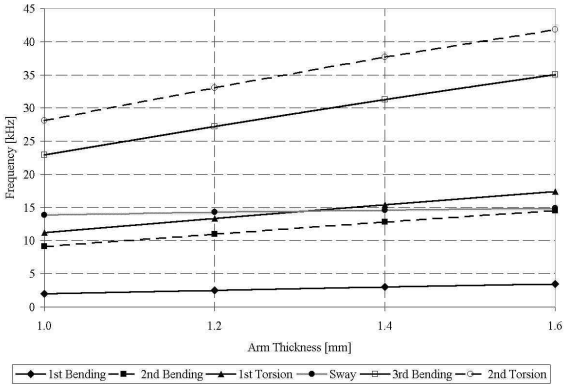

(a) Natural frequencies of arm modes

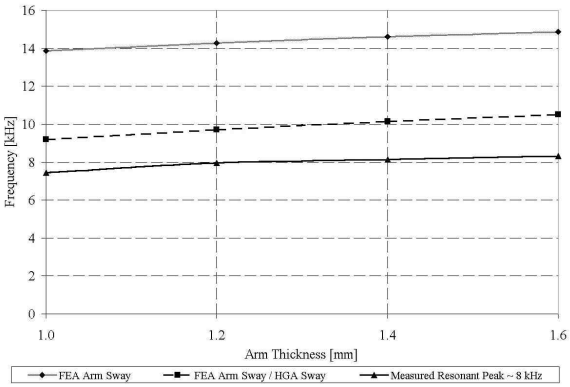

(b) Arm sway mode, FEA and measured.

Figure 4.8: Natural frequencies and measured resonant frequencies vs. arm thickness.

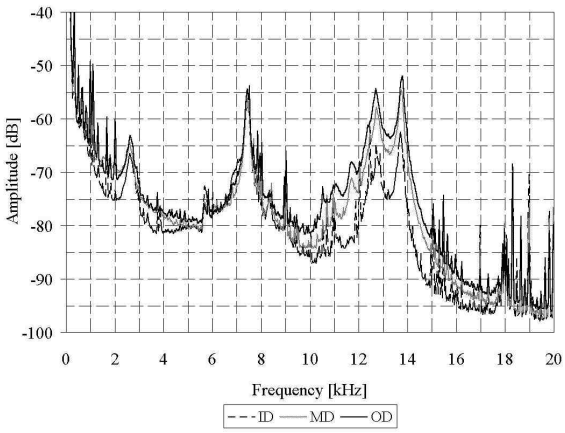

(a) t10

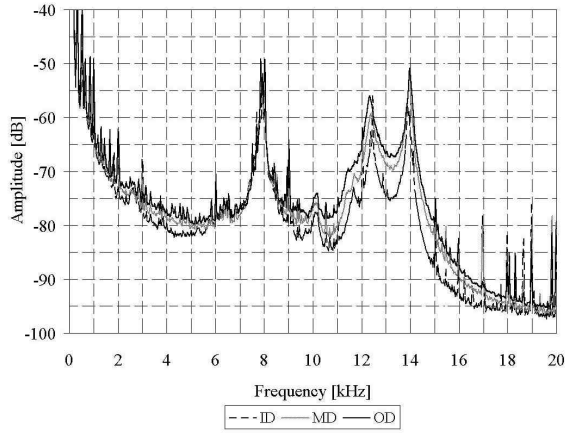

(b) t12

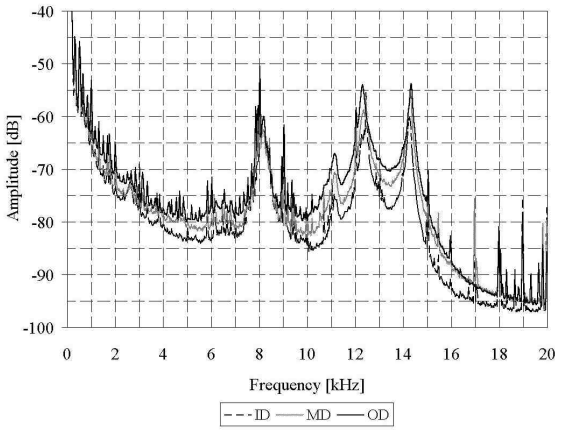

(c) t14

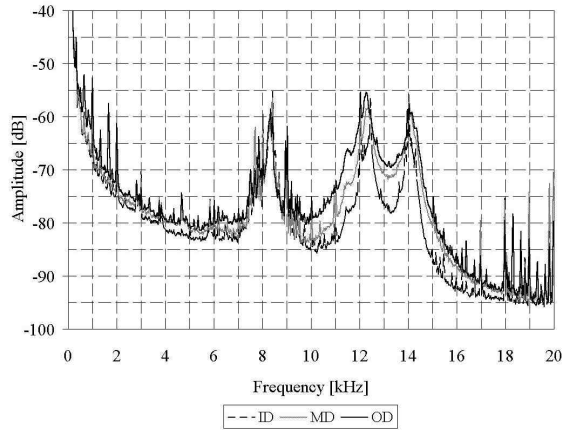

(d) t16

Figure 4.9: Power spectra of slider off-track vibrations.

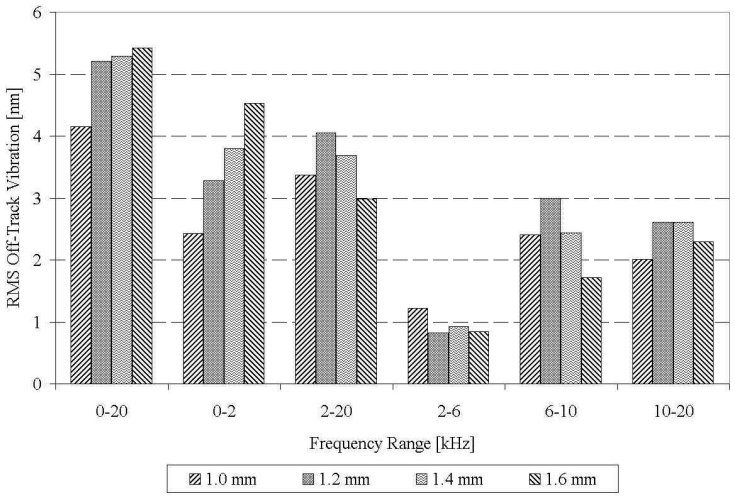

Figure 4.10: RMS amplitudes and components of off-track vibration at the ID.

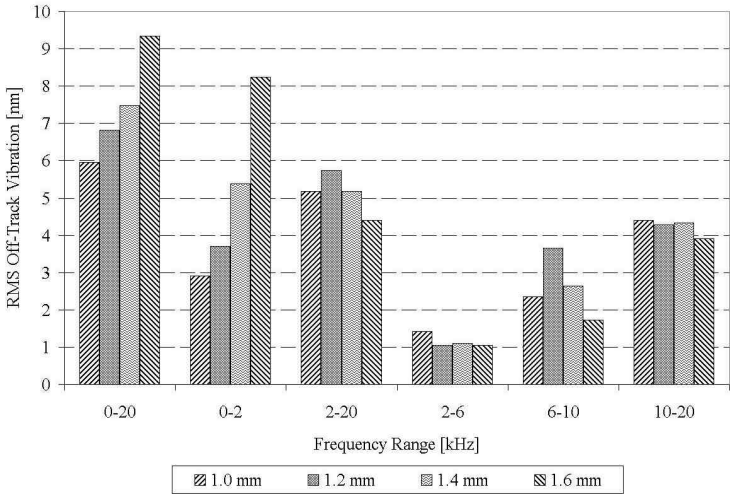

Figure 4.11: RMS amplitudes and components of off-track vibration at the MD.

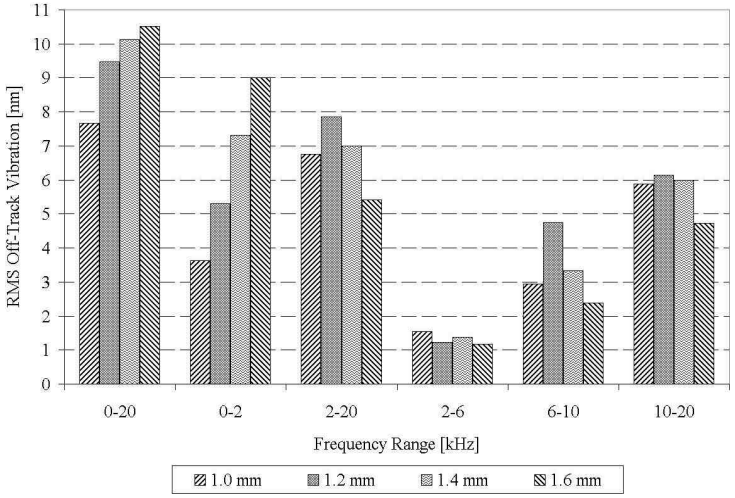

Figure 4.12: RMS amplitudes and components of off-track vibration at the OD.

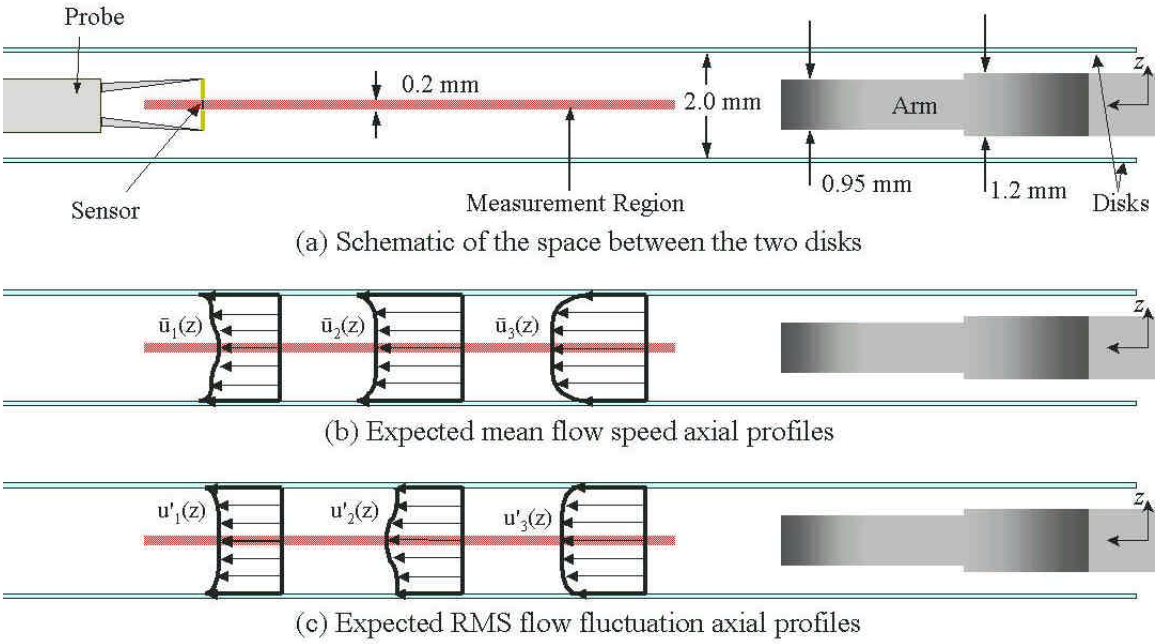

Figure 4.13: Schematic of space between the disks; expected $\bar{u}$ and u_{rms} profiles.

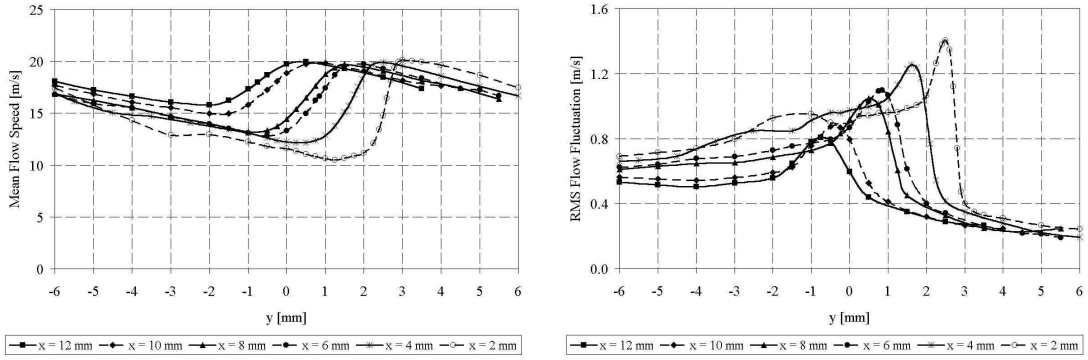

(a) $\bar{u}$ profiles (b) u_{rms} profiles

Figure 4.14: $\bar{u}$ and u_{rms} profiles along the measurement lines; t10.

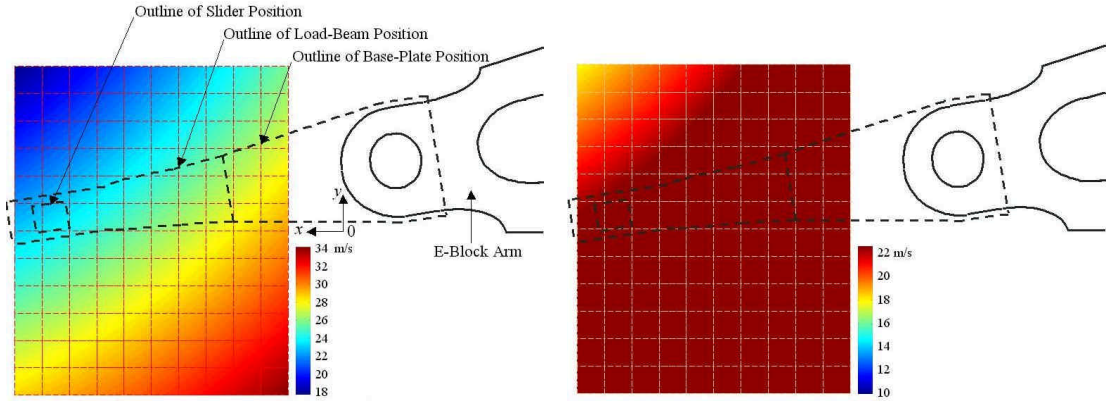

(a) Disk surface speed, full scale (b) Disk surface speed, clipped scale

Figure 4.15: Disk surface speed.

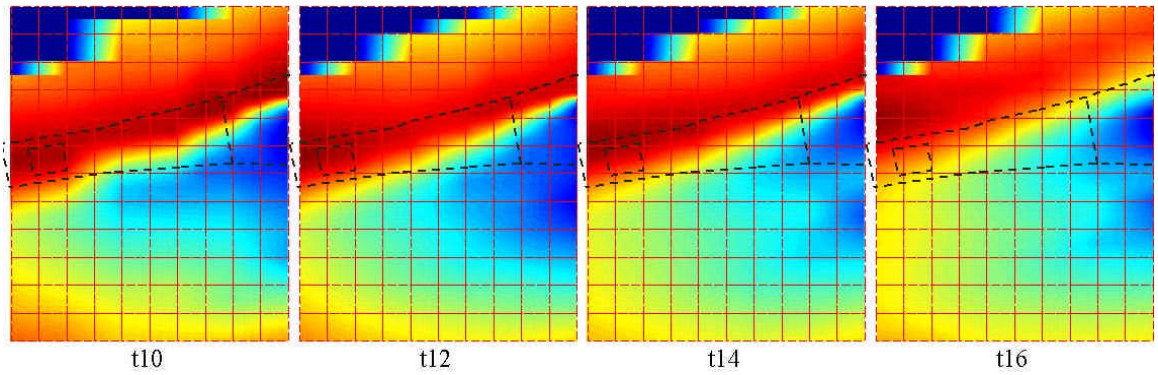

Figure 4.16: Mean flow speed distributions; different scales.

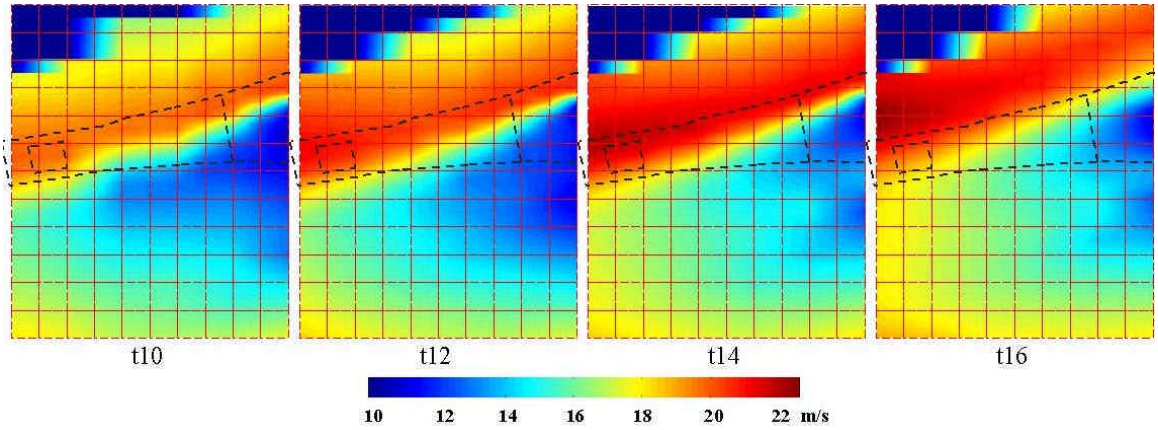

Figure 4.17: Mean flow speed distributions; same scale.

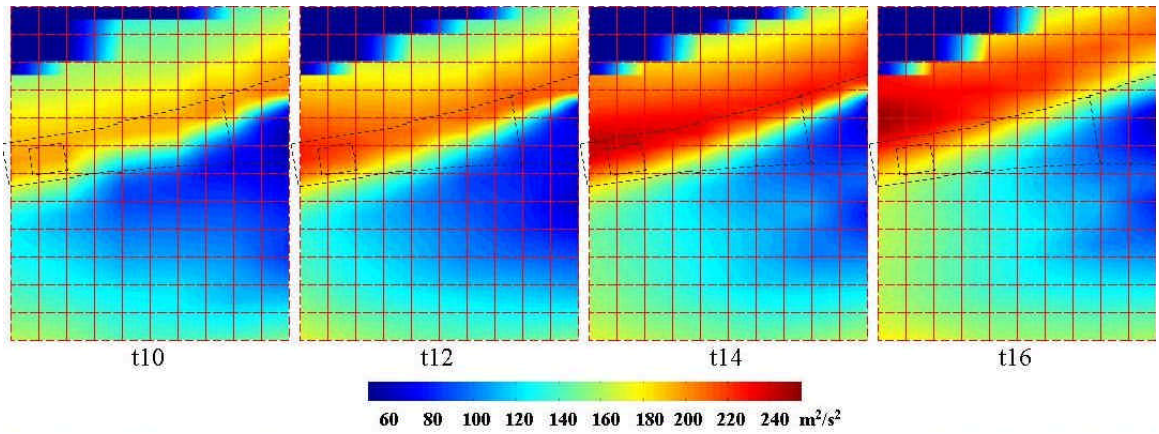

Figure 4.18: Mean dynamic head distributions.

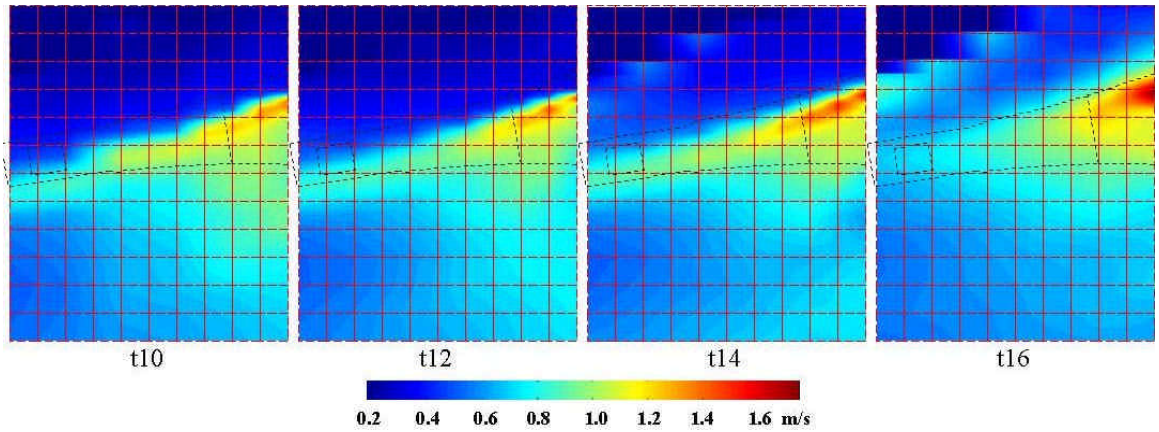

Figure 4.19: RMS flow fluctuation distributions.

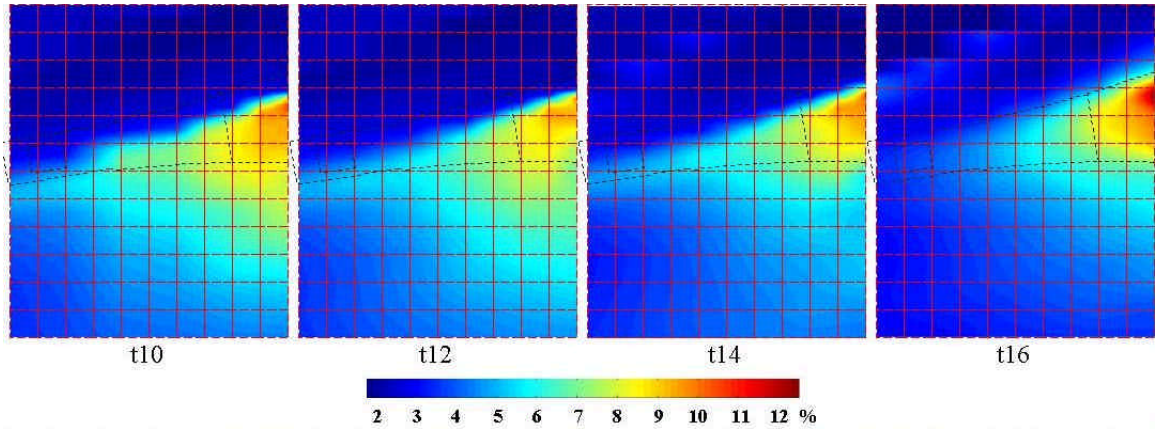

Figure 4.20: Turbulence intensity distributions.

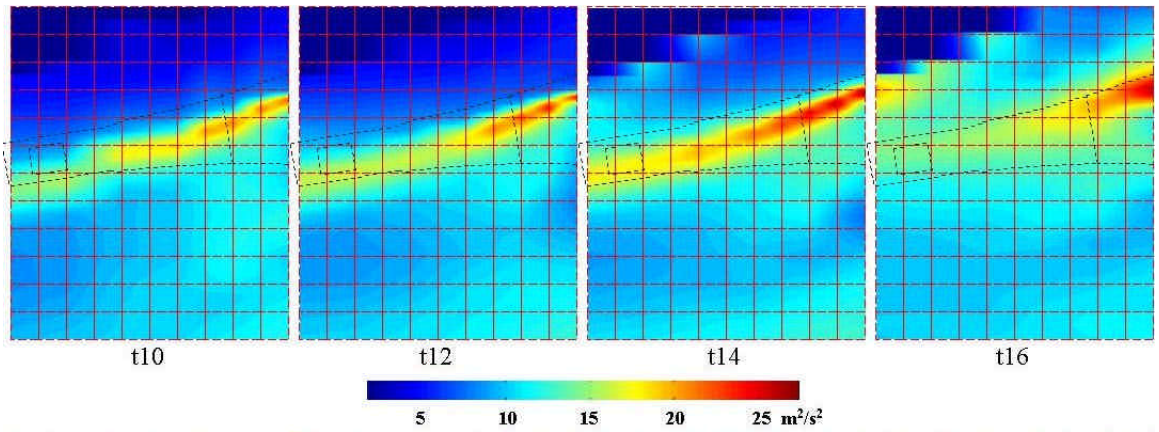

Figure 4.21: RMS dynamic head fluctuation distributions.

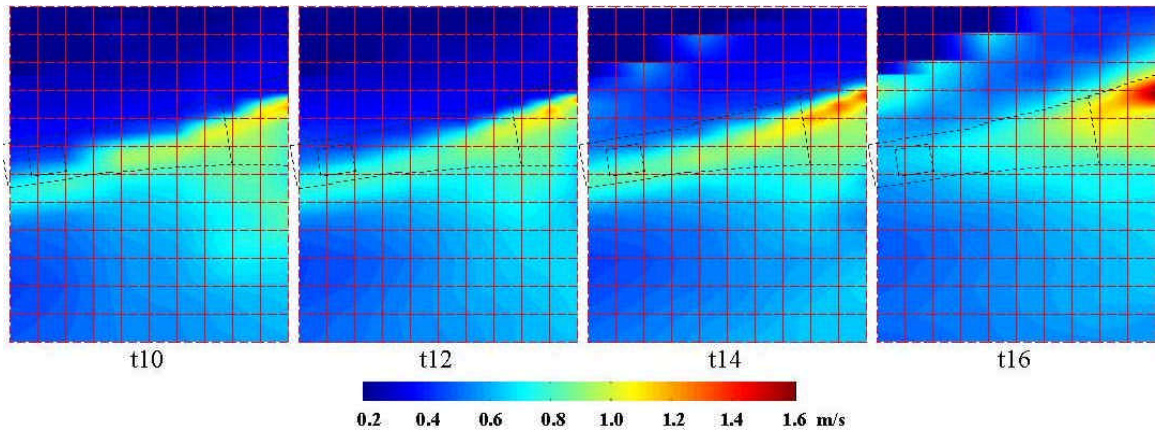

Figure 4.22: Distributions of 0-2 kHz component of rms flow fluctuation.

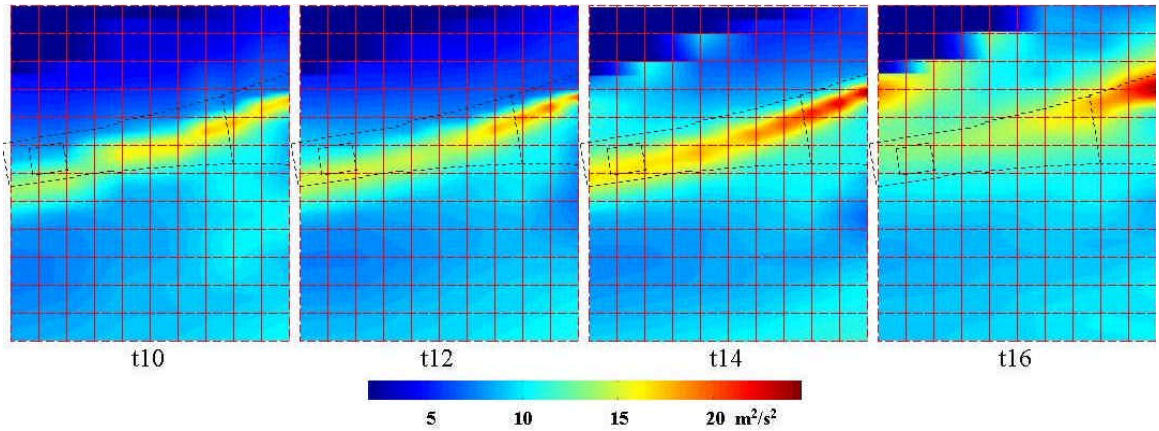

Figure 4.23: Distributions of 0-2 kHz component of rms dynamic head fluctuation.

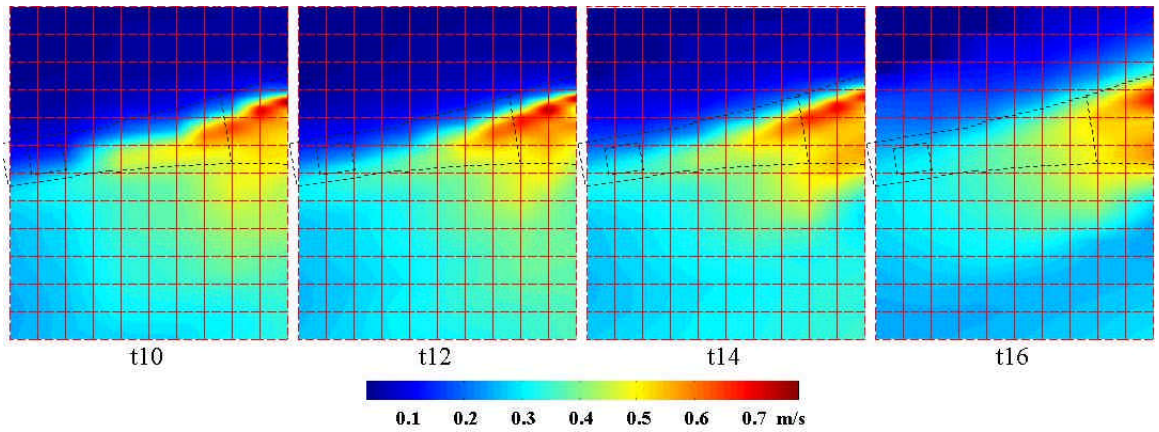

Figure 4.24: Distributions of 2-20 kHz component of rms flow fluctuation.

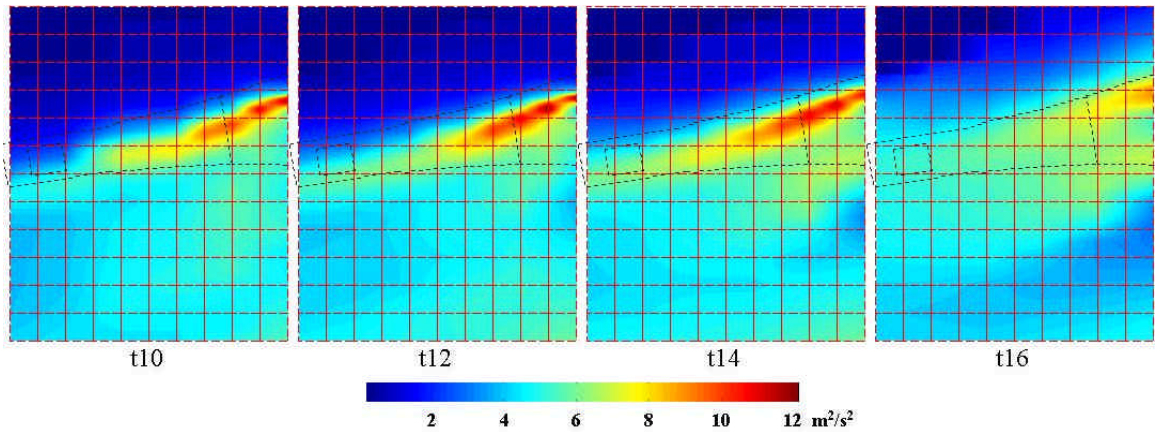

Figure 4.25: Distributions of 2-20 kHz component of rms dynamic head fluctuation.

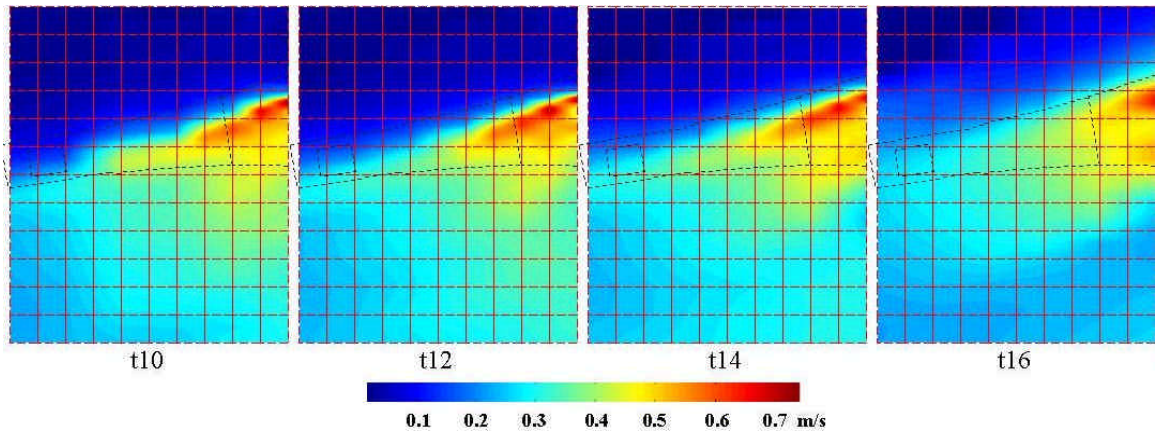

Figure 4.26: Distributions of 2-6 kHz component of rms flow fluctuation.

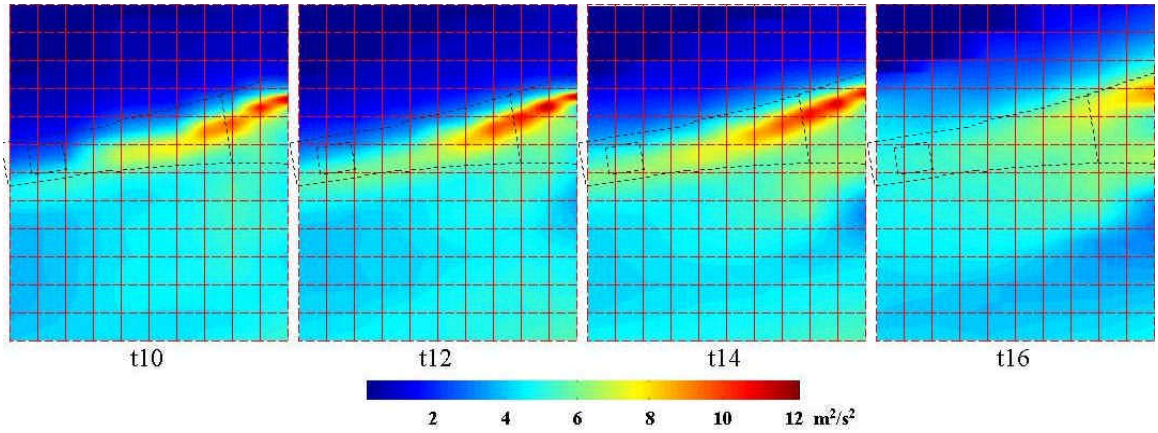

Figure 4.27: Distributions of 2-6 kHz component of rms dynamic head fluctuation.

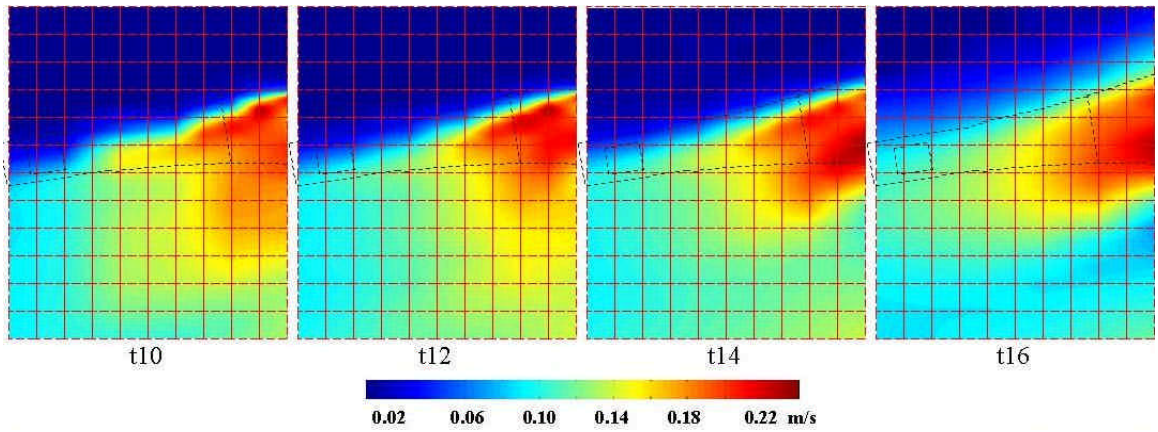

Figure 4.28: Distributions of 6-10 kHz component of rms flow fluctuation.

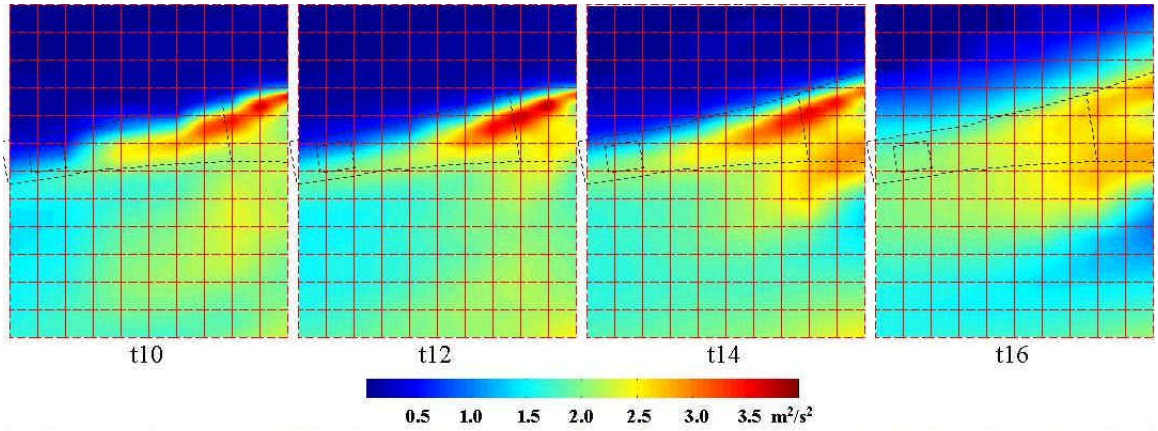

Figure 4.29: Distributions of 6-10 kHz component of rms dynamic head fluctuation.

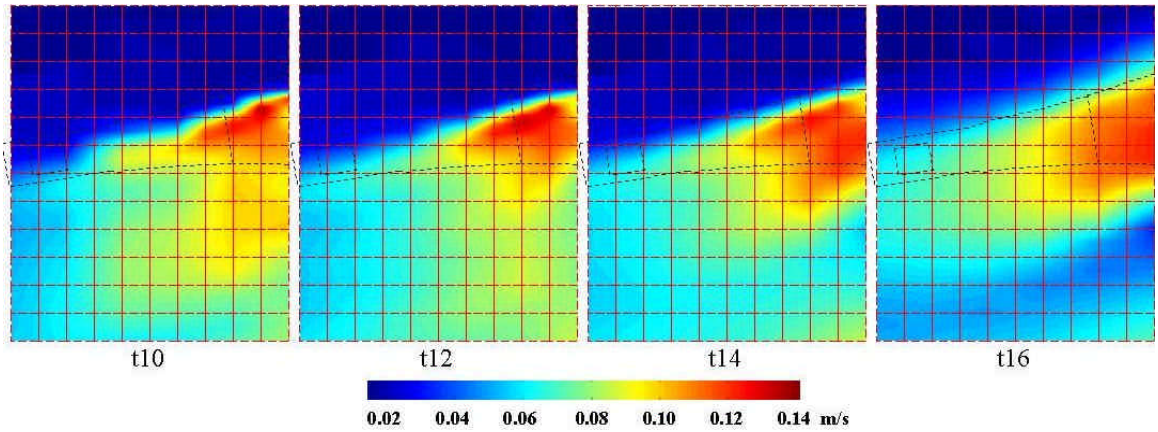

Figure 4.30: Distributions of 10-20 kHz component of rms flow fluctuation.

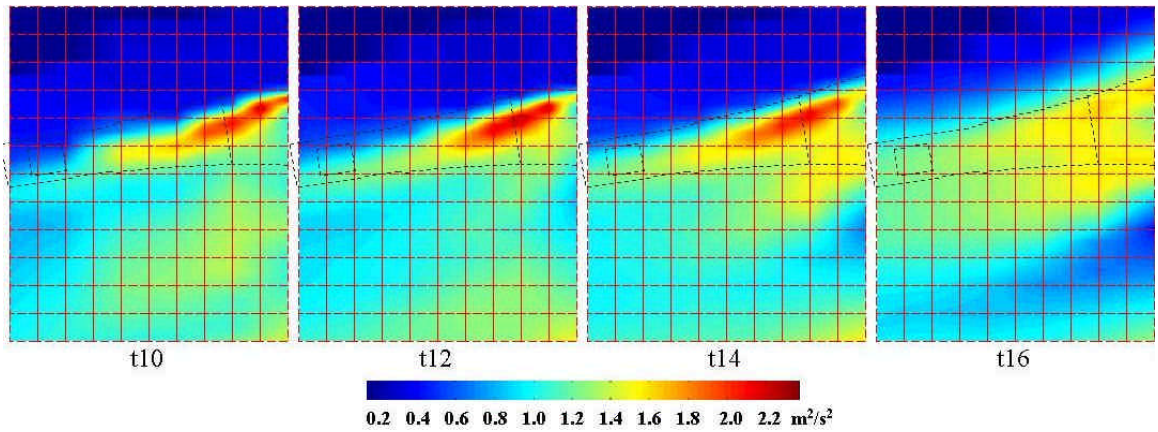

Figure 4.31: Distributions of 10-20 kHz component of rms dynamic head fluctuation.

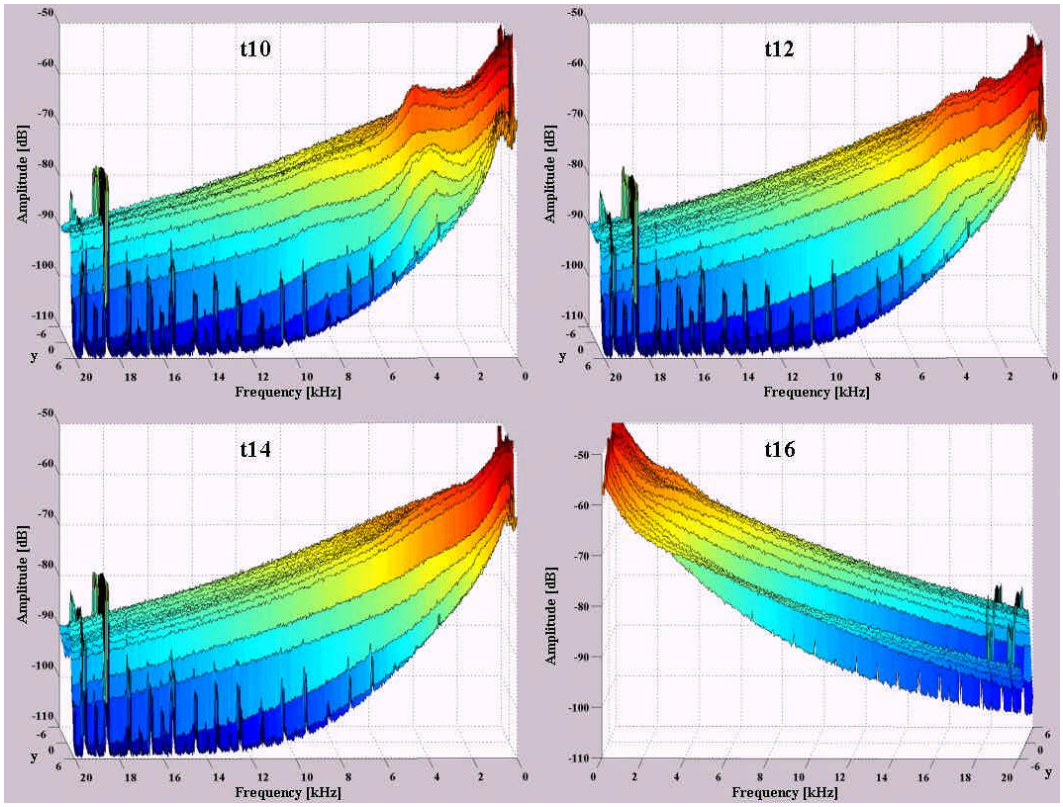

Figure 4.32: Obstructed flow fluctuation power spectra at x = 2 mm.

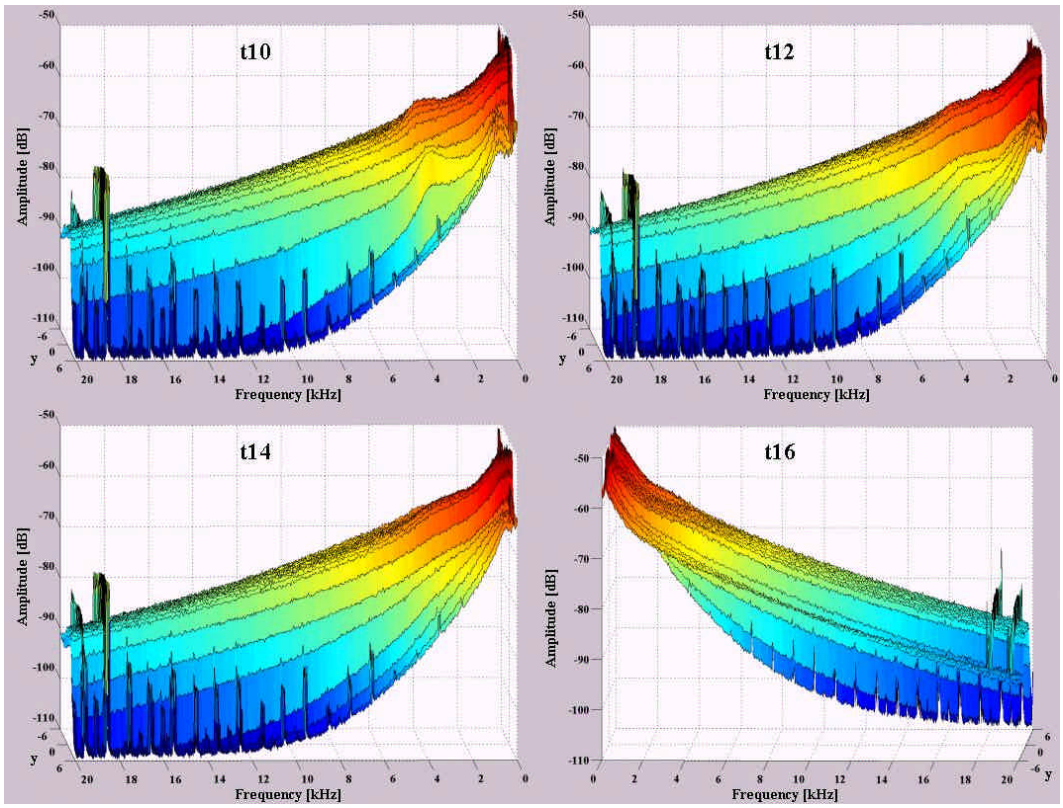

Figure 4.33: Obstructed flow fluctuation power spectra at x = 4 mm.

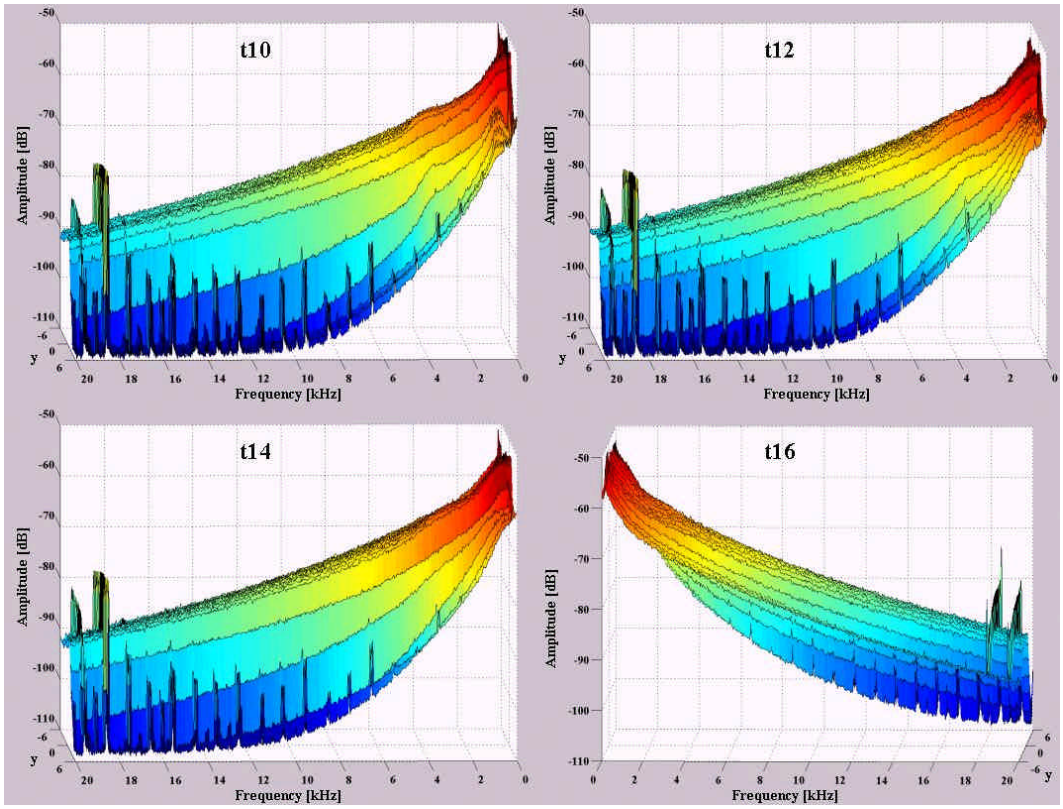

Figure 4.34: Obstructed flow fluctuation power spectra at x = 6 mm.

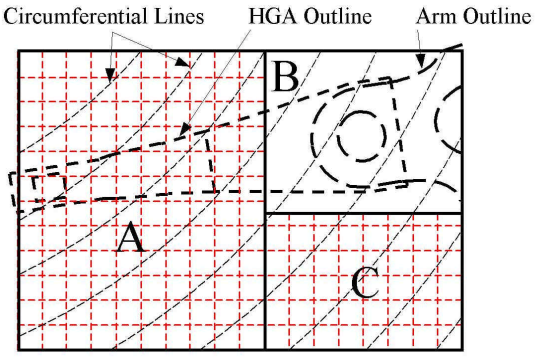

(a) Unobstructed flow measurement

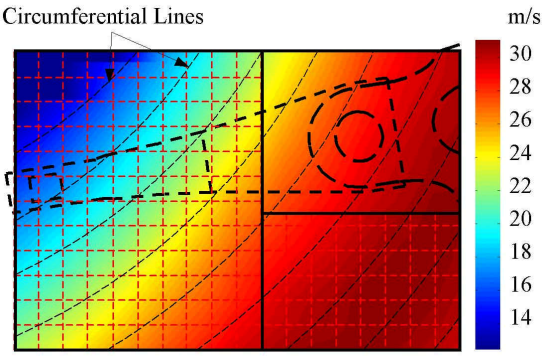

(b) $\overline{u}$

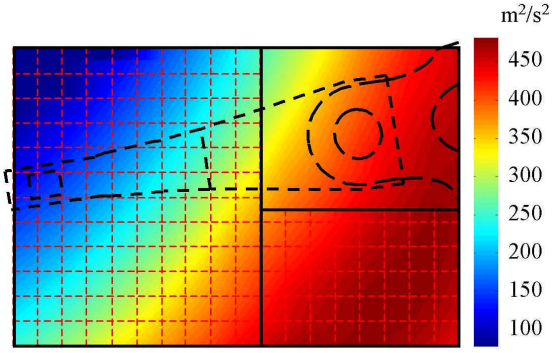

(c) $\overline{h}$

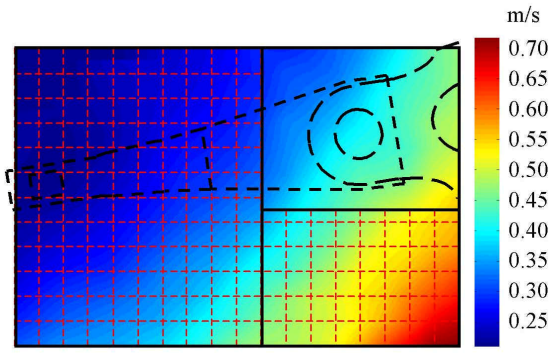

(d) u_{rms}

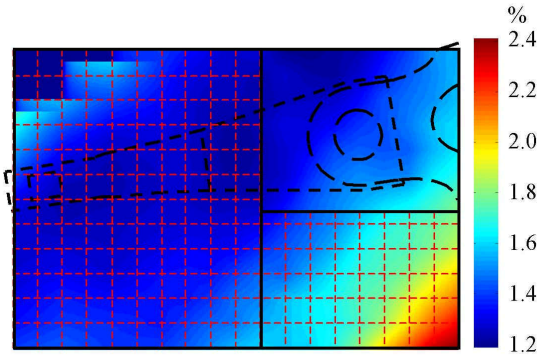

(e) *TI*

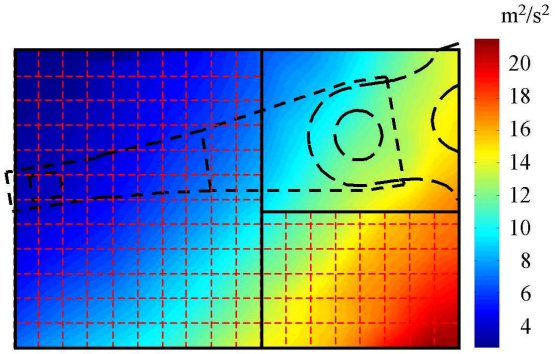

(f) h_{rms}

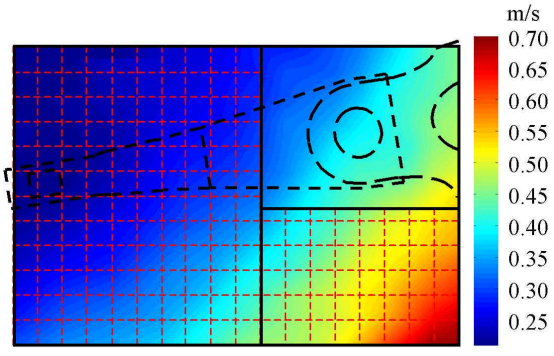

(g) 0-2 kHz component of u_{rms}

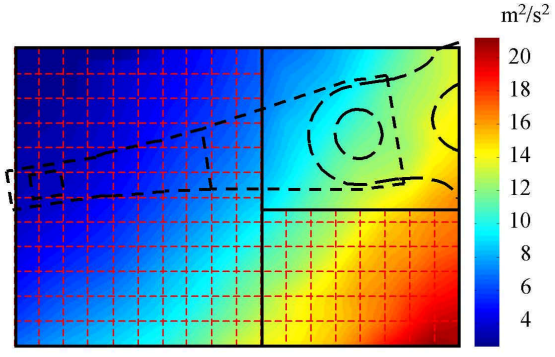

(h) 0-2 kHz component of h_{rms}

Figure 4.35: Unobstructed flow characteristics.

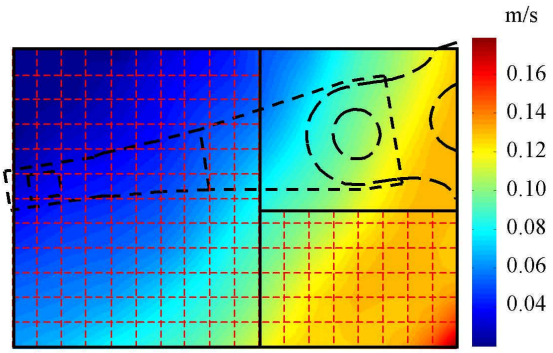

(h) 2-20 kHz component of u_{rms}

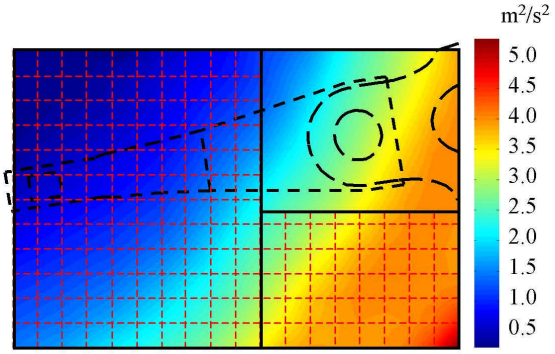

(i) 2-20 kHz component of h_{rms}

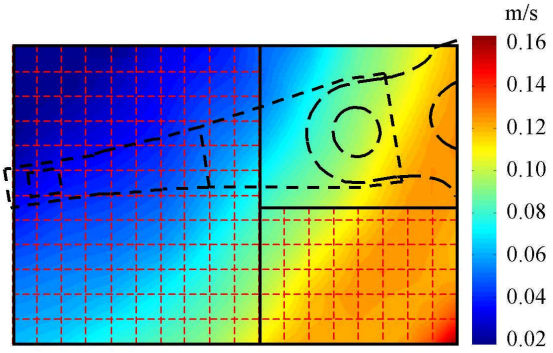

(j) 2-6 kHz component of u_{rms}

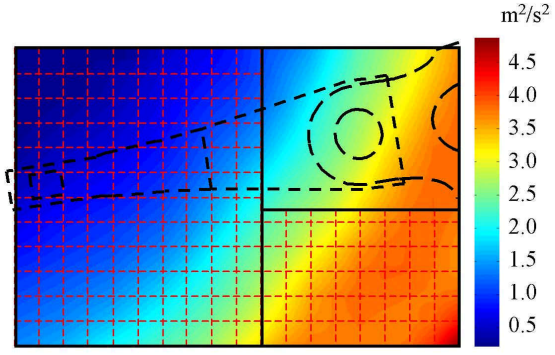

(k) 2-6 kHz component of h_{rms}

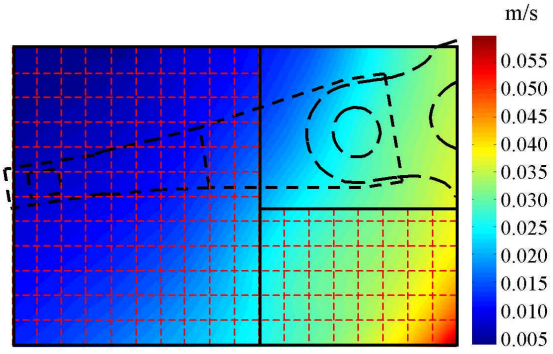

(l) 6-10 kHz component of u_{rms}

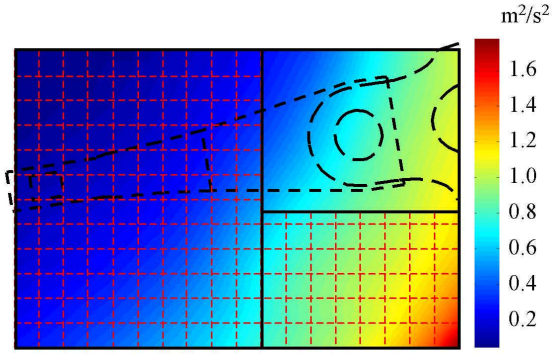

(m) 6-10 kHz component of h_{rms}

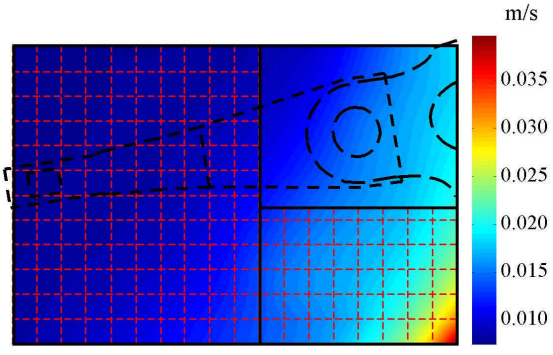

(n) 10-20 kHz component of u_{rms}

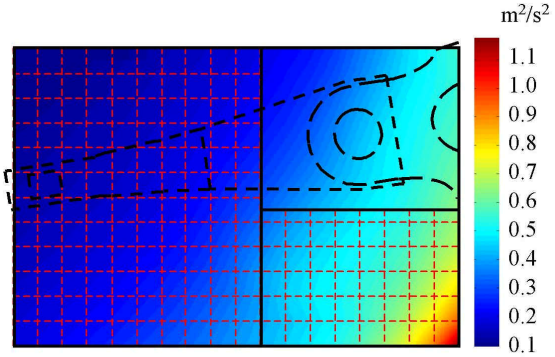

(p) 10-20 kHz component of h_{rms}

Figure 4.35 (continued): Unobstructed flow characteristics.

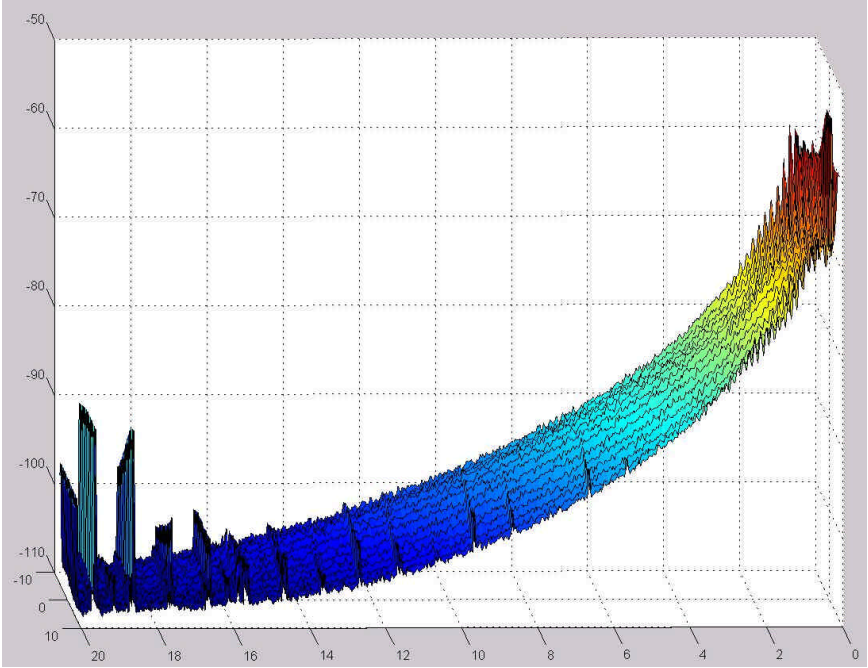

Figure 4.36: Unobstructed flow fluctuation power spectra at x = 2 mm.

CHAPTER 5

THE EFFECTS OF E-BLOCK ARM LEADING EDGE PROFILE ON THE AIRFLOW IN A MODELED HARD DISK DRIVE

5.1. Introduction

The dynamic pressure fluctuations downstream of the E-block arm can be reduced by reducing the flow speed fluctuations in the separated region around the arm. This would reduce the dynamic forces acting on the HSA and the disks, and, in turn, the slider off-track vibrations. The characteristics of the separated region around the arm are governed in part by the geometry of the arm. In this study, the effects of the E-block arm leading edge profile on the airflow in the modeled drive described in §4.2.1 were investigated experimentally. Five leading edge profiles were tested: rectangular, rounded, stepped, chamfered, and U-cut profiles. Airflow measurements were taken in the region downstream of the arm at the ID position using CTA. The specific objectives of this study were to observe the effects of the arm leading edge profile on the local flow characteristics in the region downstream of the arm, and to anticipate the effect of the different profiles on slider vibrations based on the dynamic head fluctuations they generate. In addition, the measurement results obtained in this investigation may serve as an experimental reference for the testing, development, and validation of numerical simulation procedures that aim at predicting the flow in HDDs.

5.2. Experimental Setup and Measurements

The modeled drive and the CTA airflow measurement procedure described in §4.2.1 and §4.2.3 were used in this study. The drive was operated at 10,000 rpm (w = 1,047 rad/s), the disk radius R was 42 mm, the disk thickness 1.0 mm, and the disk spacing 2.0 mm. The arm thickness was 1.0 mm and the arm tip thickness at the swage area was 0.95 mm for all arms. The flow blockage factor at the ID for the arms was 27%. Figure 5.1 illustrates the five profiles used for the E-block arm leading edge.

All of the measurements in this study were taken at the ID position. For each arm, the flow speed was measured in the region downstream of the arm tip with no HGAs attached. The measurement region, shown to scale with the E-block arm in Figure 5.2, was covered by scanning lines perpendicular to the arm trailing edge, starting at x = *-6 mm* and ending at x = 12 mm. The measurement lines were 1 mm apart between x = -6 and x = 6, and 2 mm apart between x = 6 and x = 12. The number and density of the measurement points along each line were determined during the measurement for each arm by starting with a coarse point-to-point step of 1.0 mm, and then refining the step size with additional points to capture any steep gradients and local extrema of the mean flow speed and the rms fluctuation profiles along the line. Steps as small as 0.05 mm between points were sometimes necessary to capture all the desired details of the profiles. At each measurement point, the flow was allowed to settle for a minimum of 1,000 disk revolutions before acquiring the data. The data was processed in accordance with the data analysis presented in §4.3.

5.3. Results and Discussion

The mean and rms flow speed profiles along the measurement lines (not included here) for all arms exhibited steep gradients in the mean flow speed and peaks in the flow fluctuation profiles similar to those presented for t10 in §4.5.2.2. This alluded to the existence of a shear layer in the flow. The rectangular arm will be used as a reference for comparison throughout the discussion that follows.

Figure 5.3 depicts a color contour plot of the disk surface speed. This figure is similar to the schematic of Figure 5.2, with the arm and measurement region rotated slightly to align the *x*-axis with the horizontal. An outline of the E-block arm tip is shown as solid lines, and an outline of the HGA is shown as dashed lines. It should be emphasized that the flow measurements were conducted with no HGAs attached to the E-block arms, and that the HGA outlines are included in this figure, and in subsequent ones, for reference only.

The mean flow speed distributions for the five arms are presented in Figure 5.4. The distributions were generated using different scales, precluding quantitative comparison across the plots, and have been included for a qualitative comparison of the expected main flow direction. The plots for all arms demonstrate a high flow speed region along the upper edge of the HGA outline, with a steep gradient region immediately below it over which the mean speed drops to noticeably lower levels. As the flow fluctuation distributions shown below will illustrate, this steep gradient region also exhibited high-fluctuation levels. As noted earlier, this alludes to the existence of a shear layer in the

flow. Although no direct evidence of the flow direction has been obtained in this investigation, speculations about the flow direction are justified according to the discussion presented in §4.5.2.2. The approximate main flow direction can be inferred from the plots by following the locus of the maximum mean flow speed across the measurement lines, which is indicated by the dark red area. This exercise suggests the flow crossed the HGAs at a greater angle as the arm leading edge is modified from rectangular to any of the other shapes, which implies a greater projection of the area of the HGA onto the flow direction. This is expected to increase the projected area of the body onto the flow direction.

The mean flow speed distributions in the measurement region for the five arms were regenerated using *the same scale* for all arms, and are presented in Figure 5.5. For all arms, there was a high mean flow speed zone along the upper edge of the HGA outline, and a low mean flow speed zone below that, with a steep speed gradient in between. This distribution is attributed to the presence of the arm, as it partially blocks the upstream flow and redirects it towards the gap between the hub and the arm tip. The disk surface speed distribution was also regenerated using the same scale. A comparison of the plots of Figure 5.5 reveals that the flow speed was much lower than the disk surface speed over most of the measurement region, and that in none of the cases did the local speed of air exceed that of the disk surface anywhere in the measurement region. A comparison of these plots also indicates that adding the chamfer, the step and especially the U-cut resulted in elevating the mean flow speed around the HGA outline.

Figure 5.6 presents the rms flow fluctuation distributions for the five arms. The plots demonstrate that modifying the arm profile from rectangular to any of the other shapes resulted in a reduction in the levels of flow fluctuation within the HGA outline, and their dispersion over a larger area. The plots show that the rounded arm resulted in higher levels of fluctuation than the other profiles, and that the stepped arm generated the lowest level of fluctuation within the HGA outline. We believe that this is because the step anchors the separation points along the arm. The high-fluctuation region for all arms began near the upper edge of the HGA outline, and coincided with the steep gradient in the mean flow speed distributions. As noted earlier, this feature is characteristic of a classical shear layer observed in free turbulent flows, and supports the foregoing assertion about the flow direction.

The rms dynamic head fluctuation and the turbulence intensity distributions of the five arms are shown in Figures 5.7 and 5.8, respectively. The stepped arm resulted in the lowest levels of turbulence intensity downstream of the arm tip, and also in the lowest levels of dynamic head fluctuation within the HGA outline. The dynamic head fluctuation levels for the rounded arm were also low, in spite of its high flow speed fluctuation levels, on account of its lower mean flow speed.

The mean dynamic head color contour plots are shown in Figure 5.9. These distributions follow the same trend as that observed for the mean flow speed distributions: a result which is expected due to the approximation given in Eq. (4.11).

In order to better assess the effect of the leading edge profile on the character of the flow, we decomposed the rms flow fluctuation and the rms dynamic head fluctuation into components over the frequency bands considered in §4.5. Namely, the rms fluctuations were decomposed into components over the 0-2 kHz and the 2-20 kHz frequency bands. The contributions of the 0-2 kHz components to the overall fluctuations were noticeably greater than those of the 2-20 kHz components. The 2-20 kHz components were further divided into subcomponents over the 2-6 kHz, the 6-10 kHz, and the 10-20 kHz frequency bands. Figures 5.10 through 5.19 depict the distributions of these components. The figures indicate that the stepped arm resulted in the lowest levels of all components of the dynamic head fluctuation, especially within the HGA outline, which renders it the most promising geometry for reducing the head vibration.

Figure 5.20 depicts the power spectra of the hot-wire anemometer output at the measurement points along the line at x = 2 mm for the five arms. The plots are three-dimensional, with frequency on the horizontal axis, dB amplitude on the vertical axis, and y-position (along the x = 2 mm line) on the third axis. Each curve within a plot represents the power spectrum at the indicated y-position along the measurement line, and the color contour has also been included to emphasize the magnitude of the power spectra. All power spectra exhibited a peak at 167 Hz, which coincides with the disk rotation speed, and is attributed to disk runout. The power spectra illustrate the dominance of the low frequency components; the high frequency energy is more pronounced only in the range of y = -6 to 0.5 mm. The plots also reveal the presence of clearly identifiable peaks in the power spectra, which we identify with vortex shedding. A clear vortex shedding peak

was observed in the power spectra of the rectangular arm, whereas two clear vortex shedding peaks were observed in the power spectra of all other arms along the x = 2 mm line. The frequencies of these peaks, f_v, are listed in Table 5.1. These are the frequencies in the separated region and the shear layer, and were generated by the flow separation from the arm.

The vortex shedding frequencies for the free flow over a cylinder with U = 20 m/s and a characteristic diameter l = 1.0 mm can be estimated using St = 0.21. This yields $f_{cyl,t}$ = 4.2 kHz. The expected vortex shedding frequency using a characteristic diameter of l = 0.95 mm, which corresponds to the arm tip thickness, is $f_{cyl,t}$ = 4.4 kHz. The flow conditions over the arm in the modeled HDD are completely different from those of free flow over a cylinder, and the vortex shedding frequencies estimates $f_{cyl,t}$ cannot be used to estimate the vortex shedding frequencies for the arms. However, a comparison of $f_{cyl,\mathrm{t}}$ and f_v (Table 5.1) indicates that the cylinder shedding frequency estimates provide a reasonable approximation of the frequencies observed.

5.4. Conclusion

The effects of E-block arm leading edge profile on the flow in the region downstream of the arm tip at the ID position were investigated experimentally in a modeled drive. The mean flow speed and the flow fluctuation power spectra were measured using a single-sensor hot-wire anemometer at the mid-plane between two disks, in the presence of an arm with no HGAs attached. The measurements were carried out for five arms with rectangular, rounded, stepped, U-cut, and chamfered profiles, and were used to compute

the mean and rms flow speed, the turbulence intensity, the mean and rms dynamic head, and the rms components of the flow fluctuation and the dynamic head fluctuation over several frequency bands. Modifying the arm profile from rectangular to any of the other shapes resulted in a reduction in the levels of flow fluctuation within the HGA outline, and their dispersion over a larger area. The stepped arm generated the lowest levels of dynamic head fluctuation, and it is expected to be the most promising geometry of those studied for reducing head vibration. The flow fluctuation power spectra revealed the presence of clearly identifiable vortex shedding peaks for all five arms.

Arm	f_v [kHz]
Rectangular	3.7
Chamfered	3.3, 4.4
Stepped	3.1, 4.5
Rounded	3.3, 4.3
U-cut	3.3, 4.4

Table 5.1: Observed vortex shedding frequencies.

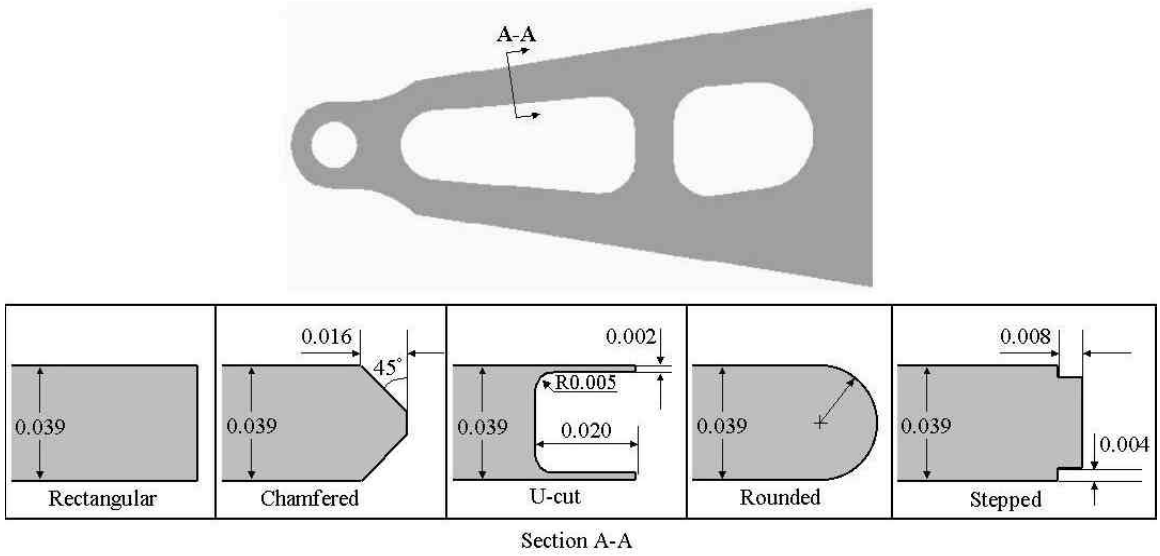

Figure 5.1: E-block arm leading edge profiles.

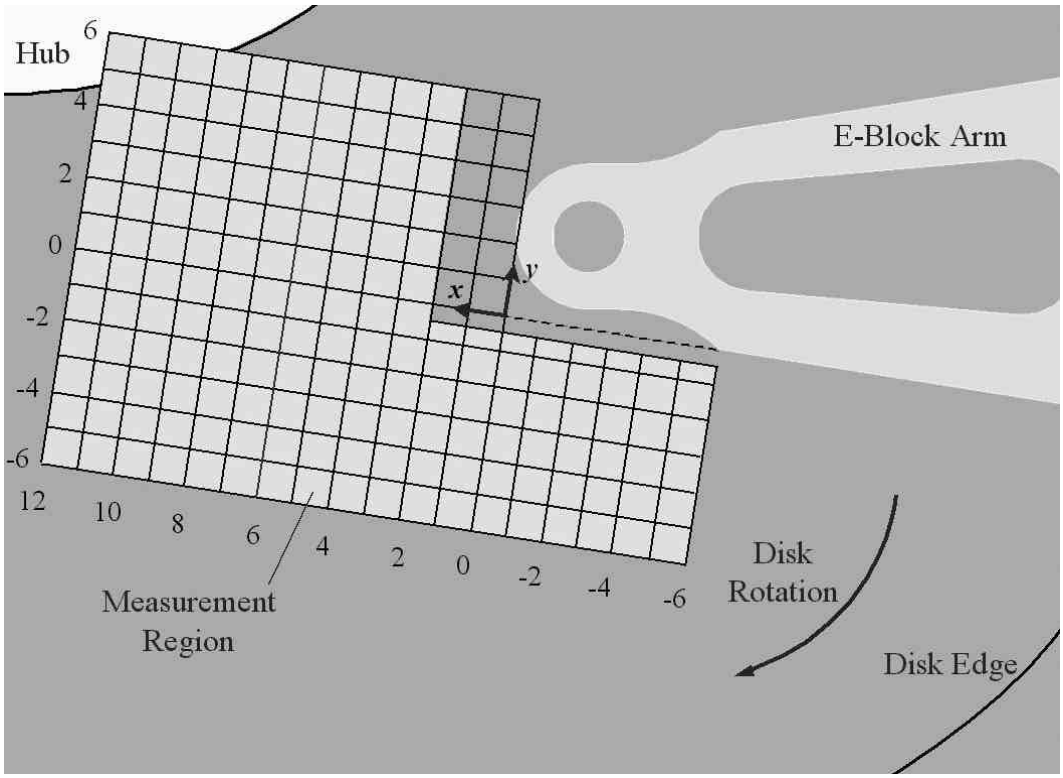

Figure 5.2: Airflow measurement region.

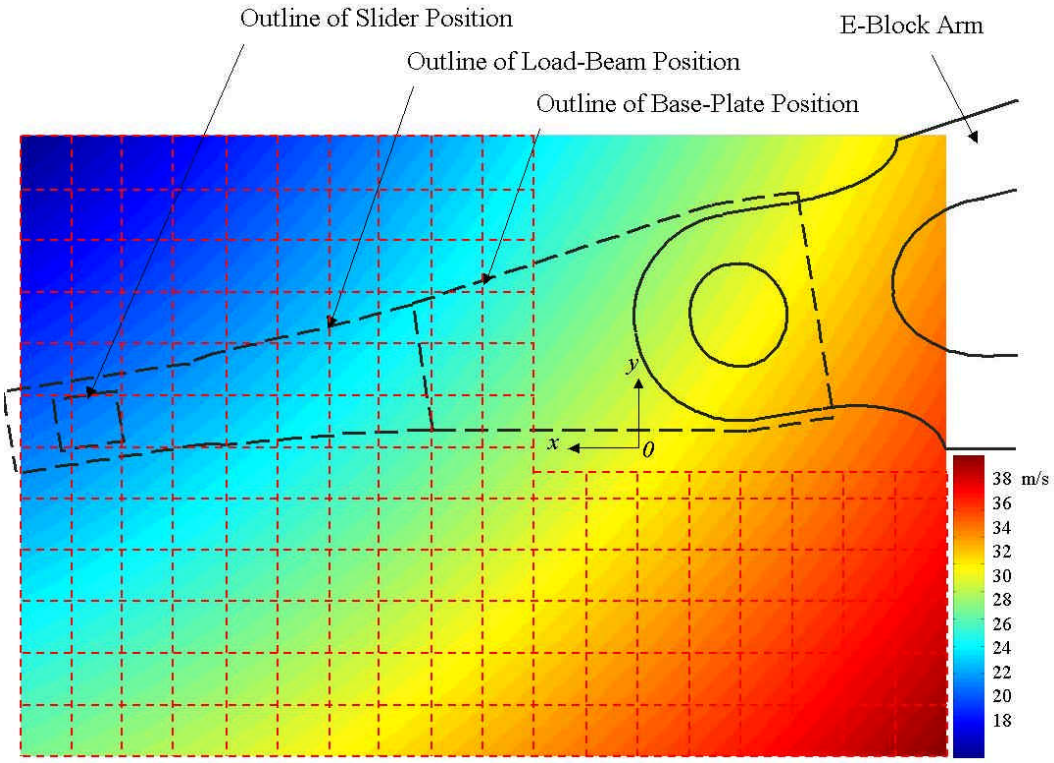

Figure 5.3: Disk surface speed.

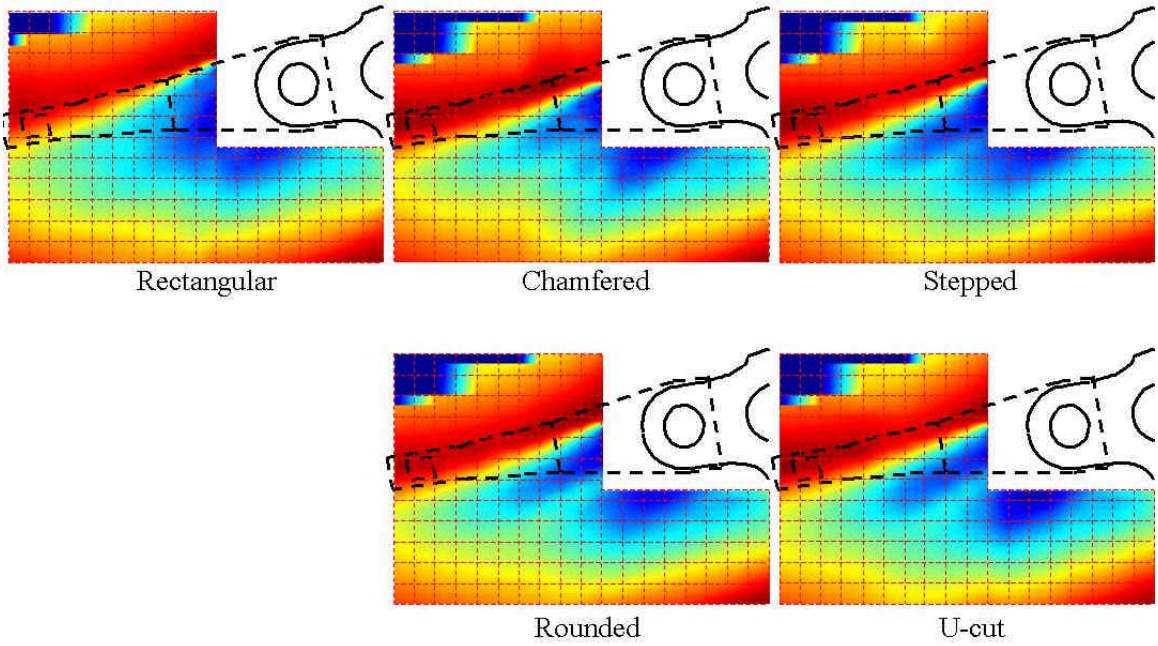

Figure 5.4: Mean flow speed distributions; different scales.

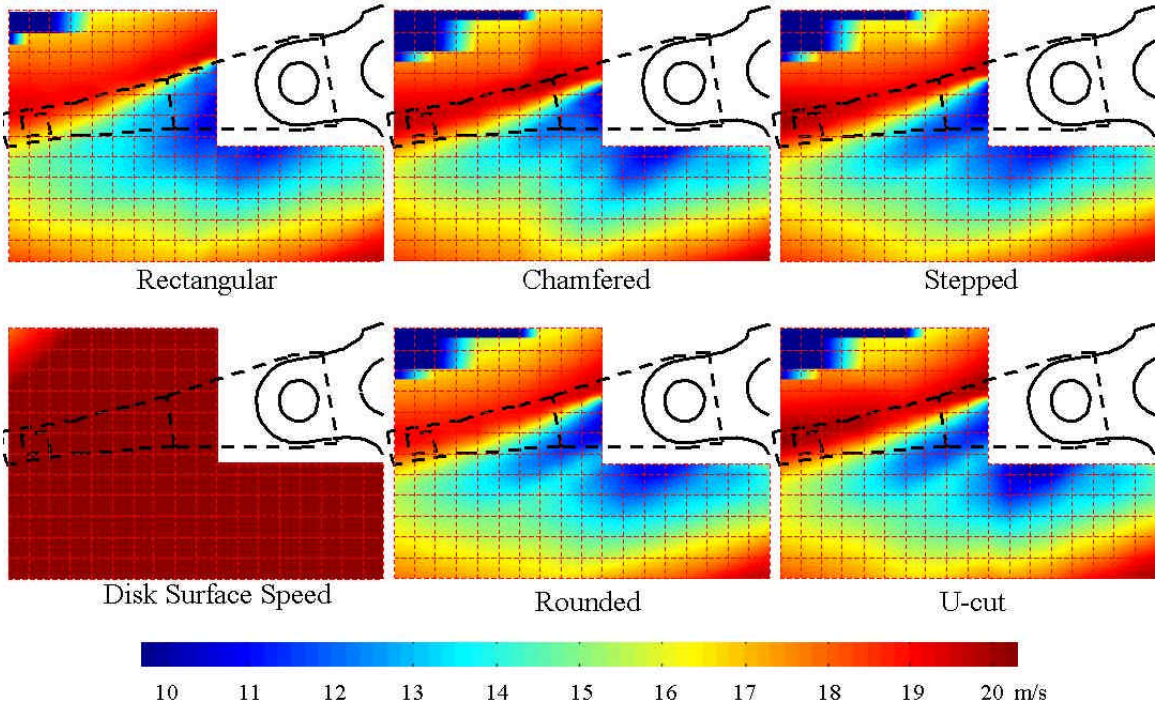

Figure 5.5: Mean flow speed distributions; same scale.

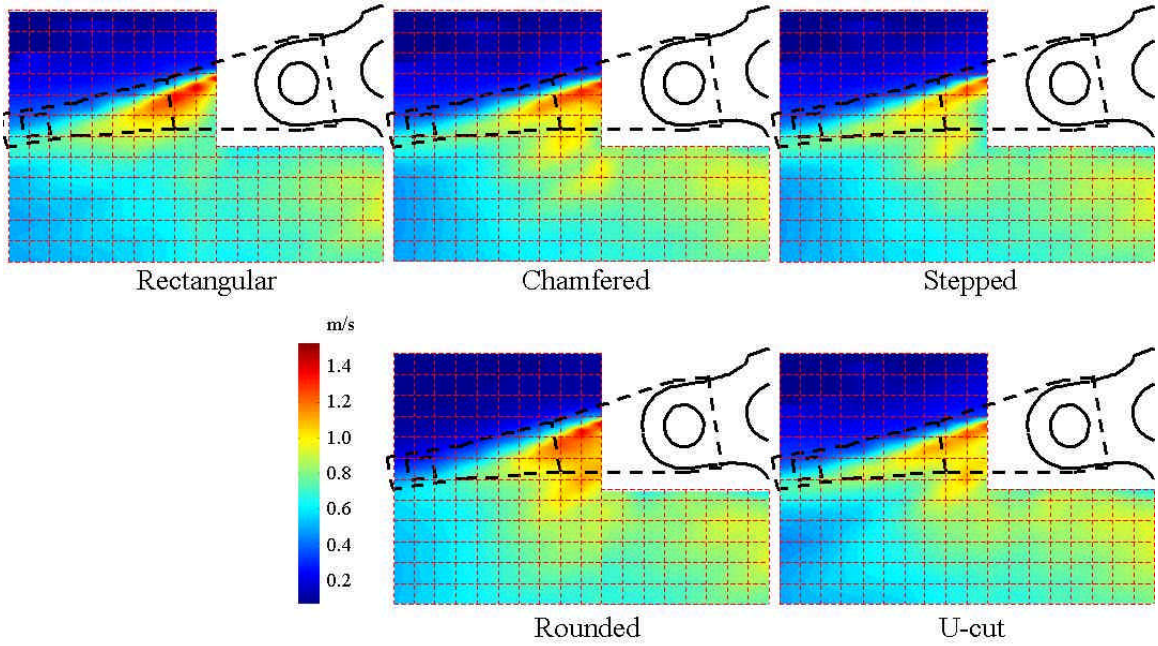

Figure 5.6: RMS flow fluctuation distributions.

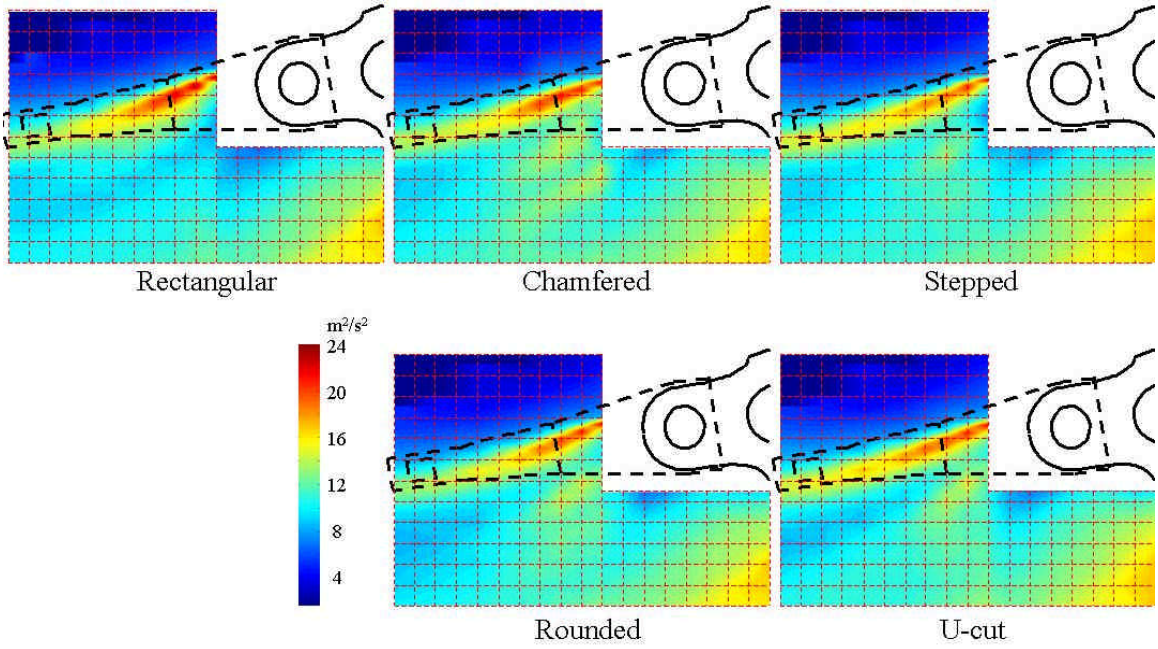

Figure 5.7: RMS dynamic head fluctuation distributions.

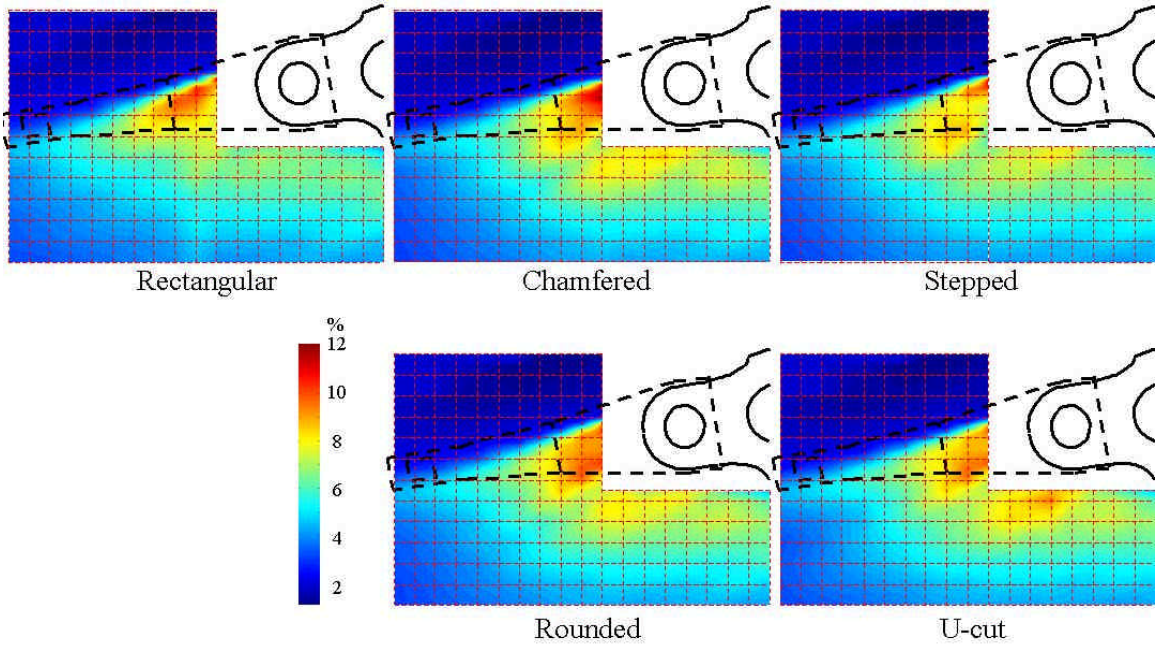

Figure 5.8: Turbulence intensity distributions.

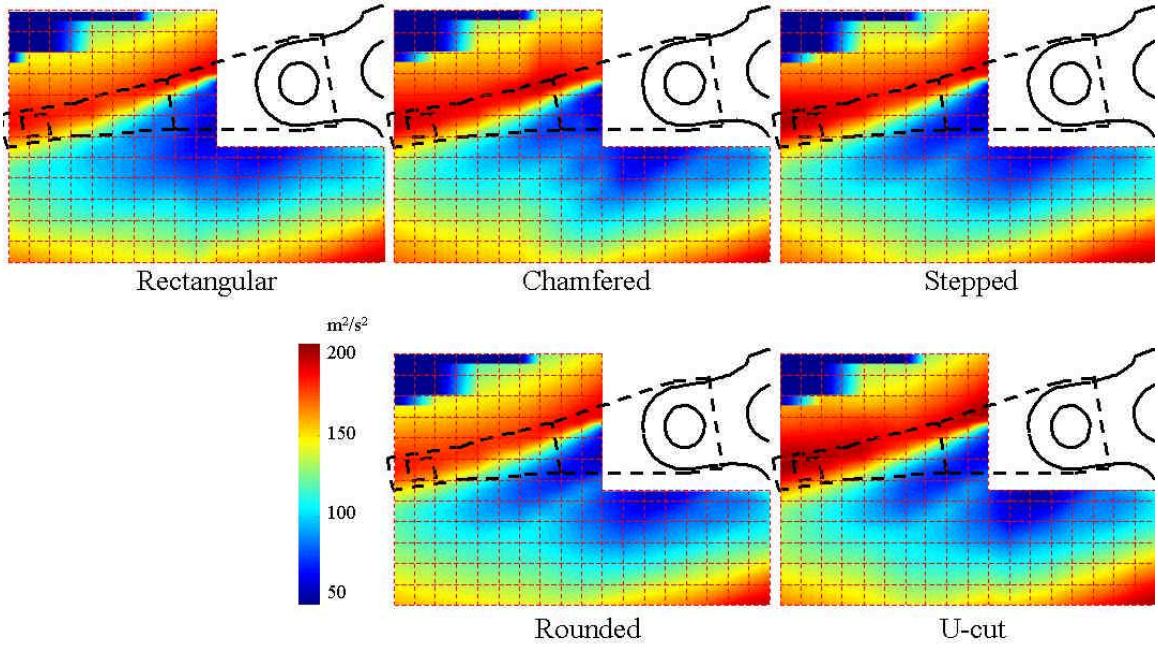

Figure 5.9: Mean dynamic head distributions.

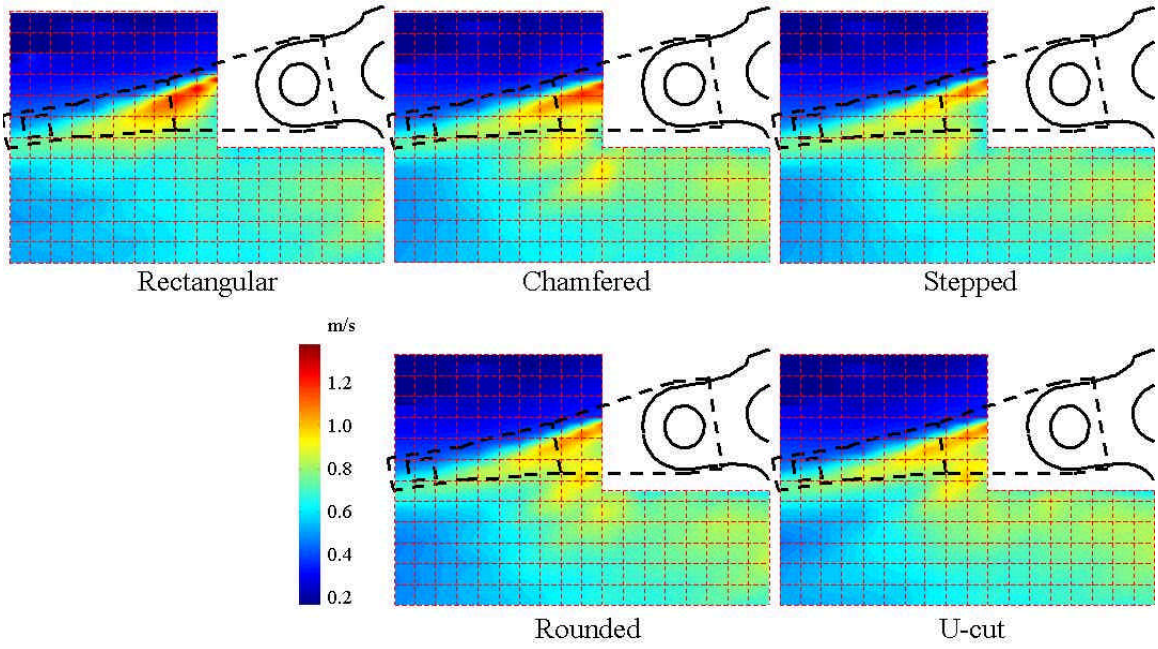

Figure 5.10: Distributions of 0-2 kHz component of rms flow fluctuation.

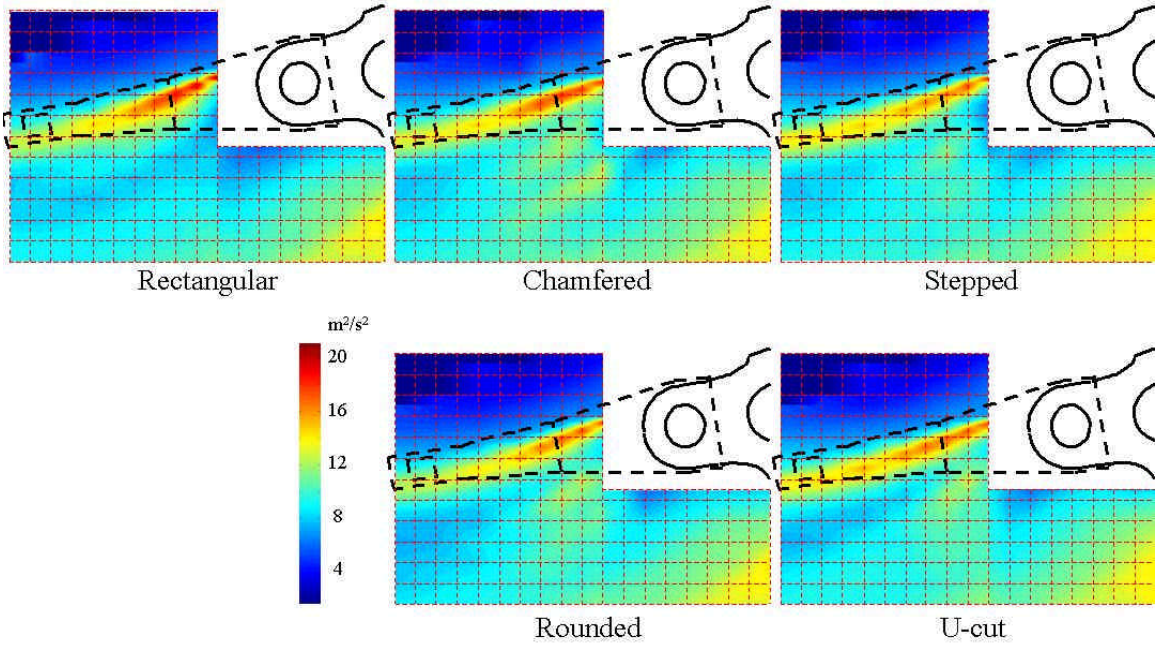

Figure 5.11: Distributions of 0-2 kHz component of rms dynamic head fluctuation.

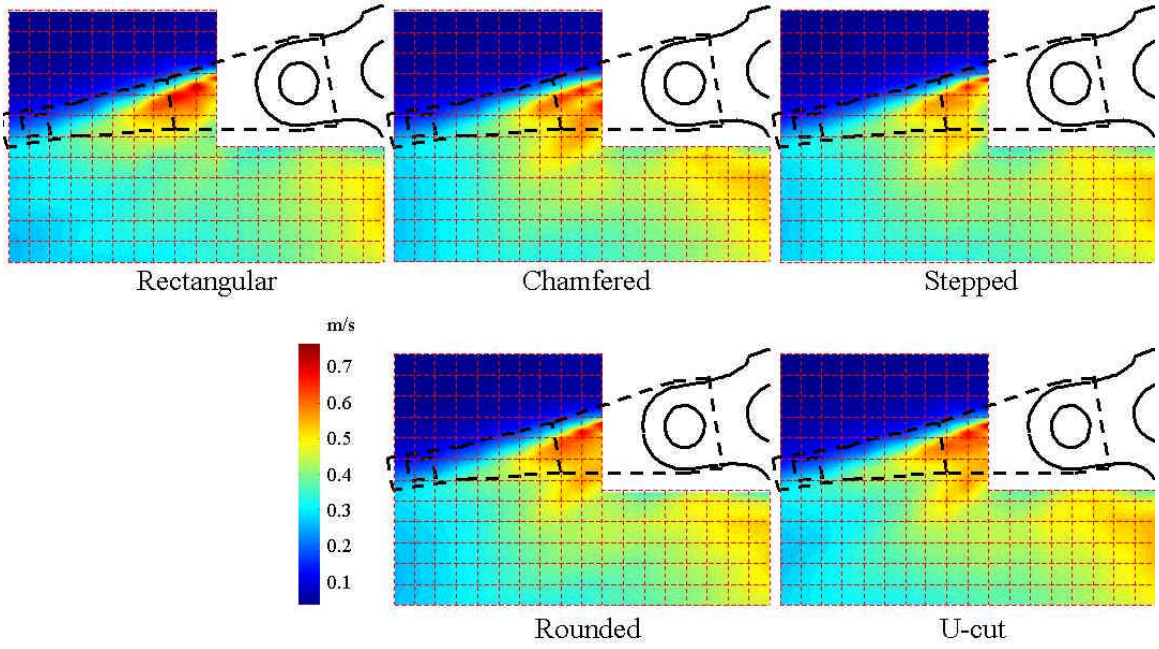

Figure 5.12: Distributions of 2-20 kHz component of rms flow fluctuation.

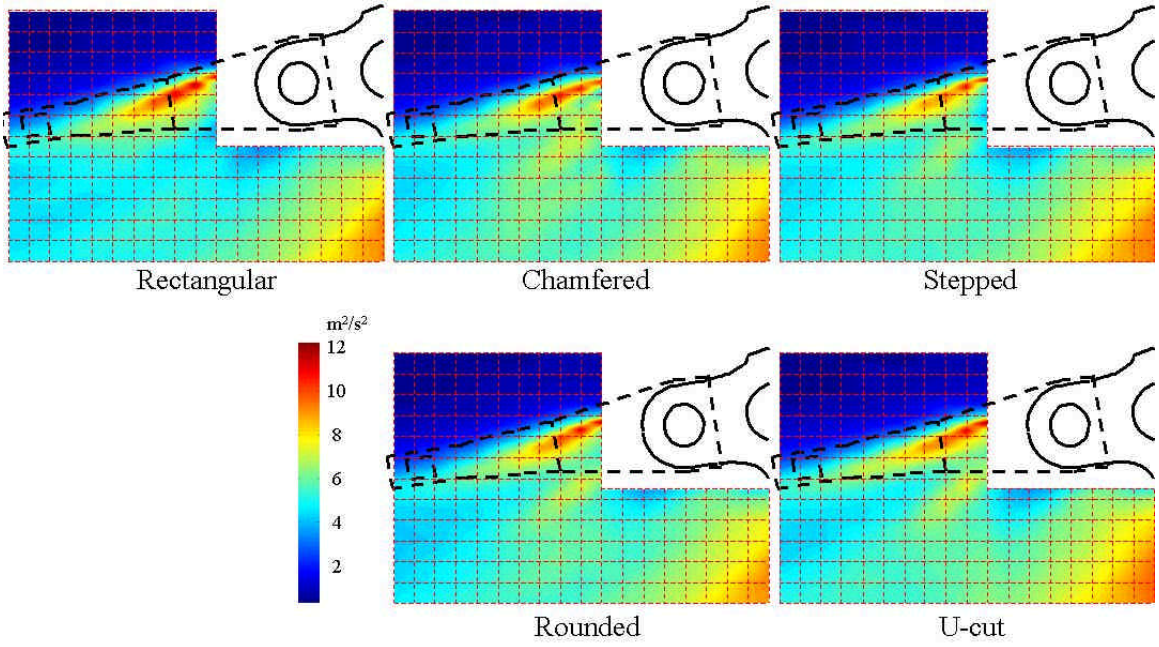

Figure 5.13: Distributions of 2-20 kHz component of rms dynamic head fluctuation.

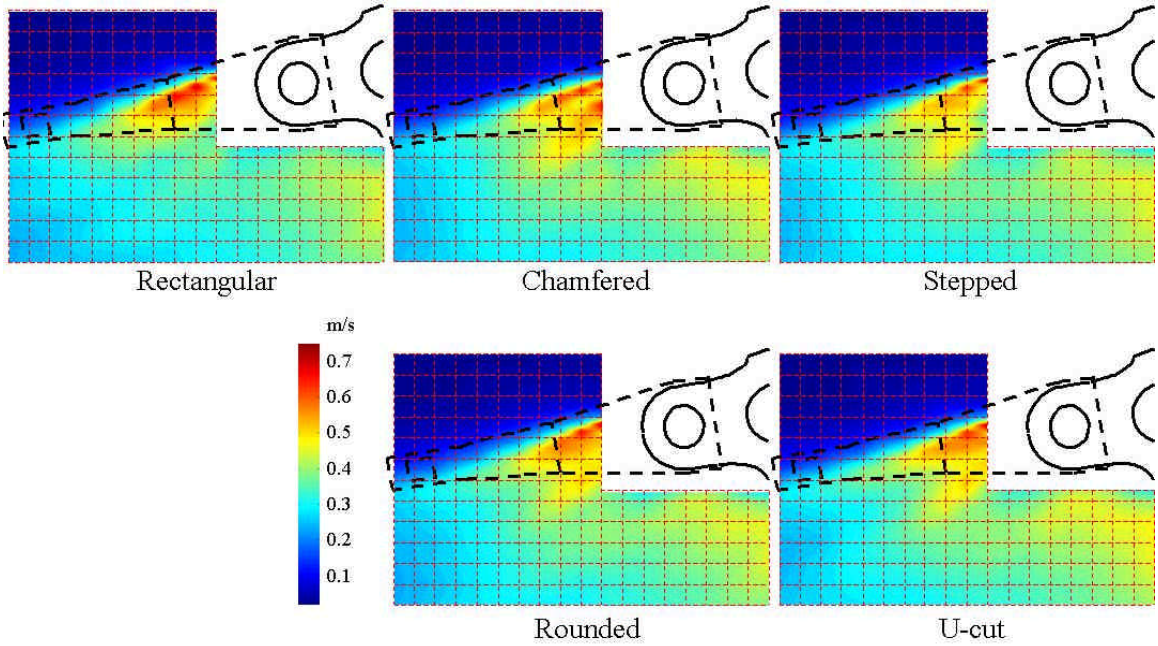

Figure 5.14: Distributions of 2-6 kHz component of rms flow fluctuation.

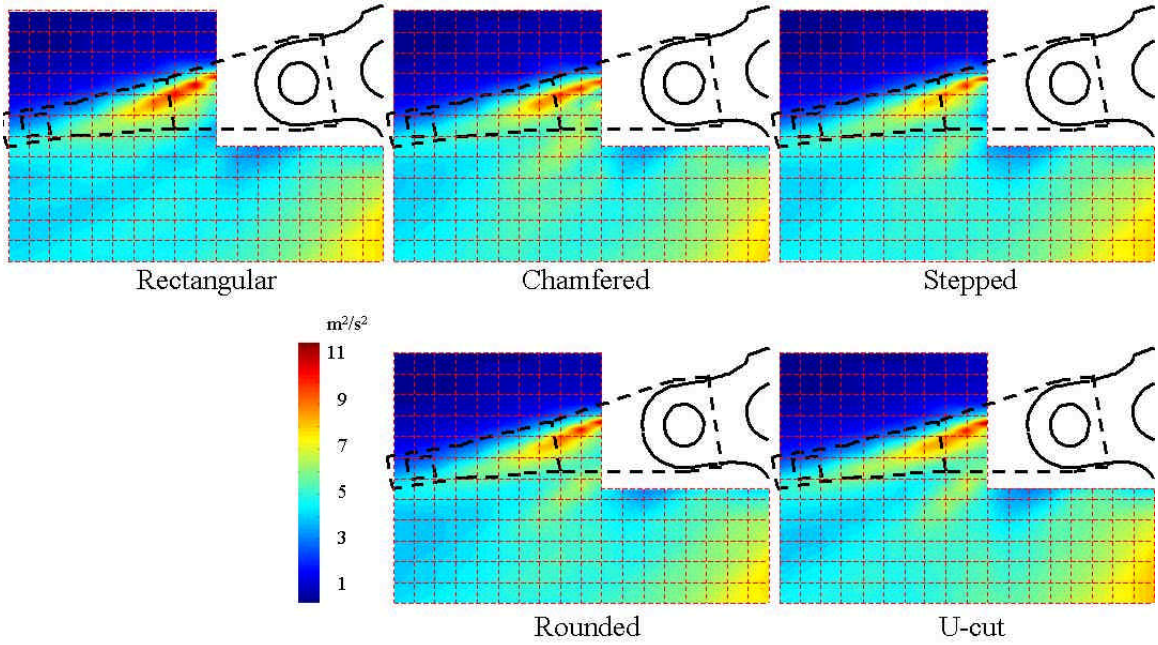

Figure 5.15: Distributions of 2-6 kHz component of rms dynamic head fluctuation.

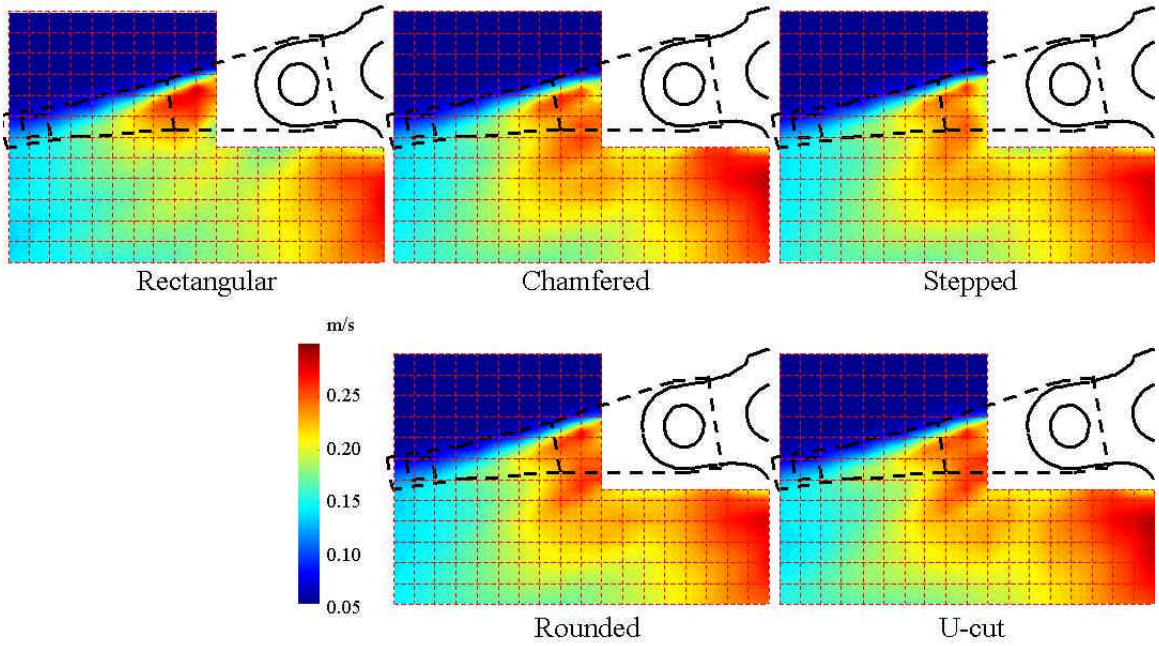

Figure 5.16: Distributions of 6-10 kHz component of rms flow fluctuation.

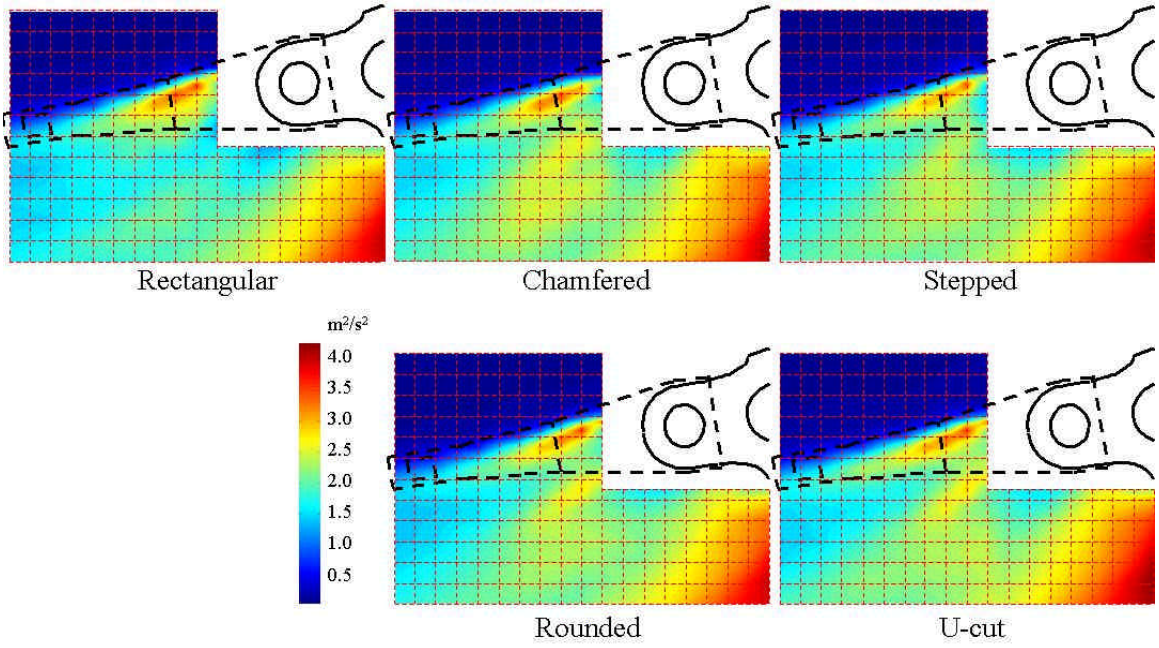

Figure 5.17: Distributions of 6-10 kHz component of rms dynamic head fluctuation.

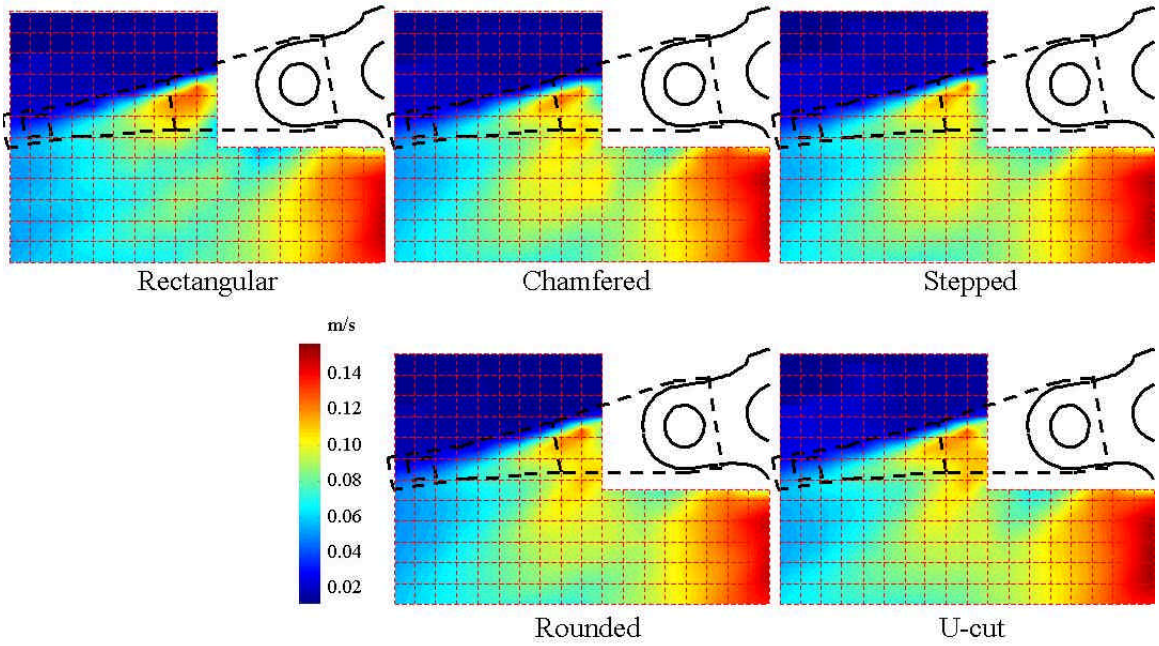

Figure 5.18: Distributions of 10-20 kHz component of rms flow fluctuation.

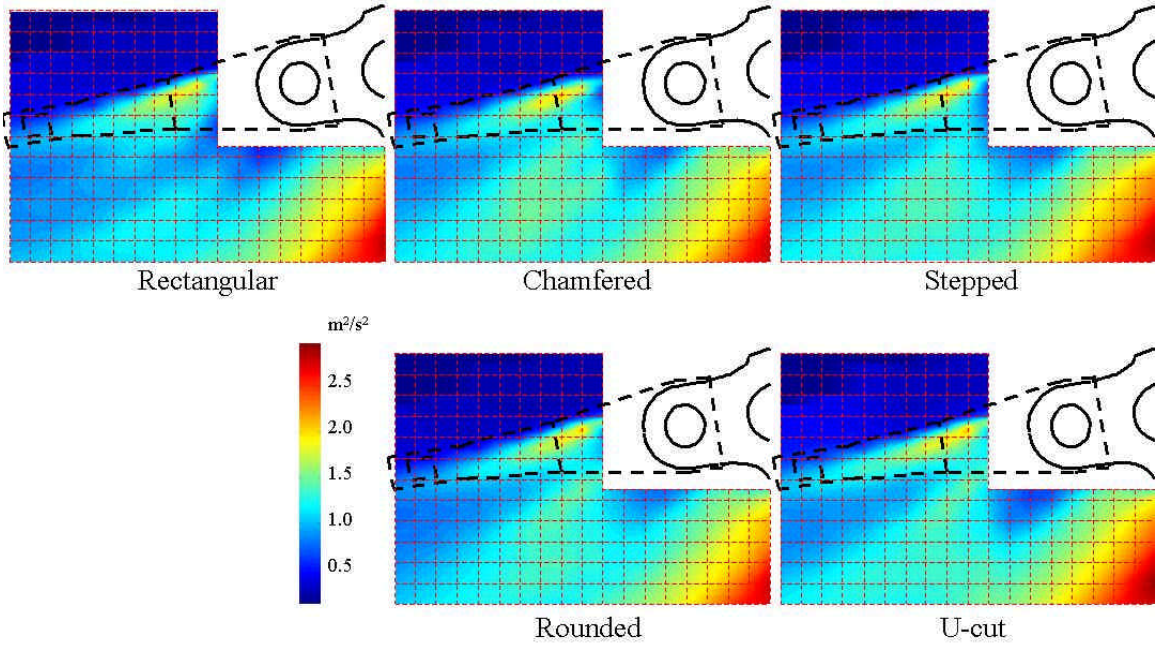

Figure 5.19: Distributions of 10-20 kHz component of rms dynamic head fluctuation.

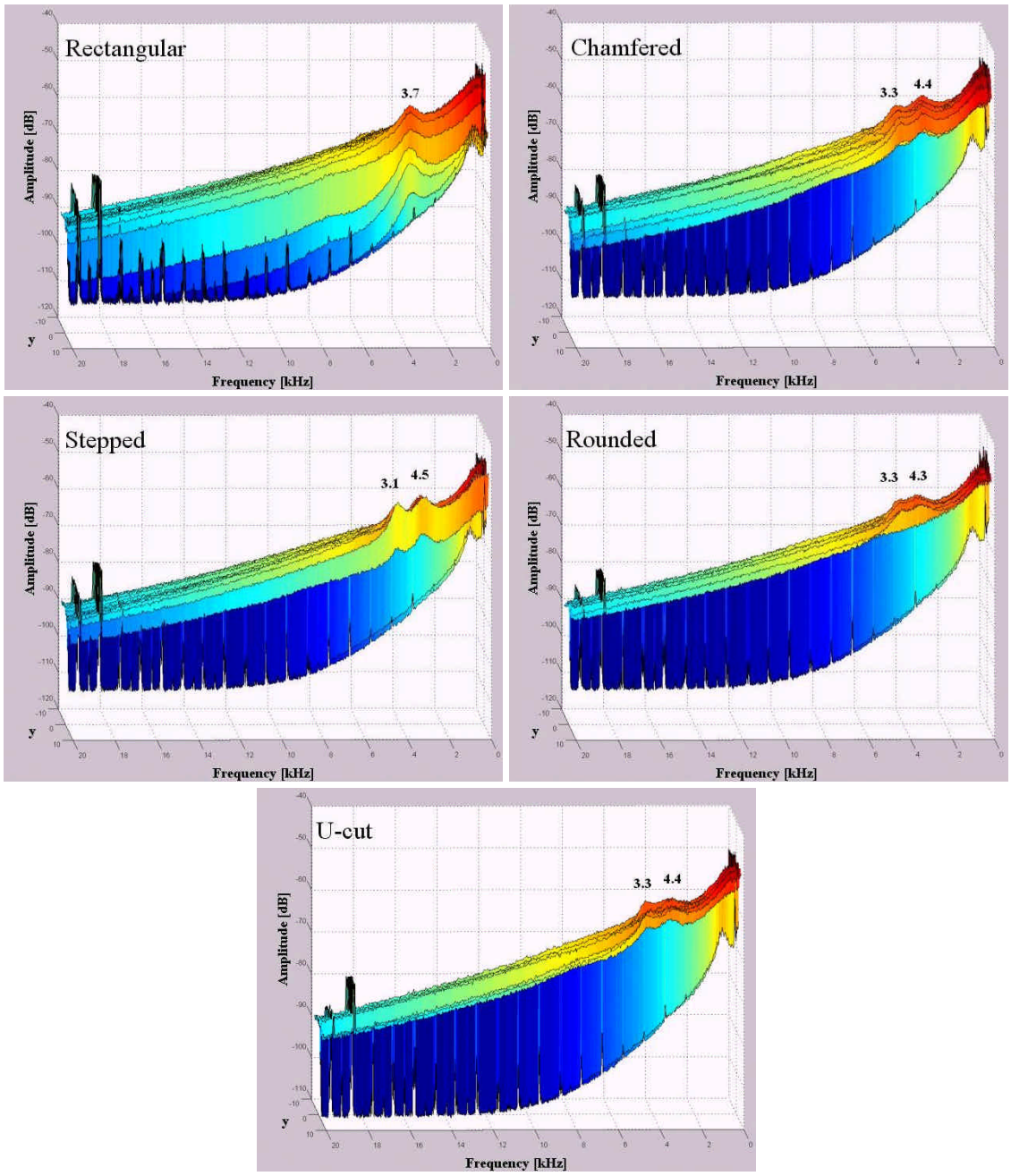

Figure 5.20: Flow fluctuation power spectra at x = 2 mm.

CHAPTER 6

SUMMARY AND CONCLUSIONS

Increasing the areal storage density of hard disk drives is a challenging task that requires many technological advances to support higher track and linear bit densities. Increasing the track density can be achieved by reducing component disturbances that move the read-write heads off-track, improving the structural characteristics of drive components so that their response to disturbances is attenuated, and enhancing the ability of the servo controller to keep the heads on narrower tracks.

The research presented in this dissertation was aimed at investigating and mitigating off-track vibrations of read-write heads in hard disk drives. It addressed three objectives. The first objective was to study and understand drive dynamics at the system level. The second objective was to determine the optimal orientation of strain sensors on an instrumented suspension to detect suspension vibrations that may contribute significantly to the off-track motion of the read-write head. These strain measurements would provide real-time suspension vibration information that can be employed in control schemes to suppress off-track vibrations. The third objective was to experimentally study and characterize airflow effects in hard drives, and to reach a better understanding of the relationship between airflow and head vibration.

A thorough understanding of drive dynamics is an essential prerequisite to accurate structural identification, modification, analysis, and design. In chapter 2, we studied the

dynamics of the head stack assembly using finite element modeling and analysis. The approach we adopted was to examine the dynamics of the individual components of the head stack assembly and then investigate the dynamic characteristics of the system as a whole in terms of the component dynamics and their coupling. The head stack assembly modes that can potentially contribute significantly to off-track vibrations of the read-write heads were identified as the suspension sway and torsion modes, the actuator rigid body and butterfly modes, and the sway and torsion modes of the E-block arms. The coupling between the HGAs generated several modes that could be grouped into sets corresponding to the familiar single-suspension modes. In addition, some HGA modes were driven by E-block modes that were close in frequency.

The use of strain sensors for active vibration control capitalizes on the idea of strategically attaching strain sensors to measure localized strains at key locations on drive structures, so that the sensors will effectively detect structural vibrations that may result in off-track motion of the heads. In chapter 3, we determined the optimal location and orientation of strain sensors on an instrumented suspension based on the degree of observability of suspension modes that contribute to off-track vibration of the heads. The optimal location was on the suspension load-beam bend area. In addition, we identified the four locations on the load-beam with the highest degree of observability of the selected modes for implementations in which four strain gauges are arranged in a *Wheatstone* bridge circuit, in a configuration that would increase the sensitivity of the measurement. These four locations were on the suspension load-beam bend area.

The airflow in the drive presents a significant disturbance to the read-write head motion as it excites the structural modes of the actuator and the disks. It is anticipated that airflow-induced vibrations will pose a major and critical obstacle in the path to achieving the higher track densities. Consequently, understanding the nature and characteristics of the airflow in disk drives, as well as its impact on structural vibrations, is key to designing drive components to reduce flow-induced vibrations and improve the performance of future drive generations. In chapter 4, we experimentally investigated the effects of E-block arm thickness on the off-track vibrations of the read-write heads and the airflow in a modeled drive. Four arms with thicknesses 1.0, 1.2, 1.4 and 1.6 mm were tested. The power spectra of the head vibrations were measured using laser Doppler vibrometry, and were used to compute the rms off-track vibrations. The mean speed and flow fluctuation power spectra of the airflow downstream of the arm tip were measured using hot-wire anemometry, and these measurements were used to compute the rms dynamic head fluctuations in the measurement region.

The primary contributors to the off-track vibrations were identified as the E-block arm sway mode, the suspension second torsion mode, and the suspension sway mode. The rms off-track vibrations and rms dynamic head fluctuations were decomposed into components over several frequency bands. The off-track vibrations and the dynamic head fluctuations were dependent on E-block arm thickness. There was a positive correlation between the trend followed by the rms off-track vibration components and the corresponding rms dynamic head fluctuation components. Specifically, a positive

correlation was observed between these components over the 0-20 kHz, 0-2 kHz, 2-20 kHz, 6-10 kHz, and 10-20 kHz frequency bands.

In chapter 4, we experimentally investigated the effects of E-block arm leading edge profile on the airflow in a modeled drive. The mean flow speed and the flow fluctuation power spectra were measured using hot-wire anemometry. The measurements were carried out for five arms with rectangular, rounded, stepped, U-cut, and chamfered profiles, and were used to compute the rms dynamic head fluctuations and their components over several frequency bands. Modifying the arm profile from rectangular to any of the other shapes resulted in a reduction in the levels of flow fluctuation within the HGA outline, and their dispersion over a larger area. The stepped arm generated the lowest levels of dynamic head fluctuation, and is expected to be the most promising geometry for reducing head vibrations.

REFERENCES

[1] Daniel, E. D., Mee, C. D., and Clark, M. H., Magnetic Recording The First 100 Years, IEEE Press, New York, 1999.

[2] IBM Almaden Research Center Website, http://www.almaden.ibm.com/sst/storage/mechanics/microdrive.shtml.

[3] Seagate website, http://www.seagate.com/newsinfo/technology/d4g.html.

[4] Western Digital Corporation Website, http://www.wdc.com/en/products.

[5] Mee, C. D., and Daniel, E. D., Magnetic Recording Handbook, McGraw-Hill, New York, 1996.

[6] Read-Rite Corporation Website, http://www.readrite.com/html/magbasic.html.

[7] Bhushan, B., Tribology and Mechanics of Magnetic Storage Devices, Springer, New York, 1996.

[8] Wood, R., "The Feasibility of Magnetic Recording at 1 Terabit per Square Inch," IEEE Transactions on Magnetics, vol. 36, pp. 36-42, January 2002.

[9] Menon, A., "Critical Requirements for 100 Gb/in^2 Head/Media Interface," Proceedings of the Symposium on Interface Technology Towards 100 Gb/in^2, ASME, Tribology, Vol. 9, pp. 1-9, 1999.

[10] Okawa, R., Terada K., Ito, K., Watanabe, S., Imai, T., and Tanihira, K., "Modal Analysis of HDD's Actuators," Fujikura Technical Review, 2002.

[11] Yoshida, T., Hirai, H., et al., "Vibration Reduction of a Small Magnetic Disk Drive Using a Nonreacting, Twin-Drive Actuator," ASME, Advances in Information Storage Systems, Vol. 6, 1995, pp. 289-300.

[12] Ku, C. P. R., "Dynamic Characteristics of Hard Disk Drive Spindle Motors – Comparison Between Ball Bearings and Hydrodynamic Bearings," ASME, Journal of Tribology, Vol. 118 (2), April 1996, pp. 402-406.

[13] McAllister, J. S., "The Effect of Platter Resonances on Track Misregistration in Disk Drives," Journal of Sound and Vibration, January 1996, pp. 24-28.

[14] Zeng, Q. H., and Bogy, D. B., "Experimental Modal Analysis Technique, System and Application for Miniature Structures," *CML* Report No. 96-011, Computer Mechanics Laboratory, Department of Mechanical Engineering, University of California at Berkeley, May, 1996.

[15] Radwan, H. R., and Whaley, R., "Servo Structural Interaction in Disk Drives Using Finite Element Analysis," ASME, Advances in Information Storage Systems, Vol. 5, 1993, pp. 101-118.

[16] Wilson, C. J., and Bogy, D. B., "Modal Analysis of a Miniaturize Structures with Application to Components in Magnetic Recording Disk Drives," *CML* Report No. 93-004, Computer Mechanics Laboratory, Department of Mechanical Engineering, University of California at Berkeley, May, 1993.

[17] Zeng, Q. H., and Bogy, D. B., "Modal Dynamics Experiment and Analysis of a Suspension Assembly Used in Hard Disk Drives," *CML* Report No. 96-013, Computer Mechanics Laboratory, Department of Mechanical Engineering, University of California at Berkeley, June, 1996.

[18] Zeng, Q. H., and Bogy, D. B., "An Investigation of the Dynamic Characteristics of a Hard Disk Drive by Experiment and Analysis," *CML* Report No. 96-017, Computer Mechanics Laboratory, Department of Mechanical Engineering, University of California at Berkeley, August, 1996.

[19] Williams, D., and Balasingam, S., "Why Rotary Actuators Behave the Way They Do," Data Storage, November/December 1995, pp. 43-48.

[20] Huang, F. Y., Imaino, W., Semba, T., Lee, F., "Rotary Actuator Dynamics With Active Damping," 11th Annual Symposium on Information Storage and Processing Systems, Session 8: HDD Actuator Design/Dynamics, June 1999.

[21] Huang, Y., Banther, M., Mathur, P. D., Messner, W. C., "Design And Analysis Of A High Bandwidth Disk Drive Servo System Using An Instrumented Suspension," IEEE/ASME Transactions on Mechatronics, Vol. 4, No. 2, June 1999.

[22] Krinke, T. A., "Second Generation Namakan Suspension," Technical Report, Hutchinson Technology, Inc., November 1998.

[23] Li, Y., and Horowitz, R., "Characterization And Compensation Of Air Turbulence Induced Vibration With Dual-Stage Actuators," 12th Annual Computer Mechanics Laboratory Sponsors Meeting, January 2000.

[24] Lim, K. B., "Method For Optimal Actuator And Sensor Placement For Large Flexible Structures," Journal of Guidance, Control and Dynamics, Vol. 15, No. 1, pp. 49-57, January-February, 1992.

[25] Hac, A., and Liu, L., "Sensor And Actuator Location In Motion Control Of Flexible Structures," Journal of Sound and Vibration, Vol. 167, No. 2, pp. 239-261, 1993.

[26] Ewins, D. J., "Modal Testing: Theory, Practice and Application," Hertfordshire, England: Research Studies Press Ltd., 2000.

[27] Yamaguchi, Y., Takahashi, K., Fujita, H. and Kuwahara, K., "Flow Induced Vibration of Magnetic Head Suspension in Hard Disk Drive", IEEE Transaction on Magnetics, Vol. 22, No. 5, September 1986, pp. 1022-1024.

[28] Yamaguchi, Y., Talukder, A.A., Shibuya, T. and Tokuyama, M., "Air Flow Around a Magnetic-Head-Slider Suspension and Its Effect on Slider Flying-Height Fluctuation", IEEE Transaction of Magnetics, Vol. 26, No. 5, September 1990, pp. 2430-2432.

[29] Tokuyama, M., Yamaguchi, Y., Miyata, S. and Kato, C., "Numerical Analysis of Flying-Height Fluctuation and Positioning Error of Magnetic Head due to Flow Induced by Disk Rotation", IEEE Transaction of Magnetics, Vol. 27, No. 6, November 1991, pp. 5139-5141.

[30] Lennemann, E., “Aerodynamic Aspects of Disk Drives”, IBM Journal of Research and Development, 1974, 18, pp. 480.

[31] Abrahamson, S. D., Eaton, J. K., and Koga, D. J., “The Flow Between Shrouded Corotating Disks,” Physics of Fluids A, 1989, Vol. 1, No. 2, pp. 241-251.

[32] Schuler, C. A., Usry, W., Webber, B., Humphrey, J. A. C., and Grief, R., “On the Flow in the Unobstructed Space Between Shrouded Corotating Disks,” Physics of Fluids A, 1990, Vol. 2, No. 10, pp. 1760-1770.

[33] Tzeng, H., and Humphrey, J. A. C., 1991, “Corotating Disk Flow in an Axisymmetric Enclosure With and Without a Bluff Body,” International Journal of Heat and Fluid Flow, Vol. 12, No. 3, pp. 194-201.

[34] Humphrey, J. A. C., Schuler, C. A., and Webster, D. R., 1995, “Unsteady Laminar Flow Between a Pair of Disks Corotating in a Fixed Cylindrical Enclosure,” Physics of Fluids, Vol. 7, pp. 1225-1240.

[35] Iglesias, I. and Humphrey, J., "Two- and Three-Dimensional Laminar Flows Between Disks Co-Rotating in a Fixed Cylindrical Enclosure", International Journal for Numerical Methods in Fluids, Vol. 26, 1998, pp. 581-603.

[36] Usry, W., Humphrey, J. A. C., and Grief, R., “Unsteady Flow in the Obstructed Space Between Disks Corotating in a Cylindrical Enclosure,” ASME Journal of Fluids Engineering, 1993, Vol. 115, pp. 620-626.

[37] Harrison, J.C., Lou, D.H. and Talke, F.E., "Air Flow at the Tip of an Obstruction Between Corotaing Disks", Advanced Information Storage Systems, Vol. 5, 1993, pp. 159-174.

[38] Gor, D, Humphrey, J. A. C., and Grief, R., “Ventilated Flow Between Corotating Disks with Large Obstructions in a Fixed Cylindrical Enclosure,” ASME Journal of Fluids Engineering, 1994, Vol. 116, pp. 828-834.

[39] Abrahamson, S. D., Chiang, C., and Eaton, J. K., “Flow Structure in Head-Disk Assemblies and Implications for Design,” Advances in Information Storage Systems, 1991, Vol. 1, pp. 111-132.

[40] Suzuki, H., and Humphrey, J. A. C., “Flow Past Large Obstructions Between Co-Rotating Disks in Fixed Cylindrical Enclosures,” Journal of Fluids Engineering, 1997, Vol. 119, pp. 499-505.

[41] Girard, J., Abrahamson, S., and Uznanski, K., “The Effect of Rotary Arms on Co-Rotating Disk Flow,” ASME Journal of Fluids Engineering, 1995, Vol. 117, pp. 259-262.

[42] Kim, B.-C. and Mote, C.D., “Suppressing Turbulence Induced Vibration of the Head Suspension Assembly in a Hard Disk Drive”, *CML* Technical Report, No. 99-015, August 1999.

[43] Schlichting, H., “Boundary-Layer Theory”, McGraw-Hill, Inc., 7th Edition, 1979.